Thèse

The Investigation on Mechanical Behaviours of Reinforcements and Machining Properties during Manufacturing Composites with Complex Shapes

L'étude des comportements mécaniques des renforts et des propriétés d'usinage lors de la fabrication de composites de formes complexes

Co-tutelle avec l'université "Dalian University of Technology" (CHINE)

Présentée par :

Shenglei XIAO

Discipline : Mécanique des solides, des matériaux, des structures et des surfaces

Soutenue le 30/10/2019 devant la commission d'examen

Jury members of the comitee:

Xiaohong Lu, Professeur	Dalian University of Technology	President/Examinatrice
Philippe Boisse, Professeur	INSA Lyon	Rapporteur
Wanyu Ding, Professeur	Dalian Jiaotong University	Rapporteur
Damien Soulat	ENSAIT	Co-directeur
Hang Gao, Professeur	Dalian University of Technology	Co-directeur
Huichen Zhang, Professeur	Dalian Maritime University	Examinateur
Peng Wang, Professeur	Université Haute Alsace	Examinateur
Chung Hae Park, Professeur	IMT-Lille Douai	Examinateur

ACKNOWLEDGEMENTS

Firstly, I would like to sincerely appreciate the endless support from my supervisors: Prof. Damien SOULAT, Prof. Hang GAO and Prof. Peng WANG. Their consistent concern and valuable guidance always help me in all time of research and writing of this thesis. All my Ph.D supervisors have remained kind throughout and encouraged me to do what I want in project.

Back to beginning of this thesis, I am very grateful for the special thanks to Prof. Peng WANG and Prof. Hang GAO, the former gave me this co-joint program that not every Ph.D. student in CHINA could get. The latter allows me to take this opportunity to broaden horizons not only in my growing professional knowledge but also in the aspect of life experience.

I also want to express my gratitude to my contemporary friends or colleagues in GEMTEX: Chan HUI, Hao SHEN, Chen CHEN, Mengru LI, Imen GNABA, Vivien BAEEAL, Henri LANSIAUX for technical discussions and knowledge-sharing during my time in research.

I am also indebted to my family members: my parents, Peiyi XIAO, Cuiping WANG; my wife, Yixuan FU; my elder brother and his wife, Shengbing XIAO, Huiying LIU, for their enduring love and support even I had been depressed and self-abandonment before I became a Ph.D. Especially for my wife, who made a huge sacrifice to support what I want to do, and endures I used to concentrate on my research neglecting the ordinary and peaceful life, which is indeed a driving force for my work and the source of true happiness.

Lastly, I would like to thanks my Ph.D. friends and colleagues who are working or studying in CHINA for helping me to do a lot of things including experimental tests or trivia in life when I was studying abroad.

ABSTRACT

Title:

The Investigation on Mechanical Behaviours of Reinforcements and Machining Properties during Manufacturing Composites with Complex Shapes

The mechanical characteristics and deformability behaviours of reinforcements are essential knowledge to acquire desired quality during manufacturing composites with complex shapes. Meanwhile, the machining properties of composites also greatly determine the corresponding service performance of composites parts. Hence, this thesis is concentrating on the two aspects in manufacturing and machining processes to explore what characters the special features in the mechanical properties and deformability behaviours of braided fabrics, which are promising and excellent textile reinforcements for composites with complex shapes, and investigate the machining composites using abrasive waterjet technique through improvement in process to further enhance the machining efficiency without sacrifice of quality. The mechanical characteristics of braided fabrics, especially for in-plane shearing phenomenon, were originally investigated and modelled based on bias-extension test. Besides, the triaxial braided fabrics were also experimentally investigated in mechanical characteristics with respect to braiding parameters including braiding angle and number of yarns. The deformability behaviours of triaxial fabrics during preforming process were integrally discussed and correlated with the corresponding defects based on the different preforming pressures. Meanwhile, the mechanical models were proposed to further realize the law behind the deformability behaviours. The variation of deformability behaviours according to braiding angle was predicted through an approach of geometrical model and verified by experimental results. It is inferred that the geometrical analysis could show a well correlation with results to a certain degree. The upgraded multi-pass cutting of abrasive waterjet was firstly introduced into composites machining process based on the exploration of the corresponding material removal mechanism. It was experimentally concluded that such technique could effectively enhance the machining quality and efficiency.

CONTENTS

LIST OF FIGURES

Chapter I

Chapter II

Chapter III

Chapter IV

LIST OF TABLES

GENERAL INTRODUCTION

Problems statement

The composites with complex shapes have been gained more and more attention in aerospace or automobile industry due to their outstanding advantages such as high fibre volume, impact resistance and interlaminar shear properties. Braided textiles are regarded as the promising reinforcements or preforms to manufacture the composites with complex shapes, which are produced by braiding textile technique that offers the special virtues including control over yarns angle and fast fibre deposition rate compared to weaving. The braided reinforcements exhibit the satisfied adaptability, a high ability to prevent cracks and abrasion, further broadening their range of applications. In the manufacturing composites with complex shapes, the first step is the preforming process that the reinforcements are deformed into desired shapes. In this process, the mechanical properties and their corresponding deformability behaviours of reinforcements play an important role in the final service performance of composites. Therefore, it is demanded and essential to master the mechanical properties and their corresponding deformability behaviours during the preforming process in order to ensure the quality of the composites. Especially regarding braided reinforcements, however, there are still problems that need to be analysed and solved. Furthermore, before the assembly process but after composites manufacturing, the machining process is unavoidable in most cases. Yet traditional machining techniques are unable to well balance the relation between machining quality and efficiency due to heat-affect zone or high cost. Abrasive waterjet (AWJ), a non-traditional and cool machining technique, promisingly has an ability to improve efficiency while ensuring the desired quality. However, fully presenting advantages of AWJ into composites machining process should be under the condition that the material removal mechanism is integrally acquired. Besides, in order to further improve the efficiency, the process innovations are also needed to be explored or modified based on the special material removal mechanism of composites by AWJ.

At first, the mechanical properties of braided reinforcements as the fundamental knowledge to realize the corresponding deformability behaviours during preforming process still need to be further explored in the aspect of quantitative analysis rather than qualitative analysis as previously studied, especially for in-plane shearing property that is dominated mechanism for defects such as wrinkles that are usually detected during preforming process. Compared to woven reinforcements, a kinematical analysis to acquire in-plane shearing property is still absent due to the lack of an appropriate model based on varied braiding angle to describe and predict such property. Furthermore, the mechanical properties are also characterized with

essential fabric features on account of braiding angle and fibre number, especially for triaxial braided reinforcements that contain the axial yarns added along the longitudinal axis as third orientation in order to enhance the fibre fraction. These features are heavily related to mechanical properties, as well as thermodynamic characters during the reinforcements deformation. Unfortunately, such relation has not been totally explored even if in a qualitative method by now.

Secondly, the deformability behaviours of braided reinforcements during preforming process based on the mechanical properties are still unknown to a certain degree. The braiding angle, which can be designed for required circumstance rather than constant 90° in woven reinforcements, is much related to the appearance in mechanical properties, resulting in variation of deformability behaviours during preforming process. However, by now, the analysis of deformability behaviours is focusing on the different punch tools, the relation between punch force and deformability behaviours. The driving mechanical characters, especially for braided reinforcements, are not clearly understood. Besides, the variation of deformability behaviours based on reinforcements parameters such as dimension and braiding angle is still uncertain and should be quantitatively analysed.

At last, the material removal mechanism (MRM) is essential for the machining process no matter what kind of processing technique is used. Especially for fibre reinforced composites including two phases of fibre and matrix, The MRM is different from each other and need to be ascertained for each processing technique in order to figure out the special defects during machining which are related to MRM. Abrasive waterjet (AWJ), as a novel processing technique, possesses an advantage of cool machining over contacted processing techniques because of no heat-affect zone. However, the composites MRMs by AWJ and the corresponding defects are still unknown. Furthermore, the processing innovations introduced from other materials such as metal or ceramics need to be modified and improved, in order to fit the composites machining characteristics and raise efficiency.

Thesis overview

This thesis is mainly focusing on exploring the mechanical properties and deformability behaviours during the manufacturing process of composites with complex shapes, and the machining properties of composites including materials removal mechanism and process innovation that could improve the machining quality and efficiency. Chapter I will detail the overall background of composites including the conceptions, manufacturing and machining

processes. Besides, the research status on the aims of this thesis will be discussed. Chapter II will discuss the mechanical properties of braided reinforcements especially for in-plane shearing property, and investigate the influence of parameters of reinforcements such as braiding angle and fibre number on mechanical properties. Moreover, the kinematical model of in-plane shearing for braided reinforcements will be proposed and verified with experimental results. Besides, thermo-mechanical properties influenced by friction will be also analysed. Chapter III will explore the deformability behaviours of reinforcements during preforming process based on Chapter II. The deformability behaviours will be defined and classified; their corresponding defects during preforming process will be also discussed. The mechanical models will be proposed to grasp the significance of law behind different deformability behaviours. Furthermore, the variation of deformability behaviours impacted by different braiding angles will be studied based on the experimental analysis and theoretical model, trying to figure out the relation between basic parameters of reinforcements with deformability behaviours. Chapter IV will study the MRMs of composites by AWJ and investigate the correlation between material removal mechanism and corresponding defects. Besides, multi-pass AWJ machining, which is a processing innovation in AWJ that has been proved as an improvement in machining quality and efficiency, will be originally introduced and modified into composites machining for the purpose of insurance of machining quality while enhancing efficiency. Chapter V will draw a general conclusion of this thesis and put forward the perspectives.

I. STATE OF THE ART

1.1 Introduction

The Fibre Reinforced Plastics (FRPs) have been widely applied in various manufacturing fields such as aeronautics, space, sporting goods, marine and automotive due to their light-weight, high specific strength and stiffness, excellent fatigue resistance and impact resistance compared to common metallic alloys. More recently, the fibre reinforced composites are being changed from the laminated structure, which is an outstanding alternative to replace the alloy as the load-carrying parts in aerospace and automotive, to advanced complex shapes which can further broaden their application areas in order to reduce the total weight, save costs and energy. Besides, based on the unique advantages compared to synthetic fibres, replacing the conventional fibres such as synthetic carbon and glass with natural fibres, for instance, flex and cotton, is the alternative way to reduce the impact on environmental pollution and further cut costs. Therefore, in this chapter, the extensive literature on the background of FRPs including the conceptions, current research trends, progress and problems, is reviewed in detail, aiming to perceive the scientific issues addressed in this thesis under a full background description.

Firstly, the literature on general composites reinforced by synthetic and natural fibres including their conceptions, process techniques, applications and tendencies, especially for composites with complex shapes, are briefly presented. Secondly, the mechanical behaviours and deformability behaviours of reinforcements fabricated by braiding and weaving techniques during manufacturing, are discussed. Lastly, abrasive waterjet (AWJ) as a promisingly machining technique is reviewed in regard to characteristics, applications and innovations, as well as the limit in composites machining.

The scientific issues that thesis is going to address are proposed at the end of this chapter based on the following review.

1.1.1 The Composites

The composites are the materials made by two or more constituent materials with significantly different physical or chemical properties that, when combined, produce a material with characteristics different from the individual components. The individual components remain separate and distinct within the finished structure, differentiating composites from mixture and social solutions as shown in Fig. 1.1 [1–4]. The composites could offer competitive properties including high ability to shape and process, excellent mechanical properties offered by relatively low weight compared to monolithic materials such as metal and plastic [5–8].

Thus, the growing use has risen widely from various fields, especially for aircraft and automotive, the demanding environments that the most advanced composites perform routinely on [9–12] referred to Fig. 1.2. Generally, the typically engineering composites include many types, such as metal matrix composites, ceramic matrix composites and reinforced plastic [13–16]. In this thesis, the long fibre-reinforced plastics (FRPs) are mainly detailed.

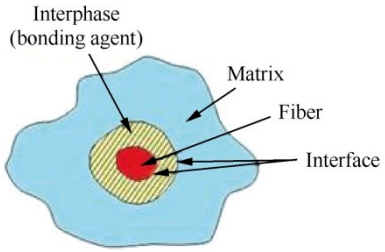

Fig. 1.1. The example of a schematic illustration of composite material structure [17].

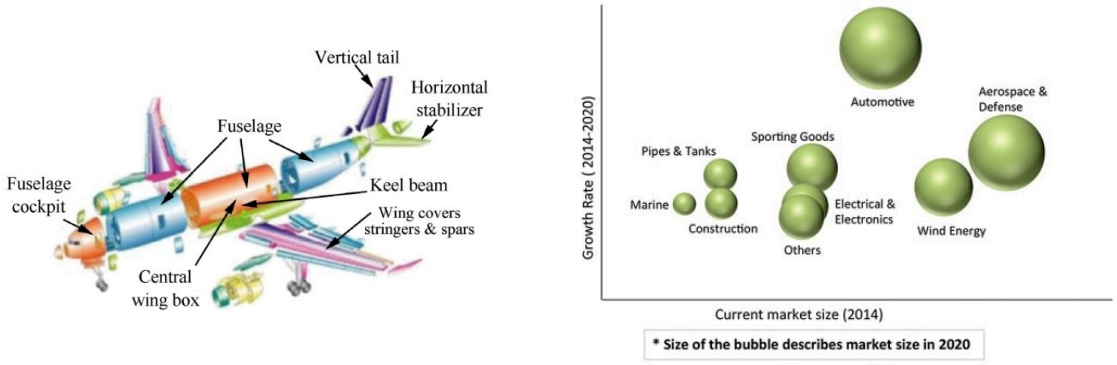

(a) (b)

Fig. 1.2. The application of FRP; (a) Large-size carbon fibre reinforced plastic (CFRP) composites component used in airbus 350; (b) Main applications distribution for FRP [18,19].

The Fibre-Reinforced Plastics (FRPs), also named as fibre-reinforced polymers, are a category of composite plastics that specifically use fibre materials to mechanically enhance the strength and elasticity of plastics. The original plastic material without fibre reinforcement is known as the matrix or bending agent that characterises tough but relatively weak. Hence, the stiffer fibre can be used as a reinforcing phase that can totally increase the strength or elasticity in FRPs compared to matrix alone. The extent that strength and elasticity are enhanced in FRPs depends on the mechanical properties of the fibre and matrix, their volume relative to one another, and the fibre length and orientation within the matrix [20–22]. The excellent properties of FRPs compared to metals such as high specific strength and stiffness are shown in Table 1.1, revealing the most promising advantage of weight saving that leads to

the application of FRPs in aerospace since the early 1930s [23]. By now, the commonly reinforcing fibres are synthetically manufactured such as carbon, glass and aramid due to the high stiffness, strength and corrosion resistance [24–27]. Before being boned to the matrix that is often thermosetting or thermoplastic resin polymer, fibre reinforcements are needed to be fabricated through textile processing techniques of weaving, knitting, braiding and stitching to process in sheet, continuous mats, or as continuous filaments for spray applications [28]. After fabricating the fibre reinforcements, the moulding processes of FRPs begin through placing the fibre reinforcements on or in the mould. The fibre reinforcements can be made by dry fibre, or fibre that already contains a measured amount of resin called "prepreg". The dry fibre reinforcements are "wetted" with resin either by hand or the resin injected into a closed mould [29]. The part is then cured, leaving the matrix and fibres in the shape created by the mould. Heat and/or pressure are sometimes used to cure the resin and improve the quality of the final part. The forming processes, by far, generally includes many types such as wet layup, filament winding, resin transfer moulding and liquid composite moulding. Applying the different forming processes is depended on the properties of matrix and fibres and the purposes [30,31].

Table 1.1. Comparison of characteristics between composite materials and metals

	Steel	Aluminium alloy	High-resistance carbon epoxy resin	High-modulus carbon epoxy resin	R-glass epoxy resin
Tensile strength (MPa)	1850	500	1000-1300	1000	1800-2000
Young's modulus (GPa)	200	72	130	200	53
Density (g/cm^3)	7.9	2.8	1.5	1.7	2
Coefficient of linear expansion-longitudinal ($10^{-6}K^{-1}$)	12	23	-0.2	-0.8	6
Coefficient of linear expansion-transversal ($10^{-6}K^{-1}$)	12	23	35	35	31

* Unidirectional composites with a fibre content ratio of 60%

As the concerns for sustainable development for global environmental issues, and an increased awareness of renewable "green" materials that have initiated efforts in many industries, the conventional synthetically fibre composites are being discouraged in spite of

having the distinguish mechanical properties, mainly due to non-degradable property that is heavily harmful to society and environment where human being live [7,10,25,32]. Thus, the need for replacing the conventional composites with almost equal mechanical properties is urgently acquired by human to build the eco-friendly society. In recent years, the reinforcements made by natural fibres such as flax, have attracted much attention for researchers due to comparable specific mechanical properties to synthetic fibres as shown in Table 1.2. Besides, the various advantages such as low cost, renewability, recyclability and bio-degradability are also gradually appealing to aeronautic and automotive industries, where continuously require reducing the weigh and obtaining recyclable composites in order to cut cost and save energy [11,22,33–36]. Furthermore, these industries require not only the advanced materials but also the complex shapes in order to further replace the metal parts that are not the mainly carry component, as shown in Fig. 1.3. For manufacturing the composites with complex shape, the fabrics (reinforcements) fabricated by braiding or weaving textile techniques are generally used. The following sections focus on the braided and woven reinforcements with respect to their definition, characteristics and comparison.

Table 1.2. Mechanical properties of natural fibres as compared to conventional reinforcing fibres [37].

Fibre	**Density (g/cm^3)**	**Elongation (%)**	**Tensile Strength (MPa)**	**Young's Modulus (Gpa)**
Cotton	1.5-1.6	7.0-8.0	287-597	5.5-12.6
Jute	1.3	1.5-1.8	393-773	26.5
Flax	1.5	2.7-3.2	345-1035	27.6
Hemp	---	1.6	692	---
Ramie	---	3.6-3.8	400-938	61.4-128
Sisal	1.5	2.0-2.5	511-635	9.4-22.0
Coir	1.2	30.0	175	4.0-6.0
Viscose	---	11.4	593	11.0
Soft Wood Kraft	1.5	---	1000	40.0
E-glass	2.5	2.5	2000-3500	70.0
S-glass	2.5	2.8	4570	86.0
Aramid	1.4	3.3-3.7	3000-3150	63.0-67.0
Carbon	1.4	1.4-1.8	4000	230-240

Fig. 1.3. The examples of FRPs with complex shapes

1.1.2 The woven and braided reinforcements

As discussed previously, the reinforcements fabricated by braiding and weaving techniques are generally applied in manufacturing composite parts with complex shapes. Weaving is a method of textile production that two distinct sets of yarns are interlaced at right angles to form a two-dimensional woven fabric as shown Fig. 1.4(a). The longitudinal yarns are called the warp and the lateral yarns are weft, and the warp and weft are regularly oriented with angle 90°. The two-dimensional reinforcement can be layered by woven fabrics as a laminated structure as shown in laminate made by stacking laminas in different orientations (Fig. 1.4b). The yarns are only aligned along the plane in weft X and warp Y direction and no yarns are aligned in the through-thickness or Z-direction, possibly bringing about the occurrence of delamination [38].

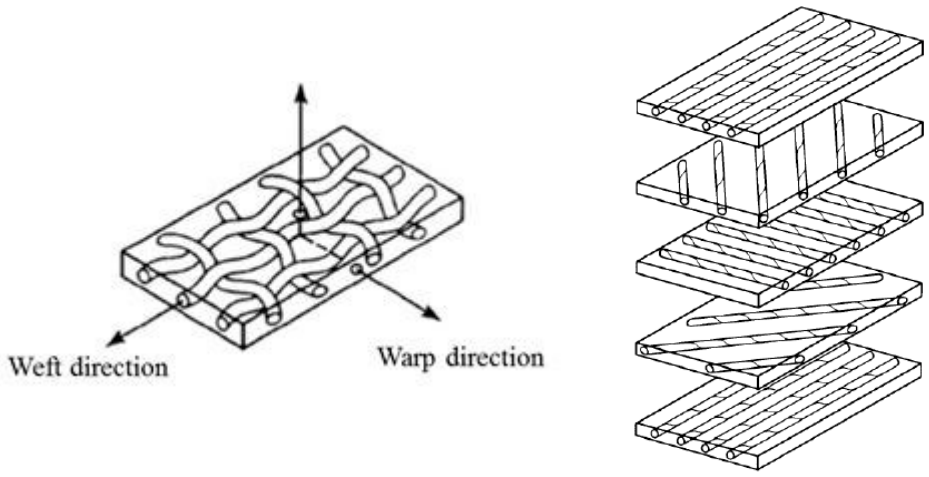

(a) (b)

Fig. 1.4. Lamina fibre reinforced composite: (a) Lamina with 2D woven fabric; (b) Laminate made by stacking laminas in different orientations [39].

Three dimensions (3D) woven reinforcements or multilayered fabrics composed of several in-plane woven layers, which are linked together by yarns passing in the Z direction by several methods such as layer-to-layer angle interlock, through-the-thickness angle interlock and orthogonal as shown in Fig. 1.5 [40], are proposed in order to improve impact damage

tolerance, through-thickness mechanical properties while reducing the fabrication costs. Guénon et al. showed that even for low binder yarns content about 1% in 3D carbon/epoxy composite the delamination toughness for mode I is about 14% higher than for 2D carbon/epoxy prepreg laminates [41]. Cox et al. studied the failure mechanisms of 3D woven carbon reinforced polymer composites on tension, compression and bending. They observed that the 3D woven composites exhibit high strain to failure in tension as well in compression [42]. However, the main problem facing the use of multilayer woven fabrics is the difficulty in producing a fabric that contains yarns oriented with angles between 10° to 170°, which is the limit of their further application. Thus, the braided reinforcements produced by braiding technique present the excellent adaptability due to varying braiding angle, being considered as the promising reinforcements in manufacturing composites with complex shapes [43,44].

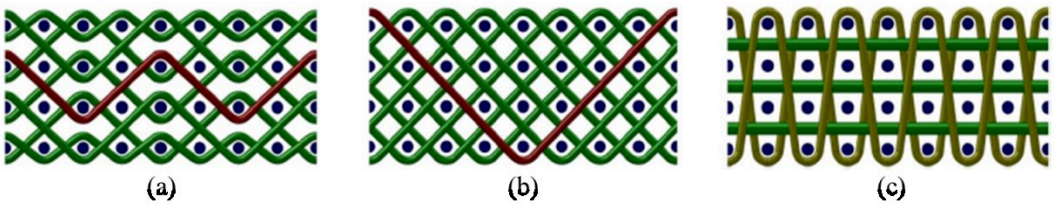

Fig. 1.5. Typical 3D woven architectures: (a) Layer-to-layer angle interlock; (b) Through-thickness angle interlock; (c) Orthogonal [45].

Braiding, as the second major textile way of manufacturing reinforcements, has been suited to manufacture of narrow width flat or tubular fabric. Braiding is done over top of mandrels that vary in cross-sectional shape or dimension along their length, likely originated from the maypole dance, a well-known practice in several European countries [46,47]. The braiding machine has been developed to accelerate the braiding process in order to satisfy the industries requirement. A typical braiding machine consists of a track plate with a cam path that is followed by the bobbins moved by the rotation of horn gears. Unlike the weaving, the braiding technique can offer the different braid patterns and types such as diamond braid, regular braid and flat, circular braid shown in Fig. 1.6 [48]. Furthermore, the biaxial, produced by half the carriers moving in clockwise and the other half in the counter clockwise, can be considered as a typical structure that the angle between two adjacent bias yarns is not limited to 90°, but can be changed between 10° to 170°, as shown in Fig. 1.7. The half of this angle is regarded as one of easy-controlled parameters during the reinforcements preparing and can be defined as braiding angle [49]. In particular, the triaxial braids, which contain the axial yarns added along the longitudinal axis as third yarn direction, could effectively enhance the high fibre volume fraction. The other advantages performed by braiding rather than

weaving include increased toughness, control over yarns deposition and fast fibre deposition rate [38,50–56]. However, the braiding is also limited to objects with large size; it means that the braiding could only produce the fabrics with a narrow width, which is restrained by the current braiding machine. Furthermore, the long-setup time to recharge the huge number of carriers is also the limitation to braiding efficiency. Concerning the kinetics of braiding process, in addition, a great deal of friction in the system subjected by yarns is needed to considered carefully, especially for the friction-sensitive yarns that are not recommended for braiding.

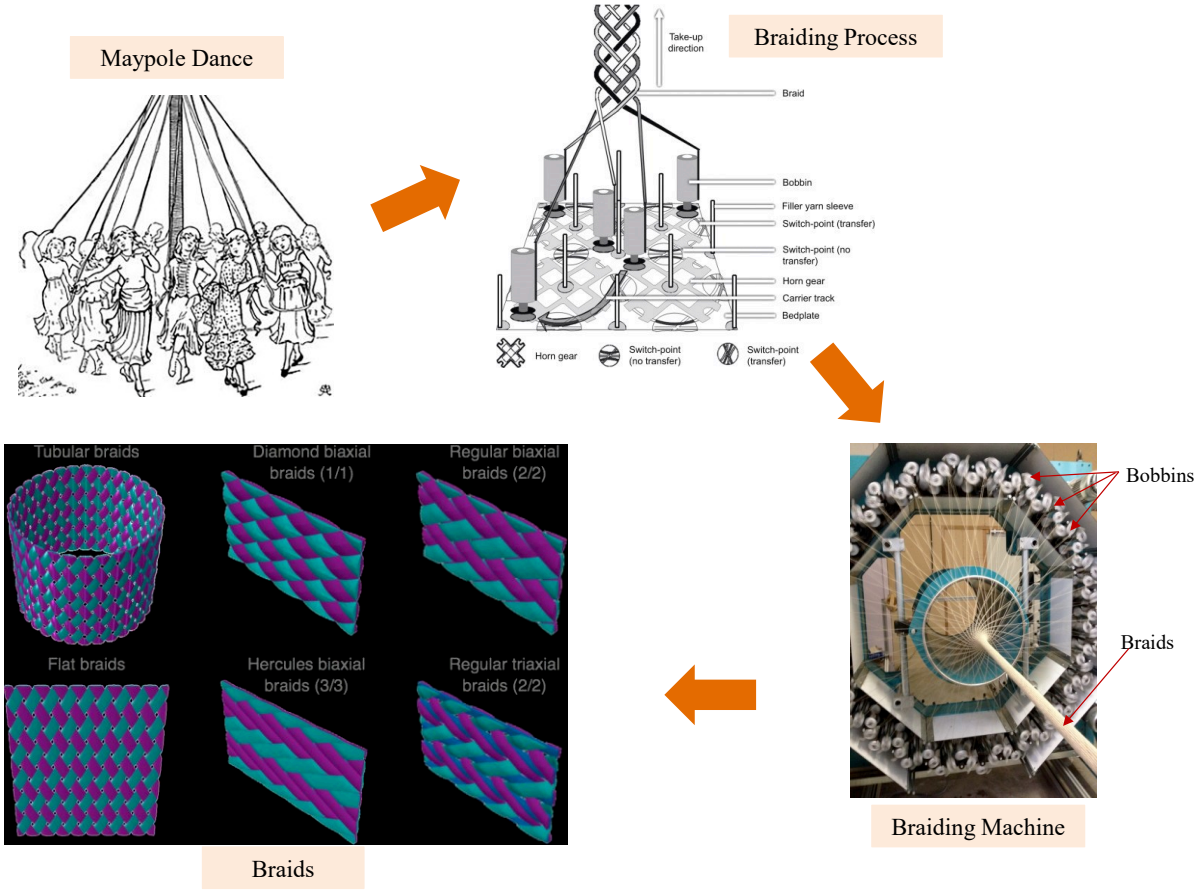

Fig. 1.6. Braiding process and braiding fabrics.

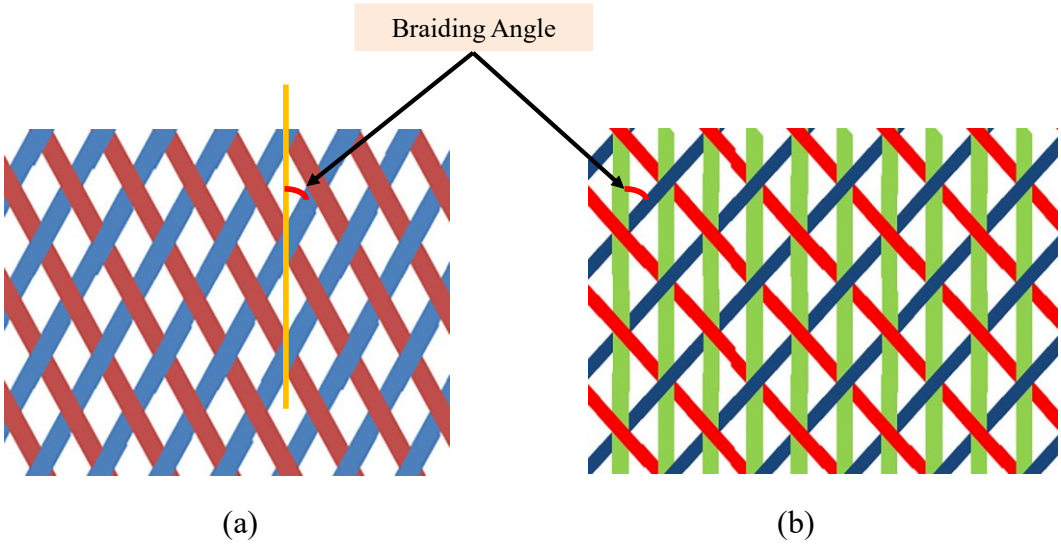

Fig. 1.7. The biaxial and triaxial braids structure: (a) Biaxial; (b) Triaxial.

The 3D braided reinforcements can be also generated by the interlock process as same as weaving. Besides, the two braiding processes, four-step and two-step, are also able to produce reliable 3D reinforcements. However, compared with these processes, the in-plane property could be maintained more firmly by multilayer interlock rather than the other processes [57]. 3D braided reinforcements have good conformability, drapability, torsional stability and structural integrity, which are strongly depended on the number of axial yarns, the angle of braided yarns and their braiding pattern. Associated to braiding technique, a great of deal of kinematic analysis has been published [58–60] with respects to models [51,58–63] in function of braiding parameters and characteristics of braids (braiding angle, cover factor, volume fraction, but also yarn's crimp). The analytics models were completed by numerical software, as described in the numerous works of Y. Kyosev [64–66]. The 3D braided reinforcements show a less tensile strength in both directions and less transverse tensile modules, whereas the longitudinal compressive properties and tensile modulus are better than laminate [50,67]. Braided composites also have the interesting mechanical properties in terms of high shear, torsion resistance and tolerance to damage at low or high speeds. Another advantage is related to their dimensional stability involving near net shape manufacturing capabilities [53,68–73]. The development of mechanical models able to predict the mechanical behaviours of braided composites [49,52,74–77], and braiding angle is the subject of numerous works published [53,54,56,78–95]. Recently Catera & al. [96] proposed an approach based on a multi-scale composite modelling starting from the evaluation of homogenized material properties of triaxial carbon braided at the mesoscale for a subsequent FE-based modal analysis. By the same approach, Werkamp-Richter et al. [97] investigated numerically the non-linear

mechanical response of triaxial braided composites under multiple loading. Consequently, braided fibre reinforced composites have a broad range of industrial applications in a large variety of markets as aerospace, defense, sport, medical, automotive [49,50,58,78,96,98–100], and also in a specific market. For example, braided fibre reinforced ropes are used for deep-sea handling applications, where their low weight results in more efficient lifting compared to steel wires [101,102].

1.1.3 Liquid composite moulding (LCM) process for manufacturing composites

Since composites are used in many industries, the manufacturing processes of composites become also important. The matrix material can be introduced to the reinforcement before or after the reinforcement material is placed into the mould cavity or onto the mould surface [103]. The matrix material experiences a melding event, after which the part shape is essentially set. Depending upon the nature of the matrix material, this melding event can occur in various ways, such as chemical polymerization or solidification from the melted state. In general, the reinforcing and matrix materials are combined, compacted and processed to undergo a melding event. After the melding event, the part shape is essentially set. There are different types of moulding processes which can be utilized to form a composite material. In this part, the Liquid Composite Moulding (LCM) process for manufacturing composites with complex shapes is discussed.

The Liquid Composite Moulding (LCM) processes which include more than a dozen different types of manufacturing processes [104] are increasingly used in the manufacture of advanced composites. In LCM processes, the resin is injected into the reinforcement and fills the stack of the preform, and then converted from liquid to solid state by the thermally activated crosslinking reaction. Resin Transfer Moulding (RTM), one type of LCM as shown in Fig. 1.8(a), is a process that resin is injected under pressure into fibrous preforms that are held between two solid and closed moulds. The stack of the reinforcement is placed in the mould before its closing and clamping. Low viscosity resin is then pumped into the mould until it is filled. Since this is a matched-die process, it is capable of holding very tight dimensional tolerances [105]. The mould can contain internal heaters or can be placed in a heated platen press for a cure. Other variations of this process include vacuum-assisted RTM (VARTM) seen in Fig. 1.8(b), which a single-sided tool is used along with vacuum bag. Instead of injecting the resin under pressure, a vacuum pulls the resin through a flow medium that helps impregnate the preform [106]. VARTM is a cost-effective process which can be used under

flexible conditions because it only utilizes atmospheric pressure to push the resin into the mould cavity. It provides a possibility to manufacture complex and thick parts with high mechanical properties. The standard fibre volume fraction of the composites produced by infusion process is 55%, sometimes can rise up to 60% under certain conditions. Moreover, due to the needless of mould on the upper part and the reuse of the mould at the bottom part, composites can be produced at a lower cost. However, during the infusion process, a vacuum bag is used to replace the rigid mould, which will lead to an uncontrolled fibre volume fraction. Moreover, it is difficult to measure the transverse permeability of the preform which plays an important role in the infusion process. The advantages of RTM include increased laminate compression, a high glass-to-resin ratio, and outstanding strength-to-weight characteristics [107].

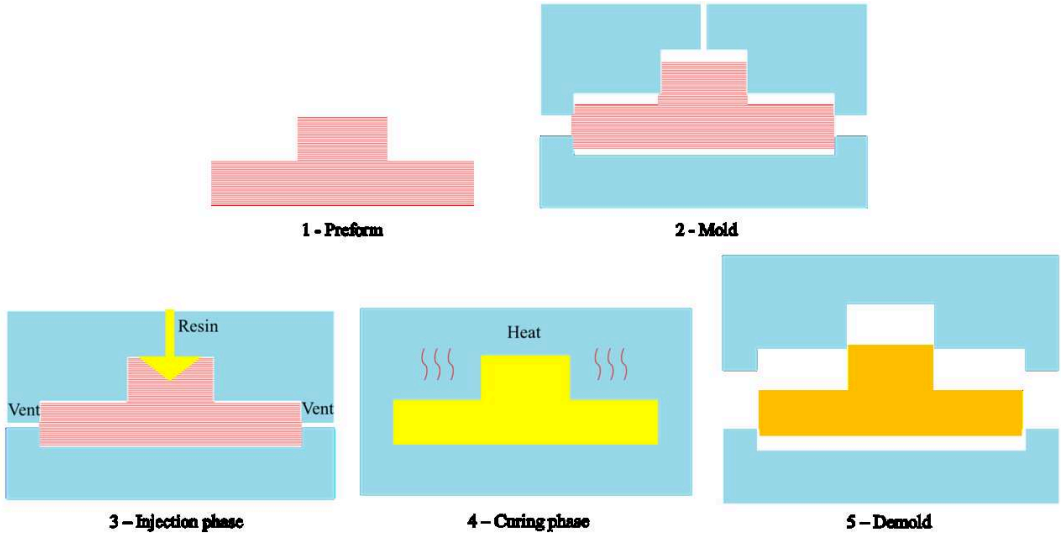

(a) RTM

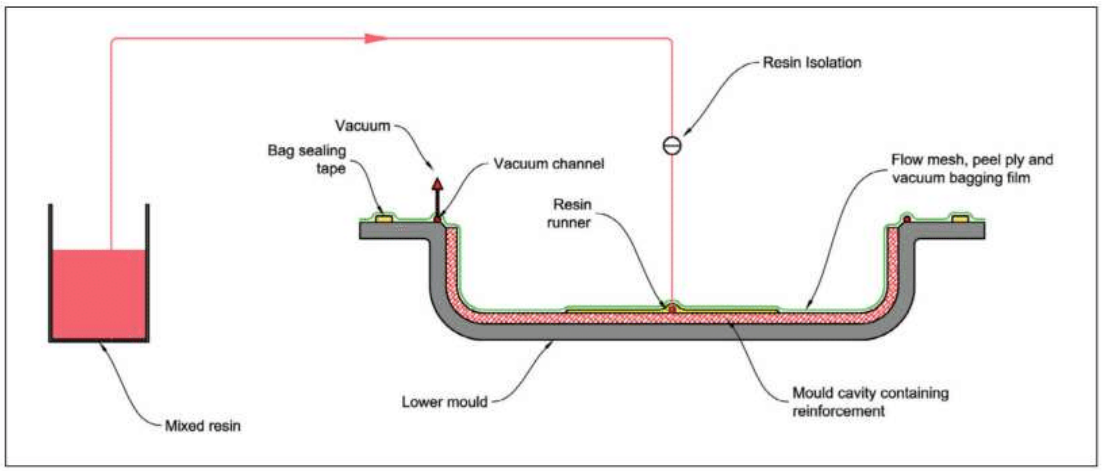

(b) VARTM

Fig. 1.8. Resin Transfer Moulding injection process [108].

Before the resin injection process, the reinforcements are preformed to be the desired shape. This process is called preforming, draping or stamping as shown in Fig. 1.9, which are similar with pressing of flat sheet metal in either blank or coil form into a stamping press that a tool and die surface forms the metal into a net shape. However, the reinforcements are nonhomogeneous so that the deformability behaviours are totally different from mental. The specific deformability behaviours, especially for textile reinforcements, are reviewed in Section 1.3.

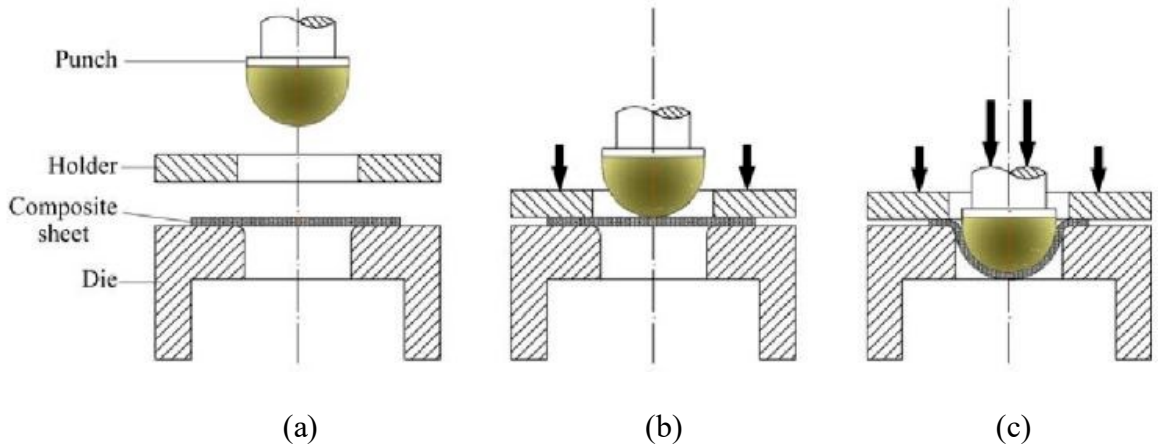

Fig. 1.9. Illustration of thermal stamping process: (a) Heating die set and punch; (b) Heating specimen through heat transfer; (c) Thermal stamping [109].

1.2 The mechanical behaviours of reinforcements

As reviewed previously, the current studies principally focus on the mechanical behaviours of composites reinforced by braided and woven fabrics, which are contributed by many factors such as characteristics of reinforcements and matrix, the property of interface between fibre and matrix, and the resin injection process. The mechanical behaviours of reinforcements before resin impregnation, however, do not acquire enough attention. Fundamentally, the mechanical behaviours of reinforcements composed by textile fabrics definitely determine the properties of the composites, especially for composites with complex shapes, because the mechanical behaviours of a fabric heavily influence the preforming quality. The basic mechanical behaviours of reinforcements mainly include the in-plane shearing and tensile properties, the compression and bending properties [53,68,110]. Among them, the in-plane shearing and tensile properties of the fabric are primarily considered as the most dominant mechanism as reinforcements are under preforming process.

The in-plane shearing is defined as the rigid yarn rotation rather than a shearing of yarn itself under the condition that the ends of fabric sustain the tension. The shearing force is due to

friction between crossing yarns, so that the in-plane force initially is very small compared to the known in-plane tension values. And then, the in-plane shearing force gradually increases due to contact and laterally compression of intersection yarns. When all the yarns are in contact and compressed, the force increases rapidly, and a critical locking angle is reached [111–113]. There are two principle methods to determine the shear properties of textile reinforcements, bias-extension test and picture frame test, as shown in Fig. 1.10. Such two methods are initially designed since the 1960s and then developed for investigating the in-plane shearing properties of woven fabrics [114–117]. The bias-extension test consists of a tensile test on the woven fabric that the warp and weft yarns directions are orientated initially at 45° to the direction of applied tension. The description of bias-extension with respect to its specifications, the geometry of rectangular specimen and different shearing zones, are made by Wang et al. in 1998 [118]. If the shearing zones in the fabric can be seen during the test, the size of the fabrics (reinforcements) must satisfy the certain geometrical conditions, as shown in Fig. 1.10(a). In general, when the length of specimen, L, is more than twice its width, W, and assuming no inextensibility and slippage of yarns, there are three zones distinguished theoretically during the test that the zone A remains undeformed, a pure shearing zone in the centre of fabric (zone C), and a half of shearing zone B near zone A [56,119–122]. It is assumed that the in-plane shearing is constant in each zone. A picture frame test is a hinged frame with four rigid bars with equal length as shown in Fig. 1.10(b). The tension is applied across diagonally opposite corners of the picture frame rig, causing the picture frame to move from an initially square geometry into a lozenge. The specimen within the picture frame is theoretically subjected to a pure and constant in-plane shearing [114,123,124]. Contrasted with such two tests, it is suggested that the bias-extension test lies the advantage in terms of accuracy and convenient, especially for exploring the thermo-characteristics. Consequently, the research on exploring the in-plane shearing based on bias-extension is relatively extensive. Although the other experimental tests have been proposed that a rectangular fabric specimen is clamped on two opposite edges, prescribe an in-plane shear deformation to the woven fabric [112,115], the tests are close to picture frame [125].

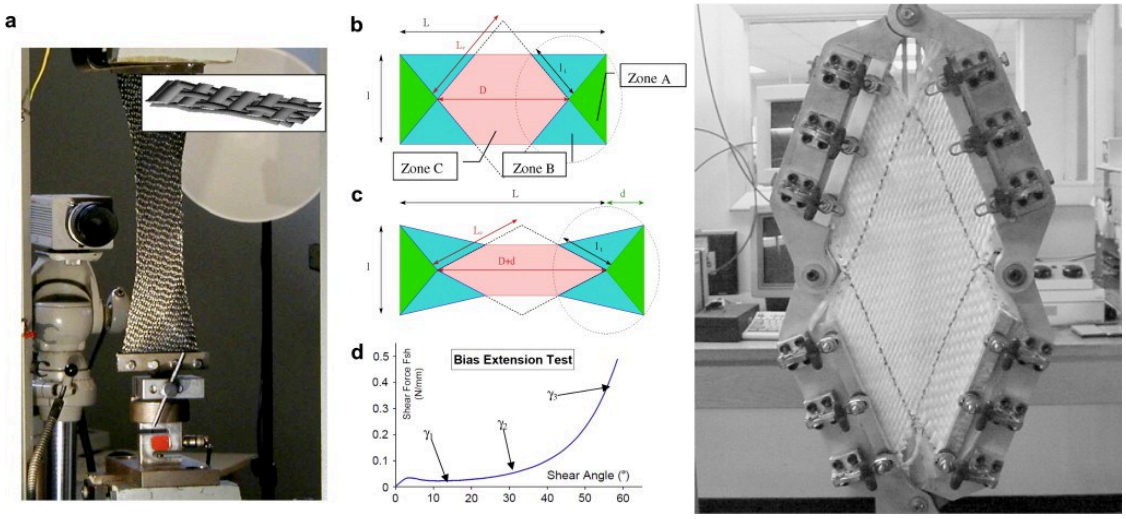

(a) (b)

Fig. 1.10. Two principle methods to determine in-plane shearing behaviours of woven fabric: (a) Bias-extension test; (b) Picture frame test [119,126].

Based on the assumptions including no slippage, neglected bending stiffness and inextensibility of yarns, the characteristics in in-plane shearing need to be specified on the kinematic correlation among the in-plane shear angle, shear stress, force and extension of fabric. Thus, the variation of in-plane shearing angle based on the shear load and force has been explored gradually [119,127] and can be directly obtained by optical analysis [128]. However, only explaining the variation of in-plane shearing angle is not enough to characterize the property of in-plane shearing. The shearing force to determine the in-plane shearing angle also needs to be confirmed at least concerning the geometry of specimen [126,129–131]. The shear load to the overall load of test machine were introduced in [114,126]. In addition, the shear moment was studied through the formulation of finite elements [128,132,133], completing the property of in-plane shearing. Other models based on the energetic approach were proposed to clearly specify the characteristics of shearing zones [134].

As the discussion above, the in-plane sharing behaviours are normally determined by dry composite reinforcements. However, for thermoset or thermoplastic prepregs, the mechanical behaviours are significantly different from that of dry textile reinforcements under the temperature variation, which is specially called as thermo-mechanical characterisations, depending on the state of the resin that could substantially modify the properties. In the case of thermoset prepregs, the performing temperature in the test is lower than curing temperature, but the in-plane shearing tests are performed at the temperature slightly over melting point of resin. According to properties of bias-extension and picture frame tests, the bias-extension is

relatively more adaptable for investigating the in-plane shearing at high temperature [129,135]. The loads on the specimen measured for bias-extension tests at a temperature around the melting point (343°C) for a carbon satin/PEEK matrix prepreg suggests that the influence of temperature is strong. The in-plane shear stiffness is much larger at 320°C than at 360°C. Nevertheless, over 360°C, the shear stiffness does not decrease anymore [136]. Besides, the different speeds at various temperatures in the tests also have an impact on the strain rate [136,137], but they are less important than the influence of temperature, possibly due to in the constitutive model [134,138].

According to the researches review above, it can be induced that the exploring of mechanical behaviours recently is primarily focusing on the woven reinforcements, which has been saturated indeed. The braided reinforcements have not been gained enough attraction on mechanical behaviours. The variation of braiding angles, which is considered as one of special parameters distinguished from woven ones, increases the difficulty of mechanical analysis. Thus, the geometrical and mechanical models concerning the braiding angles compared to woven ones are proposed. For examples, a geometrical and micromechanical model was developed by Potluri and Manan [52] for non-orthogonal reinforcements. In this study, the parallel between braided and sheared woven fabrics is established. The increasing of nominal axial strain in function of the braiding angle during tensile tests was experimentally shown on biaxial braids by Harte and Fleck [139]. A predictive model on the mechanical behaviour of biaxial braided fabrics was compared to experimental results in Hristov et al. [140], but in this study, the initial braiding angle of samples is considered as constant. Significant differences (around 20%) between numerical results computed with mechanical model and those obtained experimentally were demonstrated by Dabiryan and Johari[141] on biaxial braids with high braiding angles. Specific materials, as auxetic, were also used in biaxial braided structures and mechanically characterized by Subramani et al.[142]. Rebelo et al. [143] not only investigated the influence of design parameters partly on selected properties of braided stents such as radial compression but also on the various required characteristics such as porosity and cover factor. But this study is limited to biaxial braids with only 16 yarn bobbins. Del Rosso et al [144] described the experimental identification of tensile behaviour of biaxial microbraids (number of yarns lower from 16) made of Kevlar or Dyneema. Their study showed that the braiding angle plays a fundamental role in determining the final properties of the dry microbraids. The higher the braiding angle, the higher the strain to failure. On the other hand, these authors showed that microbraids

having smaller braid angles have a stiffer response after jamming occurred with respect to those having bigger bias angles. The understanding of the tensile behaviour of braided materials was also the subject of research by Rawal [99,145–147], using the developments of models compared with experimental results.

Based on the discussion above, it is suggested that the mechanical behaviour of braided reinforcements cannot be deduced from the numerous studies dedicated to the behaviour of dry woven fabrics. In addition, it is still unclear whether the bias-extension test is adaptable for determination of in-plane shearing for braided fabrics since the geometrical conditions and the in-plane shearing characteristics under the condition of non-orthogonal fabrics are not clearly defined. In this case, the picture frame test is obviously no more adaptable because it would require the design and processing tested hinged frames for each braided angle, which is inconvenient and uneconomical. Furthermore, for triaxial fabrics, adding the yarns along axial direction could change totally mechanical behaviours, which need an in-depth study based on a variation of braiding angles. At last, in order to optimise the manufacturing process, especially for providing the appropriate temperature during forming process, the thermos-mechanical behaviours of braided reinforcements should be also explored under temperature variation.

1.3 The stage of preforming

The reinforcements would be beforehand preformed to the desired shapes before resin injecting during manufacturing composites with complex shapes as shown in Fig. 1.11. This stage is defined as the preforming process, which is the first step of the phases in LCM. Mastering the preforming quality of reinforcements is significant because it would heavily influence the properties of final composites. However, the composite reinforcements preforming is a difficult stage including the complex deformability behaviours such as yarns sliding, in-plane shearing behaviour, intra-ply sliding and material draw-in, which are influenced by many process parameters such as the preforming load, the initial orientation of yarns, the properties of yarns and the shape of tools [148]. Hence, it is complicated to precisely characterise the deformability behaviours during preforming stage. Moreover, the preforming defects observed at different scales (mesoscopic and macroscopic scales), such as buckling, wrinkling, and misalignment [149–152], are heavily associated with preforming behaviours. These defects can bring negative influences on the resin impregnation, and critical changes of the in-plane and through-thickness permeability [148,153,154].

Consequently, in order to produce the complex geometric composites without defects, it is important to acquire the deformability behaviours during the preforming process.

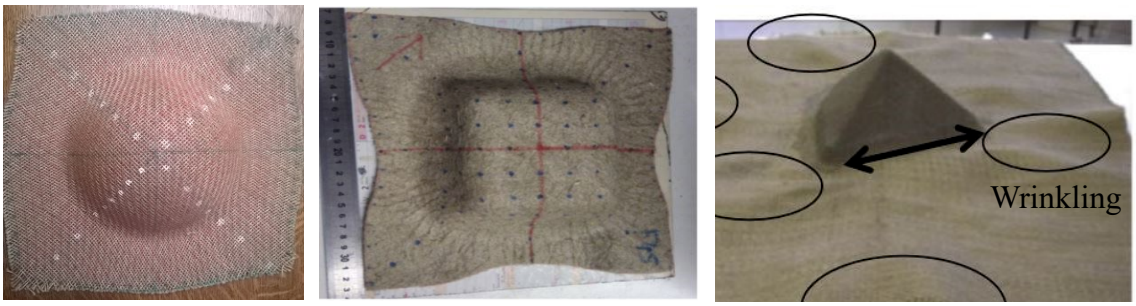

(a) (b) (c)

Fig. 1.11. Some typical preform shapes, (a) Hemisphere, (b) Square and (c) Tetrahedron

At present stage, the researches on deformability behaviours associated with defects mainly focus on the relationship between preforming parameters and characteristics presented by different behaviours, and trying to figure out the inherent relation among them then optimizing the preforming process. Wrinkling is one of the most common preforming defects at macroscale, caused by the effects on in-plane shearing and bending [132,155,156]. The methods such as finite element and experimental analysis are utilized to find out the correlation between the processing parameters like blank-holder pressure and wrinkle [132,150,155], and finally to optimise the preforming stage [133,157,158]. But the preforming defects characterised at macroscale or mesoscale are more difficult to quantify, in particular for the complex shapes with high curvatures and large deformations [159,160]. The sliding of the network, which can be defined as inter-ply sliding in multilayers preforming or yarn sliding in monolayer preforming, is another preforming behaviour that probably has a negative influence on the preforming quality. The inter-ply sliding denoted by the relative movements of the plies induces the local wrinkles [161,162]. In contrast, the yarns sliding depending on the blank-holder pressure is experimentally defined in [148] and could lead to the buckles as shown in Fig. 1.12 (b). Gatouillat *et al*. presented numerically that excessive sliding between warp/weft yarns can lead to a loss of cohesion in the woven network [163]. In this case, the tow or yarn orientation cannot be controlled during the preforming and the local fibre density decreases. Consequently, a decrease in local fibre density can influence the resin impregnation and may lead to the resin-rich zone in final composite parts, the mechanical properties hence are impacted undesirably.

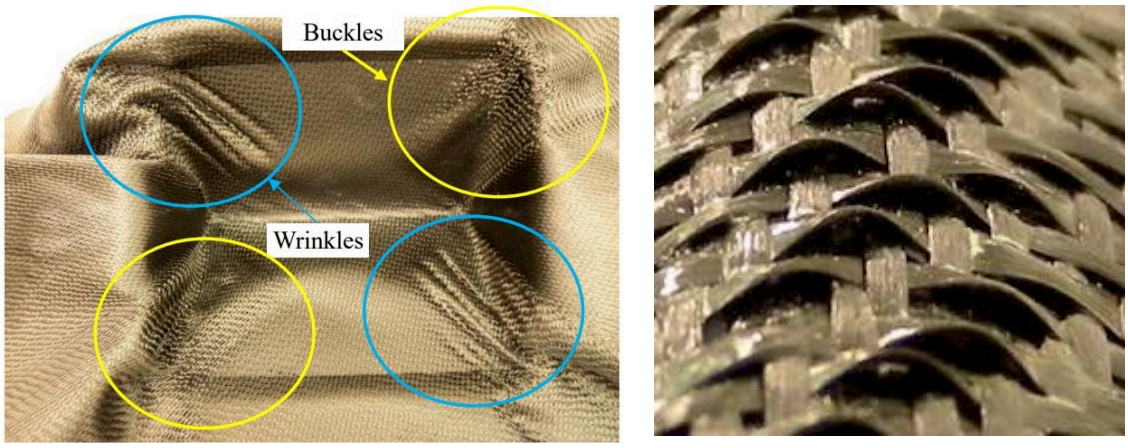

(a) (b)

Fig. 1.12. The performing defects: (a) Local wrinkles and buckles; (b) The amplification of buckles [161].

As same as discussion on mechanical behaviours of reinforcements, the preforming exploration in previous researches mainly concentrates on the woven fabrics, NCF(Non-crimp-Fabrics) or unidirectional prepreg laminates[155,164] with different punch shapes such as hemisphere [165–167], double-dome [158,168,169], eccentric cone [170], tetrahedral and square box [156,171–174]. The deformability behaviours show different magnitudes and profiles in such punched shapes. On the contrary, even though Jacquot *et al*. [175] compared the deformability behaviours of woven and biaxial braided fabrics manufactured from the same comingled flax/PA12 yarns on the hemispherical punch, there are relatively few research works dealing with the braided reinforcements preforming. Furthermore, as one of important parameters of braided reinforcements, the braiding angle could heavily impact the composites properties in terms of vibration behaviours, tensile strength and energy abortion [176–178]. Thus, it is reasonable to believe that deformability behaviours during preforming process would be varied by braiding angle selected. The optimization to avoid the certain preforming defects related to in-plane shearing behaviour such as wrinkling could be designed according to mechanism of deformability behaviours decided by braiding angle. However, such exploration on variation of deformability behaviours changed by braiding angle during preforming is still absence. In addition, the triaxial braided reinforcements with a specific structure possibly present the different deformability behaviours, compared to the classical biaxial textile fabrics (woven or biaxial braided fabrics). However, due to the lack of research of mechanical characters in deformability behaviours of biaxial fabrics, the difference between biaxial and triaxial fabrics in preforming process does not draw enough attention.

1.4 The composites machining by abrasive waterjet (AWJ)

The FRPs possess the advantages for lightweight design but also bring challenges to machining process due to anisotropy and abrasive properties. After manufacturing but before assembly process, the FRPs machining is unavoidable in most cases, for instance, drilling or cutting, for the purpose of satisfying the requirements in assembly process. Due to contact between cutting tools and materials, traditional processing technique, which is most common method in FRPs machining by now, probably result in a heat-affect zone which could degrade the fibre or matrix, especially which has the low thermostability. Although the innovations in cutting tools or process could enhance machining quality to some extent, the balance between the efficiency, machining quality and the cost is still the problem that the manufacturing of automobile, aircraft, etc. should reasonably and carefully consider. The non-traditional processing techniques as laser or electric discharge machining are also unadaptable for FRPs machining considering the same problem of the heat-affect zone.

Recently, abrasive waterjet (AWJ) processing technique, an emerging versatility and cool-machine method, has been gradually used in FRPs machining. AWJ uses high pressurized water mixed with abrasive particles through small diameter orifice nozzle to strike on and consequently remove materials by means of erosion mechanism. This processing technique could be theoretically fitted with almost all materials, especially for metal and glass which have been extensively studied during the past twenty years. Except for no heat-affect zone, AWJ also provides the advantages including minimal residual stresses and surface hardening on the materials due to small cutting force. Besides, the recyclable abrasives and water further reduce the cost and almost without pollution, attracting more and more attention from the machining field. In recent years, AWJ has been extensively applied into many processing methods such as cutting, turning, drilling and milling. Among them, the cutting processing is still the most widely accepted even though cutting performance including kerf taper or surface quality is undesired in certain cases.

Due to the advantages discussed above, AWJ cutting process has been widely studied by many researchers from many aspects. In early investigations of AWJ cutting, Hashish[179] proposed that the two cutting zones exist in processing ductile materials under AWJ based on the erosion mechanisms that were proposed by Finnie and Bitter [180–182]. The cutting zones in kerf wall are easily distinguished because of impacting angle at different angles as shown in Fig. 1.13(a). The upper zone of kerf wall is characterized by impacting at a shallow angle,

erosion proceeds as cutting wear which generates the smooth cutting zone (SCZ) that could relate to surface roughness. While the bottom of the kerf wall is represented by impacting at a large angle, the erosion is about deformation wear that produces rough cutting zone (RCZ), which is characterized by waviness or striations. D. Arola and M. Ramulu [183] also put forward an initial damage zone (IDZ) at jet entry based on an experimental investigation of composite cutting, which is due to jet expansion prior to impingement. The same phenomenon was also presented by Wang Jun [184] at the early research stage using the scanning electron microscope (SEM) to certify that bombarded area caused by high-energy particles exists at IDZ. The kerf taper, which is formed by wider entrance width and narrow exit width as shown in Fig. 1.13(c), is also made naturally because of characteristics of the jet [185] that the inner contoured regions of the jet at cross-section have higher velocities and are convergent, thus the particle velocity at inner contoured regions is high and decreases to the minimum at the nozzle wall [186]. The non-uniform material removal occurs that the kinetic energy of centre of the jet is higher than it at outer of the jet, resulting in the tapered cuts. The kerf width is dependent on the effective width of the jet, which in turn depends on the jet strength in that zone and the target material properties [187]. Particularly in hard-to-machine materials that cause the smaller effective erosion portion of the jet than it in relatively soft material.

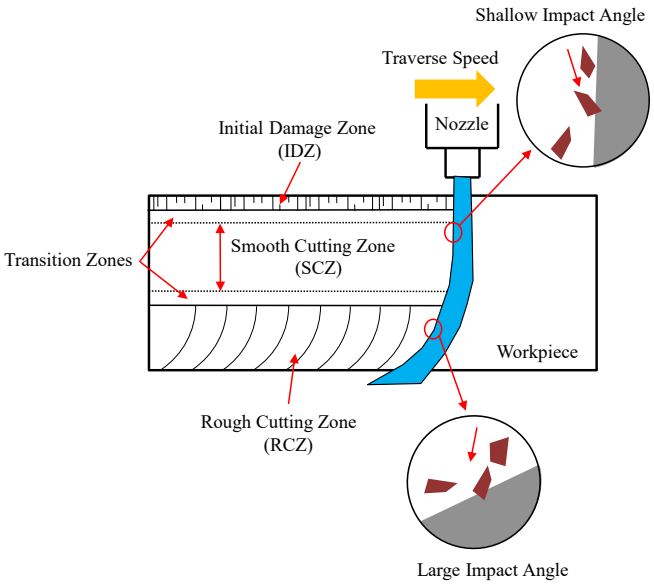

(a)

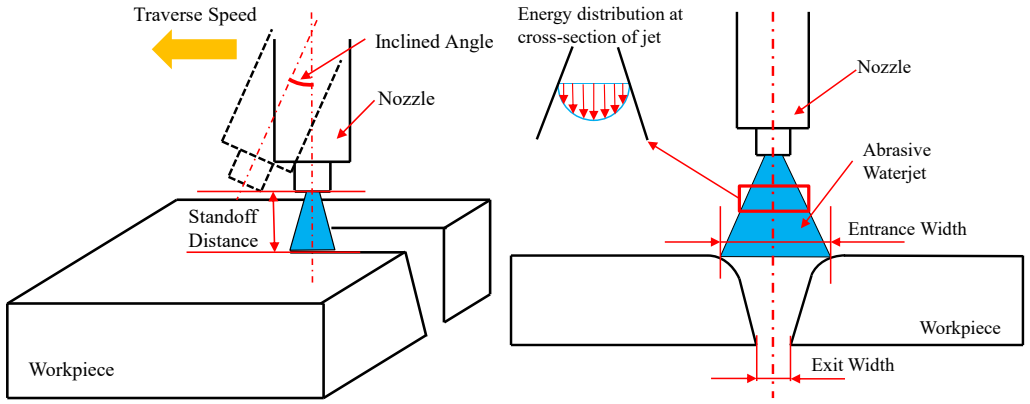

Fig. 1.13. The characteristics of AWJ, (a) the kerf wall properties, (b) the basic parameters in AWJ and (c) the kerf cross-section profile

Obviously, the striations at RCZ and kerf taper are undesired when using AWJ as the first choice to cut materials thoroughly. These defects are seriously influenced by process parameters and material properties. Generally, the easy-control parameters including pressure, standoff distance, traverse speed and abrasive flowrate are associated with entrance, exit width and different cutting zones, resulting in the kerf taper and surface quality. The ANOVA analysis and regression models are normally useful method to evaluate and predict the performance [183,188]. It is found that standoff distance is the most significant factor influencing the kerf width and taper at a limited thickness. High standoff distance could effectively decrease more the energy of jet prior to removal of materials than other parameters, and the jet expansion leads to widening the entrance width. In addition, the interaction effects of parameters are found to be insignificant. Surface quality is connected with traverse speed heavily because the overlap of particles reduces with increasing traverse speed, decreasing the effective erosion function in per unit [189]. Also, the type of particles is a relatively important effector on the surface roughness at SCZ based on the ANOVA analysis [190]. However, the influence of cutting parameters on the surface quality changes as a function of cutting depth [191]. It means thickness as the one properties of specimen has a significant effect on performance. Therefore, the qualitative analysis on kerf quality including taper and surface quality should be at a fixed thickness in order to investigate the relationship with parameters. Generally, under through-cutting the standoff distance is recommended at a constant and small range, i.e. ≤2mm [192]. In this case, to obtain expected kerf quality that the fixed thickness is less than the depth of SCZ, increasing pressure at low traverse speed is an efficient combination of parameters to improve cutting quality. Nonetheless, this combination is impractical in most cases from the view of economy.

The process improvements, such as nozzle planer tilting [189], lateral tilting [193], oscillation [194–196] and multi-pass cutting [197,198], as seen in Fig. 1.14, provide another way to enhance kerf quality. Especially for the multi-pass cutting, the repetitive cutting at the same kerf over two times in order to compensate the single pass limits, which is proposed by Wang Jun and D.M.Guo that this processing method could improve cutting quality and efficiency noticeably. Particularly for thickness materials, such as increasing smooth depth of cut and improving surface quality except for alternating the traverse direction. Meanwhile, it could also improve the efficiency and reduce the cost without any sacrifice. The main limitation of multi-pass, however, is standoff distance increasing as each cutting pass of material removed, and consequently, the effective jet width increases, which may influence the accuracy and quality of kerf. Moreover, the multi-pass is not applied in composites because of delamination defect associated with the non-through cut [185,189]. In laminated materials, repeated cyclic stresses, impact, and so on can cause layers to separate, forming a mica-like structure of separate layers, with significant loss of mechanical toughness [199]. The way to avoid the delamination during AWJ cutting is to select parameters properly, leading to through-cut at single-pass cutting. Apparently, it may reduce the efficiency and consume more energy that is occasionally undesired in practical application.

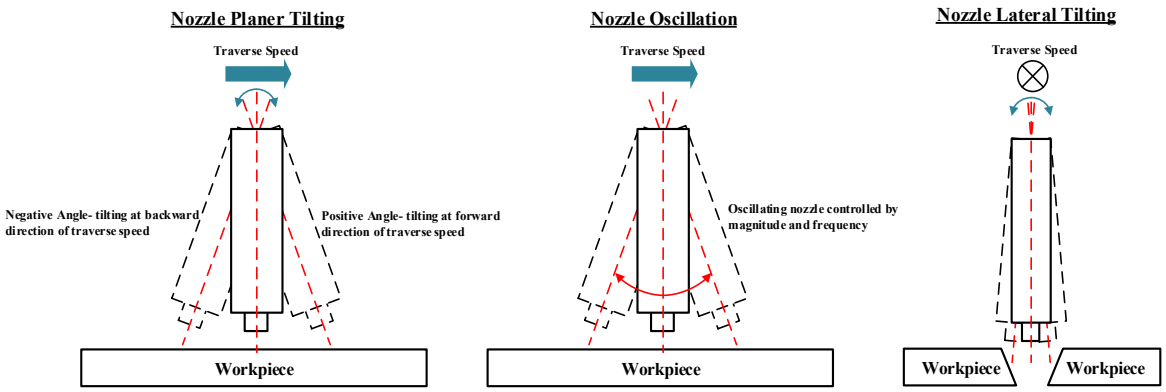

Fig. 1.14. The improvements in AWJ

Although via correlation analysis between processing parameters and objective cutting performance, it is not hard to acquire enough knowledge to guide workers who want the desired cutting quality. However, the root reason why selected parameters could insure the cutting quality is definitively decided by the material removal mechanisms (MRMs). Furthermore, the defects during machining, delamination for laminated composites, for instance, are also heavily related to MRMs. Thus, it is necessary to inquire the MRMs for different kinds of materials, especially for FRPs composites which consist of two different phases that could change material removal rate, consequently the defects would probably

occur. Only based on the MRMs exploration, the innovations in processing would be reliable. Unfortunately, the MRMs of FRPs by AWJ is still unfolded, and besides, the machining efficiency for composites using AWJ is not competent to mental or ceramic, which is also need to be improved.

1.5 Conclusion of Chapter I

The composites have been widely used with outstanding success in several industries for their lightweight, high specific stiffness, excellent corrosion resistance, fatigue resistance and impact resistance. Nowadays, composites manufacturing is experiencing a tendency from the lamination to parts with complex shape in order to further broaden its application areas. Chapter I facing this trend makes an extensive literature on the manufacturing FRPs composites with complex shapes and its corresponding machining properties.

The first part in Chapter I gradually discusses the basic conceptions, materials and techniques in manufacturing composites with complex shapes for the purpose of depicting the general background for this thesis. In the second part, the special aspect of mechanical behaviours of dry reinforcements is detailed because they are the principal mechanism during manufacturing composites with complex shapes. According to the literature reviewed in this part, it is clearly deduced that the woven reinforcements are still the primary ones that are utilized to manufacture composites with complex shapes. The other textile reinforcements produced by braiding technique do not acquire enough attention. In addition, the mechanical behaviours in braided reinforcements are heavily related to braided angle, which is the most important parameter in braided reinforcements and also the most primary difference between the woven ones, especially for triaxial reinforcements that the yarns are added along the axial direction. Besides, the thermo-mechanical behaviours also should be described in relation to variation of braided angle. Therefore, as the promising reinforcements for manufacturing composites with complex shapes, the braided fabrics need to be further explored and characterized in perspective of mechanical behaviours.

Secondly, the preforming process for reinforcements before resin injection, as one of the sequent processes of manufacturing composites with complex shapes, is reviewed with respect to deformability behaviours and defects during preforming. The deformability behaviours are associated with mechanical behaviours discussed in section 1.2, especially for in-plane shearing, and result in different types of defects such as wrinkles, buckles and uniform gaps. As same as discussion in second 1.2, the preforming exploration is mainly

focusing on the woven reinforcements, and trying to figure out the relation between the process parameters and defects rather than basic fabric parameters with deformability behaviours. Furthermore, due to the variation of braiding angle, the deformability behaviours would show the difference compared to woven ones, especially for triaxial braided reinforcements, which need to be determined qualitatively. The root cause of deformability behaviours is tension in each yarn during preforming, which also needs to be explored quantitatively, and can be predicted that the basic parameters of fabric would heavily impact the tension under the fixed punch shape.

Lastly, the composites machining by AWJ is roughly reviewed that the relation between processing parameters and cutting quality is the primary interest that could directly conduct the practice. Besides, the corresponding defects could also be avoided by optimizing processing parameters. However, the material removal mechanism is not totally known, and could not be introduced from metal machining because of anisotropy. Consequently, the improvement in composites machining efficiency without the sacrifice of quality still needs to be explored.

II. MECHANICAL BEHAVIOURS OF BRAIDED REINFORCEMENTS

2.1 Introduction

The mechanical properties of braided fabrics greatly impact the performance of composites with complex shapes. In this part, aiming to explore the mechanical properties of braided fabrics fabricated by natural and synthetic fibres, the mechanical model and its verification were investigated at first, and then, the braided parameters of fabrics including braided angle and number of fibre in axial yarn were studied in order to figure out their influence on the mechanical and thermal behaviours of the triaxial fabrics. Through the theoretical and experimental analysis in this part, the mechanical characteristics of preforms were fundamentally acquired.

2.2 An analysis of in-plane shear behaviours of braided preforms

2.2.1 Geometric condition

As described in the literature, a bias extension test is performed on a rectangular fabric [114,122–125,200,201]. For woven (orthogonally fabrics) warp and weft yarn directions are orientated initially at 45° to the direction of the applied load. The sample sizes are chosen differently for obtaining the pure shear zone. Since the yarns are free at both ends in the pure shear zone (zone C), the ratio r of length (L) (along the tensile direction) to width (w) is determined geometrically. Fig. 2.1 shows the sample with an initial angle β between the tows. During the bias extension test, it can be observed normally that the undeformed zone (zone A), the pure shear zone (zone C) and the zone where the shear angle is half that in region C (zone B). Generally, half of initial angle β is considered as the braiding angle, which is one of the important braiding parameters for analysing the mechanical preforms. Fig. 2.1 presents respectively the cases when a minimum and a larger pure shear zone are obtained. If a larger pure shear zone is obtained, it should use a longer specimen or a bigger ratio r (the width w remains constant). Consequently, the restrictive condition of bias extension test for any rectangular specimen can be described by Eq. 2-1 according to Fig. 2a:

$$r \geq 2\cot\left(\frac{\beta}{2}\right) \tag{2-1}$$

where r is the ratio L / w, so $r = L/w = 2\tan((\pi-\beta)/2)$.

The angle between tows (β) in a braided structure can be between 10° and 170°. For β equal to 90°, which means a woven structure, the Eq. 2-1 is simplified as Eq. 2-2. In this case, the

initial length of the specimen must be more than twice the width of the specimen that has been already shown in previous research [123–125,200–202]. Therefore, the bias-extension test can be achieved theoretically when the Eq. 2-1 is applied to define the size of samples of non-orthogonally fabrics.

$$r \geq 2 \tag{2-2}$$

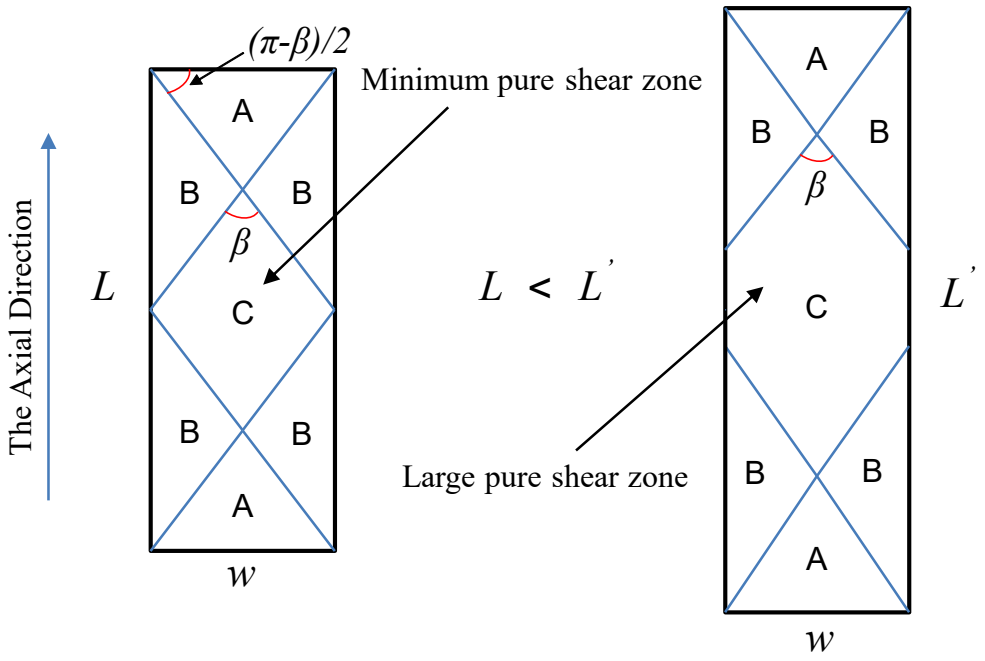

Fig. 2.1. A rectangular specimen of preform

2.2.2 Analytical model for shearing angle and moment

Fig. 2.2 shows the bias extension test for a braided fabric in initial and deformed conditions. The sample shows an initial angle β between the tows at the initial state ($10° < \beta < 170°$). When the clamping force is applied during the test, the tows rotate without sliding. The initial angle β decreases progressively to α as the clamping force F increases, generating a shear angle γ (Fig. 2.2b). The shear angle γ presents the difference between β and α ($\gamma = \beta - \alpha$). α can be described in the function of the length L, the displacement u and the width w of the sample in order to determine the shear angle γ.

$$\cos\left(\frac{\alpha}{2}\right) = \frac{(D+u)}{2L_C} \tag{2-3}$$

D and L_C are the diagonal and the edge of the rhombus of zone C in the initial condition. As the height of the triangle in zone A is constant and calculated by $L_1 = w / 2 \tan(\beta/2)$, it can be obtained D and L_C in the equations below:

$$D = L - \frac{w}{\tan\left(\frac{\beta}{2}\right)} \tag{2-4}$$

$$L_C = \frac{D}{2\cos\left(\frac{\beta}{2}\right)} \tag{2-5}$$

Finally, the shearing angle during the bias extension test can be demonstrated in Eq. 2-6.

$$\gamma = \beta - 2\arccos\left[\cos\left(\frac{\beta}{2}\right) + \frac{u\sin\left(\frac{\beta}{2}\right)}{L\tan\left(\frac{\beta}{2}\right) - w}\right] \tag{2-6}$$

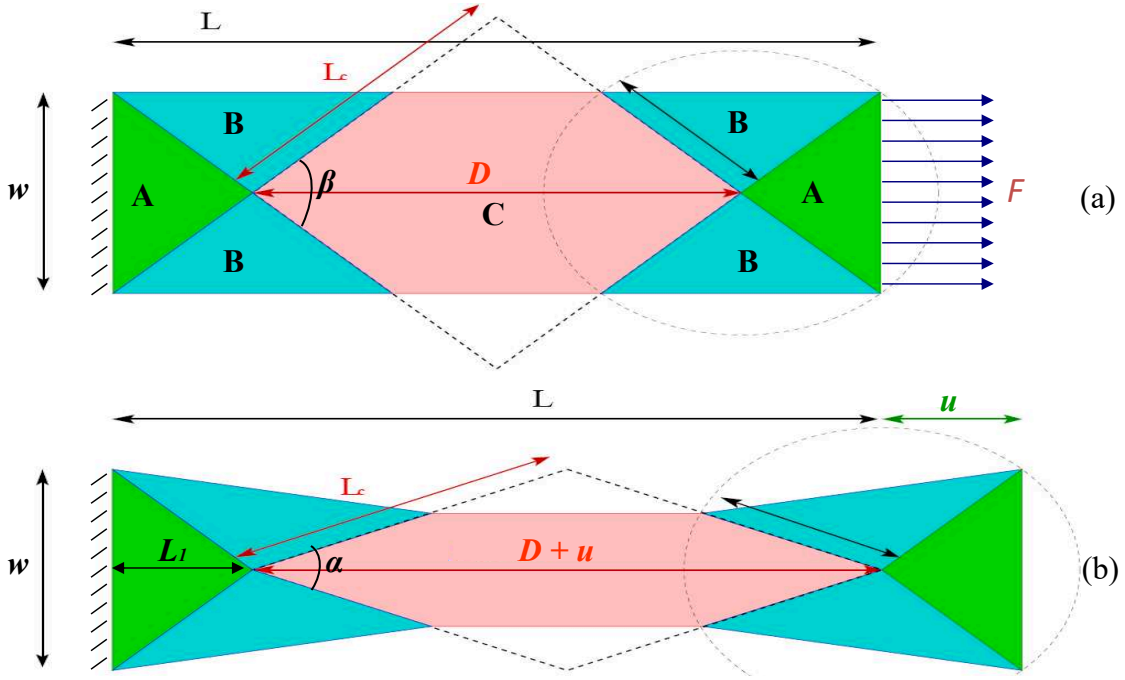

Fig. 2.2. Deformation of the braided preform sample during bias extension test, (a) initial state and (b) deformed state

During the bias-extension test, the power from the clamping load is dissipated in the semi-shear and pure shear zones (zones B and C) (Eq. 2-7). This gives the in-plane shear moment $M_s(\gamma)$ in function of the clamping force $F(\gamma)$ for a given shear angle (Eq. 2-8):

$$F(\gamma)\dot{u} = M_S(\gamma)\frac{S_C}{S_0}\dot{\gamma} + M_S\left(\frac{\gamma}{2}\right)\frac{S_B}{S_0}\frac{\dot{\gamma}}{2} \tag{2-7}$$

$$M_S(\gamma)=\frac{F(\gamma)\left[L\tan\left(\frac{\beta}{2}\right)-w\right]}{2\sin\left(\frac{\beta}{2}\right)\frac{S_C}{S_0}}\sqrt{1-\left[\cos\left(\frac{\beta}{2}\right)+\frac{u\sin\left(\frac{\beta}{2}\right)}{L\tan\left(\frac{\beta}{2}\right)-w}\right]^2}-\frac{S_B}{2S_C}M_S\left(\frac{\gamma}{2}\right) \quad (2\text{-}8)$$

where S_B and S_C are the original areas of the zones B and C in Fig. 3, S_0 is the surface of a unit cell in the initial configuration. $\dot{a}$ is the rate of quantity a .

If the initial angle between tows is 90° (β=90°), from Eq. 2-6 and 2-8 the expression of the in-plane shear angle γ and the in-plane shear moment $M_s(\gamma)$ can be simplified to Eq. 2-9 and 2-10, as presented in all works associated with woven preforms [122–126,129,135,200–208]:

$$\gamma=\frac{\pi}{2}-2\arccos\left(\frac{D+\mu}{\sqrt{2}D}\right) \quad (2\text{-}9)$$

$$M_S(\gamma)=\frac{\sqrt{2}F(\gamma)DS_0}{2S_C}\sqrt{1-\left(\frac{D+\mu}{\sqrt{2}D}\right)^2}-\frac{S_B}{2S_C}M_S\left(\frac{\gamma}{2}\right) \quad (2\text{-}10)$$

2.2.3 Experimental method and materials

Materials

Braided preforms are manufactured from two raw materials: Flax/PA12 commingled yarns and E-glass yarns. Flax/PA12 commingled yarns contain 64% of flax fibres and 36% of PA12 fibres (in mass fraction). The length of the flax fibres is 50 mm. The biaxial braided fabrics were produced by overbraiding on a braiding loom available at GEMTEX laboratory and described in [175,209]. Braiding process parameters were chosen to have a 30°braiding angle β/2. After the braiding, the fabric was cut and opened to obtain the braided preform sample (Fig. 2.3). It required more attention in these steps to master the braided angle. After the cutting and opening steps, the modification of braiding angle was weak [175] and remained equal to 30° (β/2). The main properties of the tested braids are listed in Table 2.1.

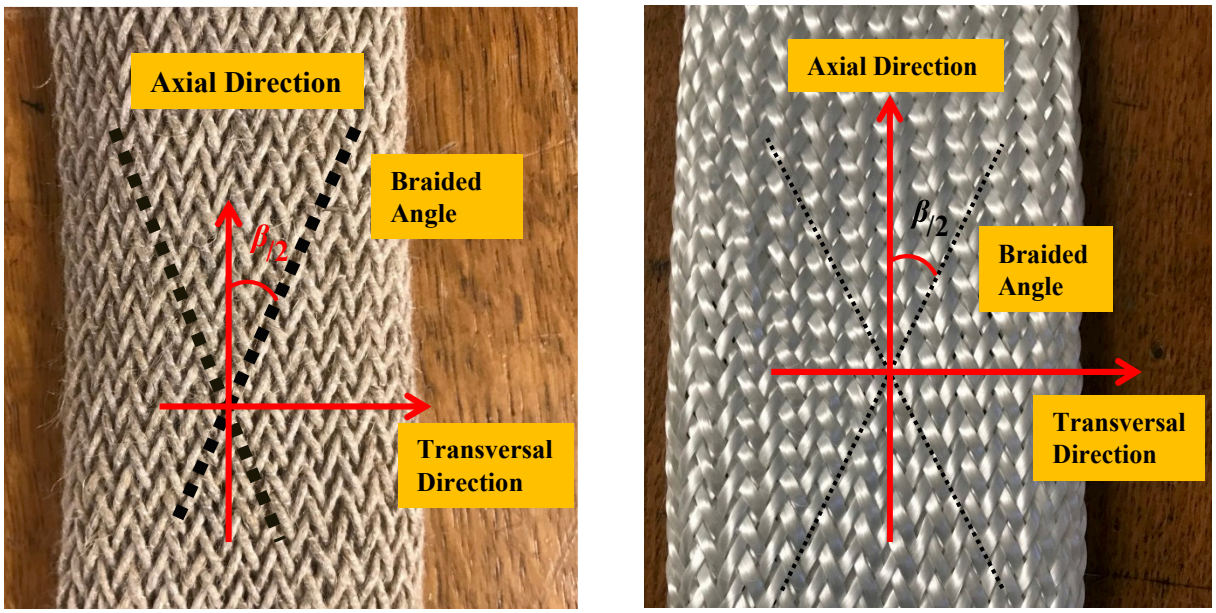

(a) (b)

Fig. 2.3. Tested preforms made by two materials after cutting and opening, (a) Flax/PA12 fibres reinforced braid and (b) E-glass fibres reinforced braid

Table 2.1. The main properties of the preforms

Parameters	Flax/PA12 fibres reinforced preform	E-glass fibres reinforced preform
Type of braid	Biaxial twill 2-2	
Yarns	500 tex	2350 tex
Area density of the fabric (g/m^2)	376 ± 5	1820 ± 5
Thickness (mm)	2.06	2.48
Braided angle (β/2)	30°	30°
Number of yarns per cm	4.2	2.4

Experimental set-up

The bias-extension tests used to determine the in-plane shear behaviour of braided reinforcements were performed by MTS Criterion Testing Systems. In order to achieve the measurement, the sample dimensions of the braided preforms must respect the geometric condition developed in section 2.1.1. Moreover, as non-orthogonally preforms, the braided structure is not symmetric in axial and transversal directions. Bias-extension tests must be performed in AD and also in TD to obtain the complete in-plane shear behaviour. As the braiding angle was chosen, it can be computed from Eq. 2-1: the ratio r must be greater than 2.8 for the tests in AD (concerning an angle between the tows β=60°) and the ratio r must be greater than 1.15 for the tests in TD (concerning to an angle between the tows π-β=120°) as

illustrated in Fig. 2.1. The definition of the in-plane shear angle γ was not changed; the observation was always in axial direction. During the bias-extension test in TD, Contrastively, the shear load and the displacement have positive values, but the shear moment and angle present the negative values.

In order to analyse the influence of the sample geometry on the in-plane shear behaviour, and in the range of limit values, several ratios r were considered. Table 2.2 lists the sample sizes in this study. r and D can be calculated according to the dimensions of each sample and the angle between the yarns (Eq. 2-4). All of the bias-extension tests were performed at a constant displacement rate of 50 mm/min. Moreover, the shear angle was measured directly by an optical measurement in the pure shear zone during the test. In this case, it could be performed a comparison between the theoretical and experimental models for each bias-extension test. As the limit of the braided preform dimension in TD (100 mm the maximum length in TD), a small sample was used, but it always respects the geometric criterion developed in Eq. 2-1.

Table 2.2. The characteristics of two preforms

Specimen type	Test direction	Fibres/Yarns	Length L (mm)	Width w (mm)	D (mm)	Ratio $\boldsymbol{r}$ (L/w)
N° 1	in AD	E-glass	245	70	123.68	3.5
N° 2			280	70	158.68	4
N° 3			350	70	228.68	5
N° 4	in TD		100	80	53.81	1.25
N° 5	in AD	Flax/PA12 commingled yarns	210	50	123.341	4.2
N° 6			240	50	153.34	4.8
N° 7			300	50	213.34	6
N° 8	in TD		100	70	59.58	1.43

2.2.4 Results and discussion

In this section, the bias-extension tests are carried out on two types of braided preforms with different ratios r presented in Table. 2.2. Each test is repeated five times to obtain an average data. Fig. 2.4 shows the non-deformed and deformed samples with Flax/PA12 and E-glass yarns reinforced braids. The three different zones are noted clearly in both types of preforms during in-plane shear tests. As presented above, there is no deformation in zone A. The stretching of the sample generates a pure in-plane shear angle γ in zone C and semi-angle $\gamma/2$ in zone B.

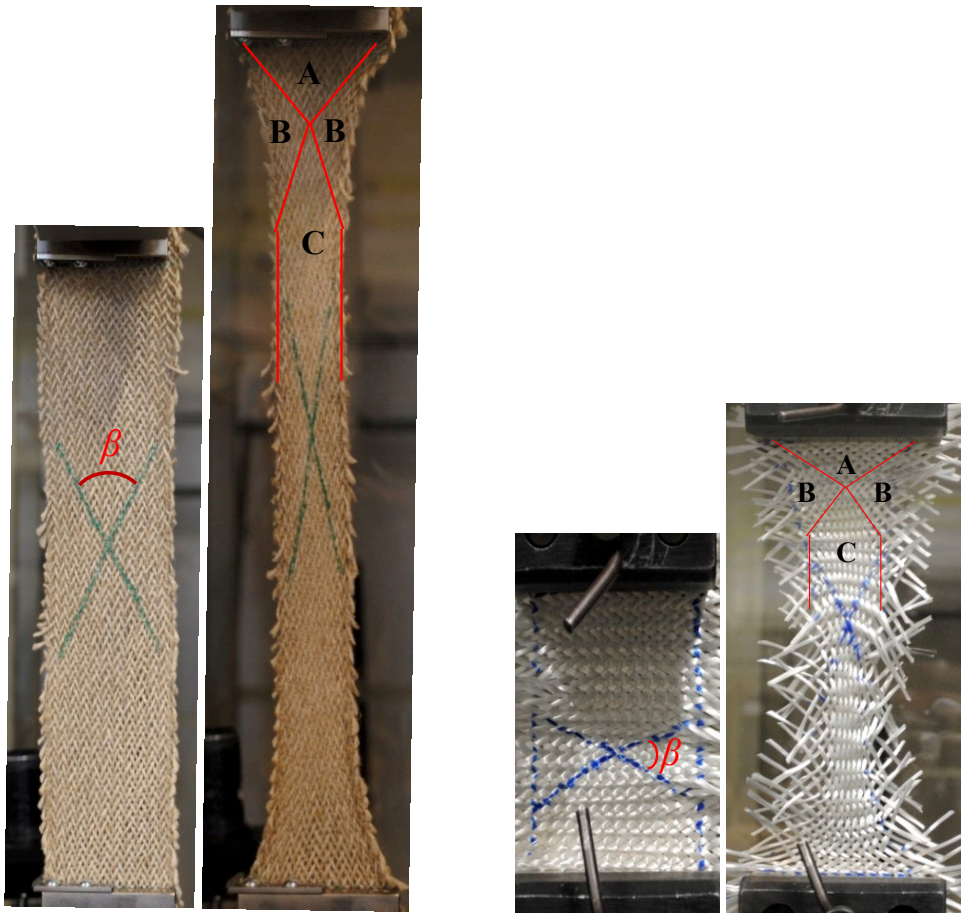

(a) (b)

Fig. 2.4. The preforms before and during bias-extension test, (a) Flax/PA12 braided sample in AD and (b) E-glass Braided sample in TD

In-plane shearing behaviour of braided preforms

Fig. 2.5 presents load-displacement curves for Flax/PA12 braided samples with different geometric ratios (r =4.2, 4.8 and 6) obtained by bias-extension tests in AD. The three curves have very similar profiles that can be divided into two parts before reaching the maximum shear load. At first, the load increases with increasing displacement in a weak stiffness until the displacement is approximately 12 mm for r =4.2, 17 mm for r =4.8 and 25 mm for r =6 (corresponding to the same shear angle about 23°). As the lateral contact and the transverse compaction of the yarns, the load increases consequently when the shear angle becomes larger and exceeds 23°, which is associated with the "locking angle" [114,123–125,200,201]. Over this limit value, the load soars rapidly with a small increase in shear angle owing to the impact stress generated by contacted bias yarns. During this time, the yarns begin to sustain the tension stress along the self-axis. Besides, the maximum in-plane shear load for three different ratios increases with an increase of the geometric ratio r. The big ratio creates a larger sample, which has the larger pure and semi in-plane shear zones.

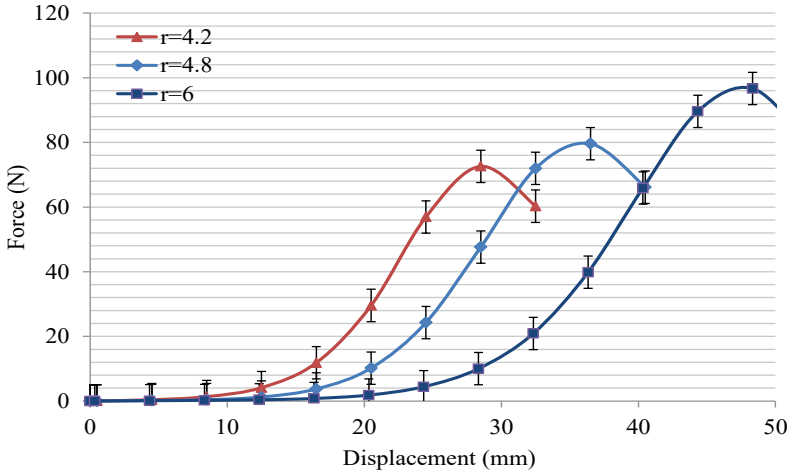

Fig. 2.5. Load vs. displacement in AD for Flax/PA12 braided samples with different geometric ratios *r*

The in-plane shear load versus the displacement curves in AD for E-glass braided samples with different ratios *r* is shown in Fig. 2.6. The curves have a profile that is different from the one figured out in Fig. 2.5 due to the different width of the yarn. The glass yarns are much wider than the Flax/PA12 commingled yarns, which take up the space that interlaced yarns need during in-plane shearing. Hence, the lateral contact of the yarns begins to compress each other almost at the onset of the test. Thus, the in-plane shearing load increases rapidly at the initial stage and then increases slowly before reaching the maximum load. Because more yarns present in the Flax/PA12 braided sample (21 yarns) compared to the glass one (17 yarns), the maximum in-plane shear load of the Flax/PA12 braided sample is higher than anyone of the glass braided samples. As presented previously, the bigger ratio *r* produces a larger area that can bear more shear load. Consequently, the maximum shear load could be observed for a larger sample no matter what kind of material it is.

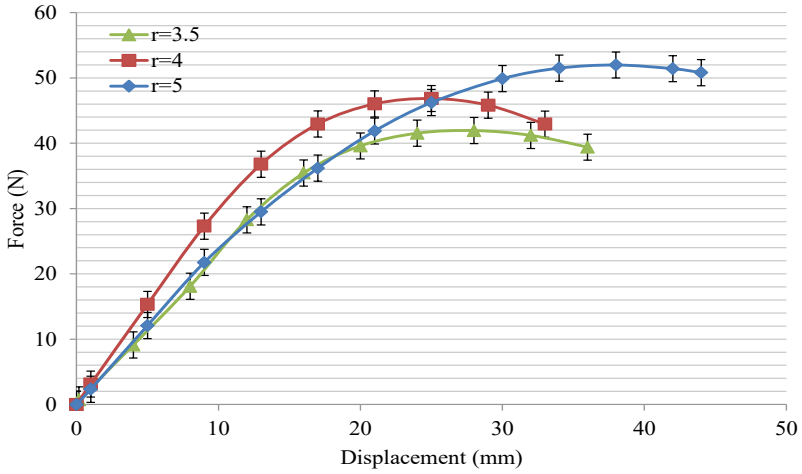

Fig. 2.6. Load vs. displacement in AD for E-glass braided samples with different geometric ratios *r*

The shear moment in function of the shear angle in AD for Flax/PA12 braided samples with different geometric ratios *r* is shown in Fig. 2.7. This function is calculated from Eq. 2-8. The shear moment increases following the augmentation of the shear angle. Three curves present a quasi-identical non-linear progression in spite of the small gap in increasing shear moment. It means that the shear moment/shear angle behaviour does not change following the variation of the geometric ratio. The geometric ratio only influences the shear load/displacement curve. Therefore, it can be said that the shear moment/shear angle behaviour resulted by bias-extension test does not change with varying ratio of length to width for braided structure.

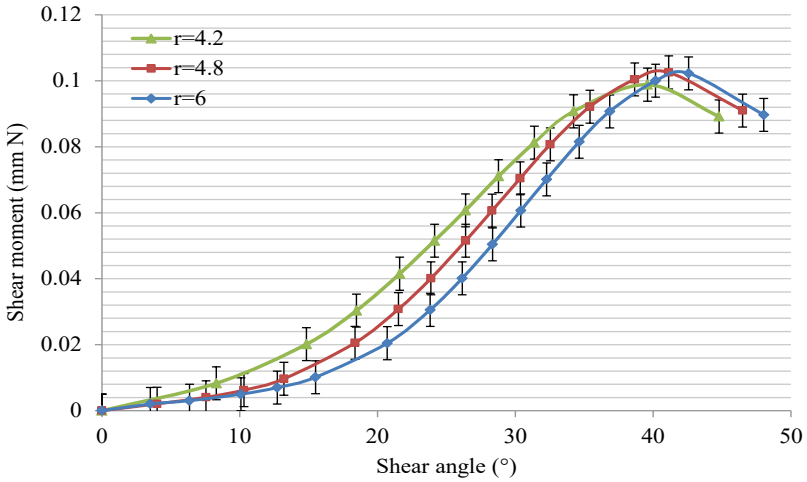

Fig. 2.7. Shear moment *vs.* shear angle in AD for flax/PA12 braided samples with different geometric ratios *r*.

Fig. 2.8 presents the shear-moment versus shear-angle curves in AD for E-glass braided samples with different geometric ratios *r*. Three curves show the same shear moment/shear angle behaviour considering the standard deviations. As the explanation made for shear load/displacement curves, the different progression of the shear moment/shear angle curves can be noted between the flax/PA12 braided sample and the glass one. The results confirm again that the variation of the sample geometric ratio does not influence the shear moment/shear angle behaviour of the braided fabrics.

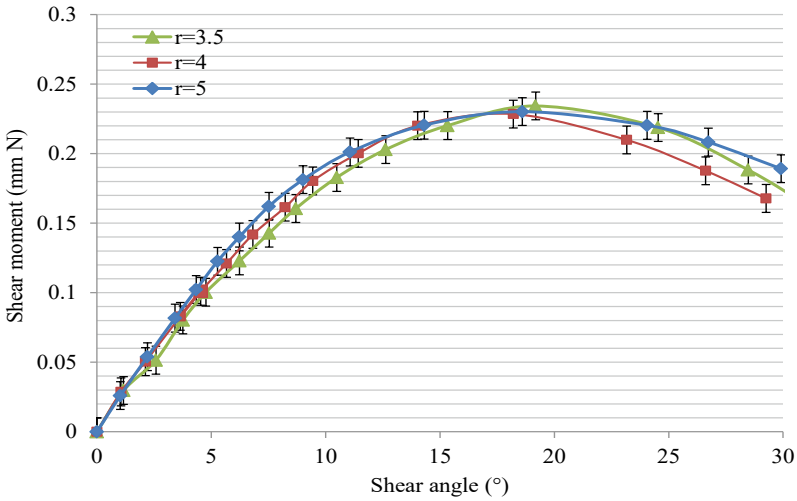

Fig. 2.8. Shear moment *vs.* shear angle in AD for E-glass braided samples with different geometric ratios *r*.

As presented previously, the braided structure is not symmetric in axial and transversal directions (AD and TD). The bias-extension test in TD is indispensable to obtain the complete in-plane shear behaviour of the braided preforms. The shear moment in function of the shear angle curves for two types of samples in TD are presented in Fig. 2.9. In order to analyse this phenomenon conveniently, the shear moment/shear angle in AD is selected into the same figure. As the shear moment/shear angle does not change with the variation of geometric ratio, only one curve is presented in Fig. 2.9. Compared between the results in AD and TD, the tendency of the curves is very similar for the same type preform. On the contrary, the maximum shear moment and shear angle are changed. Especially for glass preforms, the maximum shear moment in TD almost has 72% less than in AD (Fig. 2.9b). In contrast with Flax/PA12 fabrics, the maximum shear moment in TD is slightly bigger than it in AD. Regarding the maximum shear angle in TD is much bigger than in AD, it shows the non-symmetric in two directions. Moreover, the difference in the maximum shear angle is not changed between flax/PA12 and glass fabrics in the same direction (20°). The 20° difference in both AD and TD is always due to the difference in the width of two types yarns.

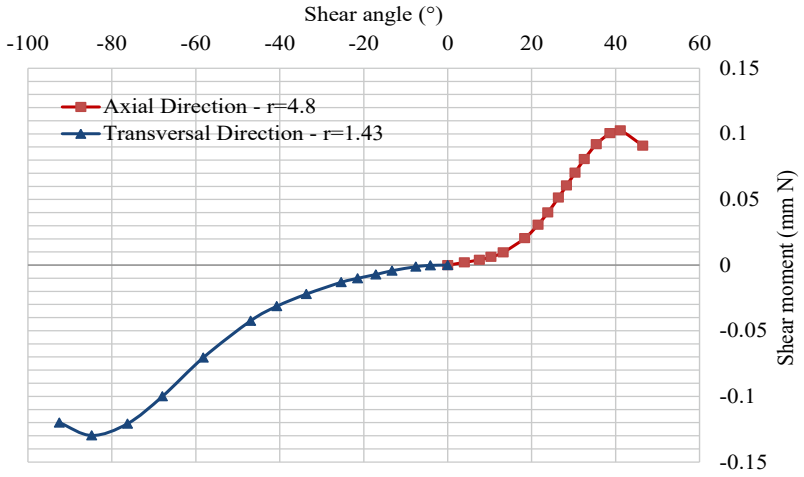

(a) Flax/PA12 braided preform

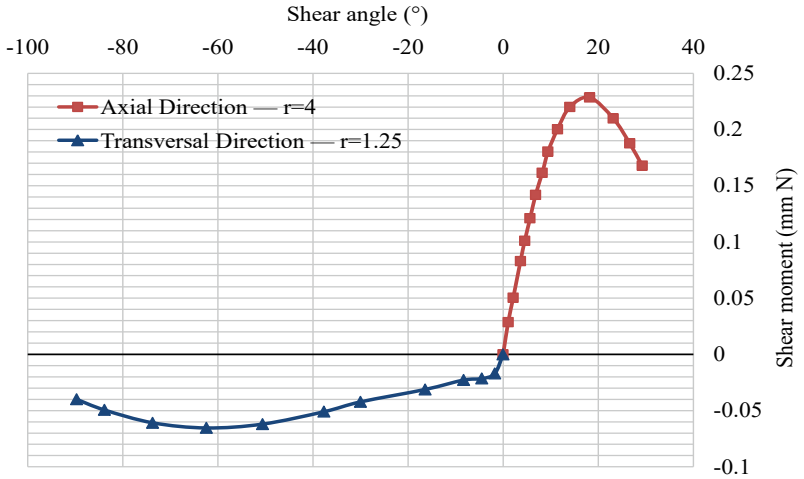

(b) E-glass braided preform

Fig. 2.9. The complete in-plane shearing behaviour for braided preforms

The theoretical models verification

The real in-plane shear angle is obtained by optical measurements during the bias extension test to verify the theoretical model presented in Eq. 2-6. The experimental and analytical correlation of in-plane shear angle in AD for Flax/PA12 and E-glass braided preforms with different dimension ratios is shown in Fig. 2.10 and Fig. 2.11. In addition, the theory calculation can be applied no matter in AD and TD, and the braiding angles in these two directions are complementary. Thus, the comparison between experimental results and theoretical calculation can be performed in only one direction (AD direction), which is enough to verify the accuracy of theoretical derivation.

In Fig. 2.10, it can be clearly observed that the theoretical and experimental curves separate approximately at 23° when the geometric ratios are 4.2 and 4.8, which is slightly bigger than it at r =6 that separates at nearly 18°. Meanwhile, the displacement for different ratios that theoretical and experimental curves separated obviously is almost identical to the ones that

load force begins to increase rapidly. It is further confirmed that the yarns sustain the in-plane shear force before the theoretical and experimental curves separate clearly. The reason for the difference between theoretical and experimental results is attributed to the yarns width that influences the variation of initial angle β. Compared with E-glass braided fabrics, it can be observed that the theoretical and experimental curves separate at 15° (see Fig. 2.11), which comes earlier compared to Flax/PA12 braids on account of the larger yarns width. Thus, the E-glass fabrics reach "locking angle" with less variation of initial angle and the shear angle has little change when the yarns start to bear the tension stress until tests finish.

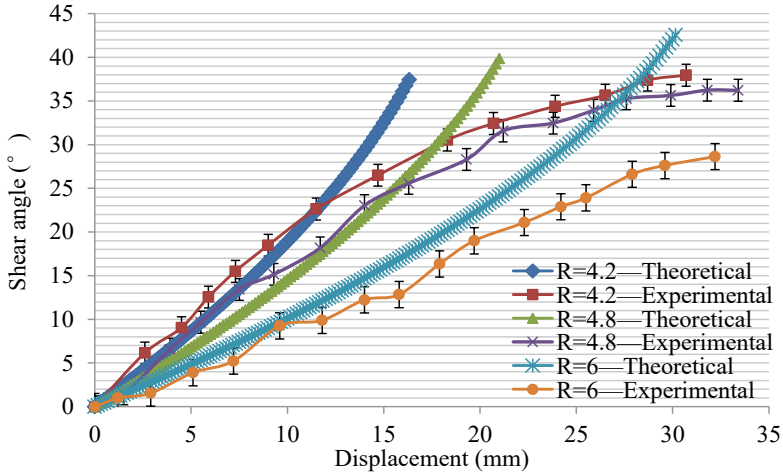

Fig. 2.10. Comparison between the theoretical models and experimental results for Flax/PA12 braided preforms

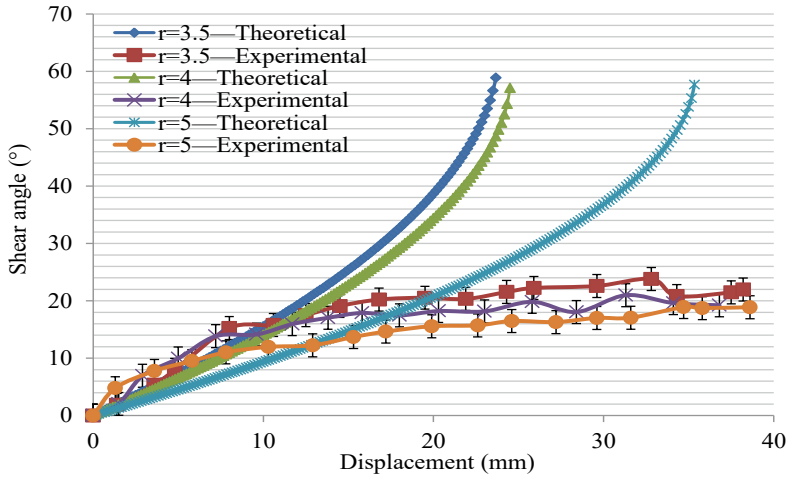

Fig. 2.11. Comparison between the theoretical models and experimental results for E-glass preforms

2.3 The influence of preforms parameters on mechanical and thermal behaviours of tubular braided reinforcements

2.3.1 Materials and methods

A multifilament UHMWPE yarn including 48 filaments(fibres) was used (density of 0.97 g/cm^3) in these tests and its specifications and mechanical properties are given in Table 2.3. This characterization is necessary to regulate the tension during the braiding process.

Table 2.3. Properties of ultra-high-molecular-weight polyethylene [19]

Properties	Value
Linear density (Tex)	169
Strain at break (%)	3.9
Tenacity (cN/Tex)	265
Twist (tr/m)	0

The structure of triaxial braided fabrics can be seen Fig. 1.7, which were fabricated by GEMTEX laboratory as seen in Fig. 2.12. The maximum number of carriers of the braiding loom used was 96 for bias yarns and 48 for the axial yarns. For this study, three UHMWPE multifilaments were used per bobbin of bias yarns and consequently, the number of bias fibres is constant and equal to 288. For axial yarns one, two and three UHMWPE multifilaments were used per bobbins to consider respectively 48, 96 or 144 axial fibres. In our denomination of braided samples, the two firsts number are respectively related to these numbers of bias yarns (first number) and axial yarns (2nd number) and they are expressed by the ratio of 48. The third number is related to the braiding angle. For example, a sample denoted 6-3-48 is a braid with 288 (6×48) bias yarns, 144 (3×48) axial yarns and with a braiding angle of 48°. The braiding angle can be controlled by varying the speed settings of the braiding loom. The braiding angle is thereby linked to process parameters by the following equation:

$$\beta = \arctan\left(\frac{\omega D}{NV}\right) \tag{2-11}$$

Where N represents the number of horn gear on the machine, ω is corresponding carrier rotational speed during braiding process. D is the diameter of tubular braided preforms and V expresses the production speed. The three patterns to illustrate the tubular braided preforms in such tests are presented in Fig. 2.13 in which the fabrics with braiding angle 45° as the example. The large range of braiding angle chosen is separated into three groups noted as small, middle and large, respectively. Table 2.4 shows the detailed information of samples.

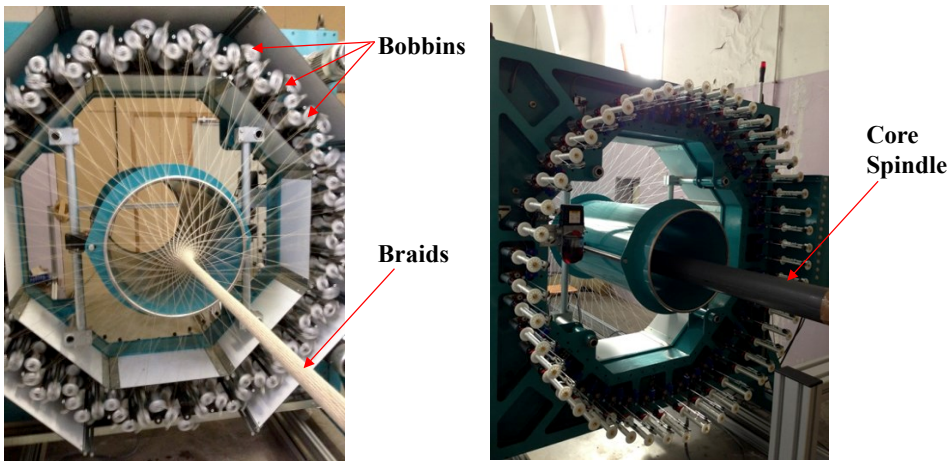

Fig. 2.12. Braiding machine in GEMTEX laboratory

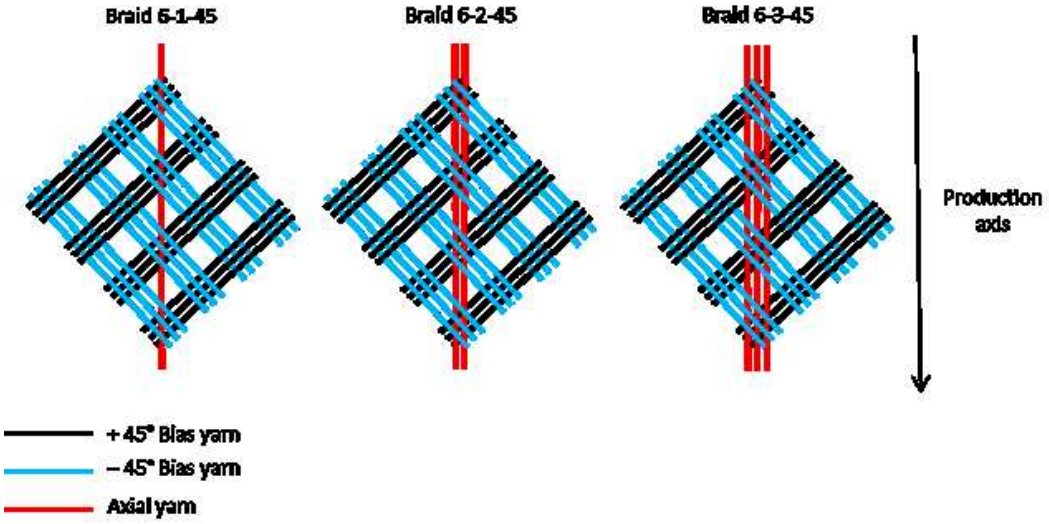

Fig. 2.13. The braiding pattens as braiding angle 45°

Table 2.4. The nomenclature of triaxial preforms

Name of samples	Group
6-1-12 6-2-12 6-3-12	Small
6-1-20 6-1-29 6-2-21 6-3-23	Middle
6-2-42 6-2-68 6-3-48 6-3-54	Large

The braiding angles were not only measured during the braiding process but also when braids were removed from the braiding machine. These measures were realized by optical techniques. Pictures of braids were taken by a camera and these pictures were analysed using the ImageJ software to compute an average of values at different places along the width and the length of

the sample. A statistic study was made to ensure the accuracy of measurements (precision of ±0.55°).

Additionally, the geometrical property (braiding angles) uniaxial tests on dry braids were conducted on an Instron tensile machine with a 250 KN load cell. According to the standard NFISO 13934, the test speed was 20 mm/min (Fig. 2.14). Ends of the sample were maintained by jaws realized with resin Epoxy and UD glass in order to avoid the sliding under the grips of the tensile machine. All the tensile tests were conducted in the axial direction. The yarns were maintained between the grips of the device and consequently, they were subjected to the tensile load. Axial yarns were oriented in the tensile direction, bias yarns presented one angle to the tensile load at the beginning of the test as the initial braiding angle. Results were obtained from the analysis of 10 samples tested for each configuration. The evolution of the braided angle was monitored by a camera positioned in front of the machine during tests. Furthermore, a thermal camera measured temperature during tensile tests by pointing on the sample. The viewable picture is described in Fig. 2.15. The temperature was measured in the centre of the sample. Towards the end of the test, the hottest point was usually no longer in the centre of the fabric. The value of the highest temperature in the frame was accepted. The measures are precise to ± 0.1°C.

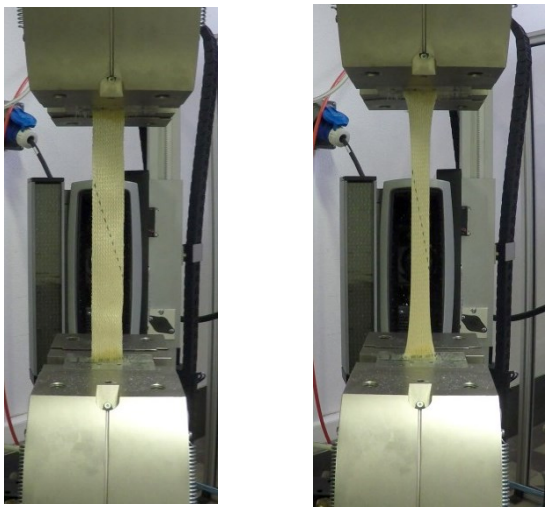

Start Before broken

Fig. 2.14. Test machine with preforms

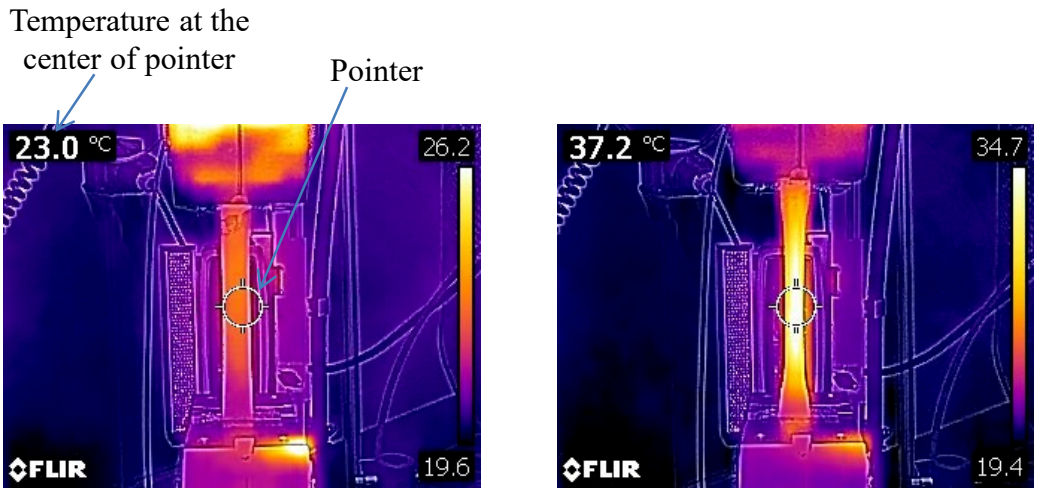

Fig. 2.15. Thermal behaviour conducted by the thermal camera during the test

2.3.2 Results and discussion

Tensile behaviour

The load/deformation curves with error bars associated with the samples are presented in Fig. 2.16. These results are clearly presented for the three groups depending on the range of the braided angle as discussed above (and denoted by “Large”, “middle”, “small” as defined in Table 2.4). Firstly, the samples with larger braiding angle are characterized by high tensile deformation contributing to high energy absorption, which could explain their application in ballistic protection [210]. Secondly, the tensile behaviour of triaxial braids is characterized by a “double peak” phenomenon. As explained by Duchamp et al. [209] during the test, axial yarns aligned in the load direction are directly subjected to the tensile load, The first peak is related to the break of axial yarns and the second part of the curve is associated to the in-plane shearing behaviour of the bias yarns. Depending on the braiding angle value, the second part of the curve can be characterized by a non-linear zone associated with the rotation movement of the bias yarns as intensively described for the in-plane shear behaviour of woven [125]. At the second peak, all the yarns slide that the load decreases.

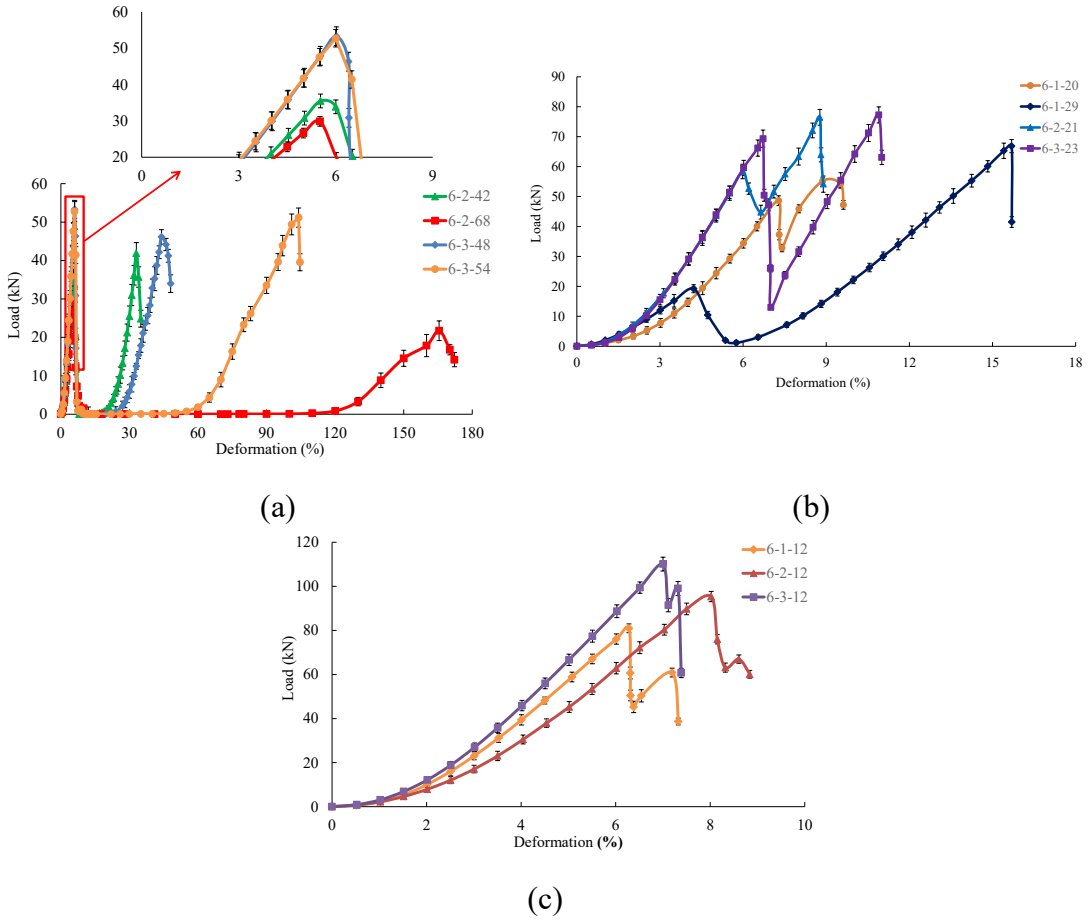

Fig. 2.16. The tensile behaviour for three groups of braided samples, (a) large, (b) middle, (c) small

Due to the range of braiding angle, however, the double-peak phenomenon is different. For large braiding angle (Fig. 2.16a) the first peak is reached around 5% of strain but the second peak is reached slowly and approximately until 150% of strain (6-2-28 sample). In the smaller braiding angle group (middle or small), the whole deformation decreases obviously and the first peak has more deformation than the second peak. Especially for the small braiding angle (12°), the two peaks become closer. It can be explained by the fact that axial and bias yarns are both subjected to the load at the same time since the braiding angle is so small that bias yarns are close enough to instantly lateral contact and compression, leading to the larger force in samples with the small braiding angle. The influence of braiding parameters (braiding angle and number of axial yarn fibres) on the maximum deformation and load can be further analysed in Fig. 2.17, respectively. Maximum deformation values from these tensile tests are presented in Fig. 2.17(a). The exponential increase of the maximal deformation in function of the braiding angle is illustrated independently from the number of axial yarn fibres. On the contrary, the braiding angle in function of the load at second peak shows a decreasing trend significantly in Fig. 2.17(b).

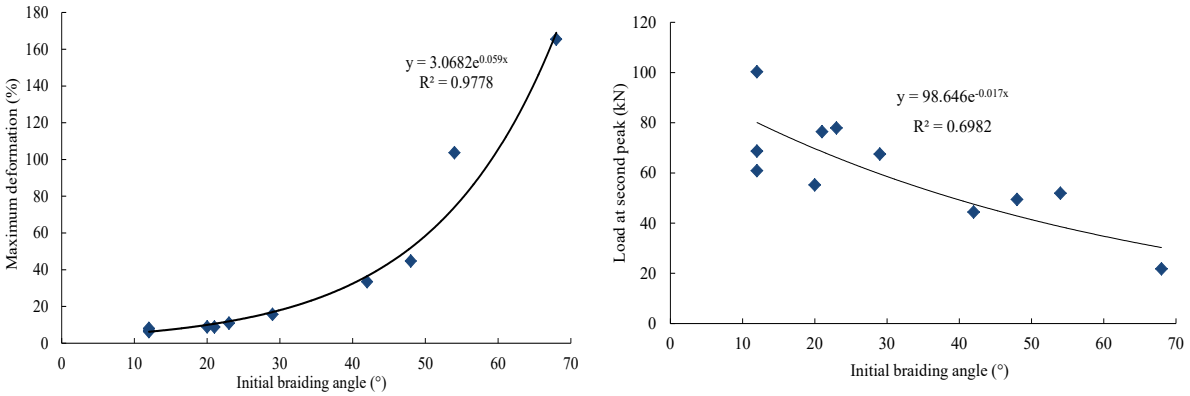

(a) (b)

Fig. 2.17. Influence of braided angle on (a) maximal deformation, and (b) maximal load at the second peak

The influence of the number of axial yarn fibres on values of maximal load at the first peak is shown in Fig. 2.18. The increasing load values with the increasing number of axial yarns is significant that can be illustrated by samples with the almost same braided angle. For samples with an angle 12° (or around 20°), a ratio of 2 in the number of axial yarns approximately involves a 20% increase of the load. For the constant number of axial yarns in the preforms, it can be inferred that the maximal load at the first peak increases with the decreasing braided angle. Therefore, the first part of the tensile behaviour (first peak) cannot be only associated with the contribution of the axial yarns in the direction of the load applied. In Duchamp 2018 [211], contributions of the bias yarns have been proposed by models defined in TexMind Braider Software.

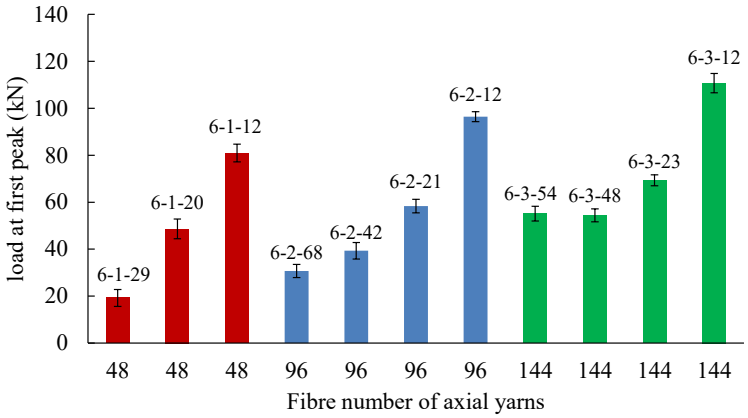

Fig. 2.18. Influence of the number of the axial yarns on the maximal load at the first peak

Evolution of braiding angle during tensile tests

Due to the measurements during tensile tests, the results of the evolution of braiding angle in function of the deformation with error bars can be presented in Fig. 2.19. The results are divided naturally according to the three groups of braiding angle. In each group, the final

value reached by the braiding angle at the end of the tensile test is clearly noted. It is noticeable that all the samples have an identical final braiding angle between 8°-13° independently from their braiding angle. This final angle between bias yarns in the load direction is related to the width of the material used (linear density, Table 2.3) and the available space. From the experimental results, it could be expected that the evolution of larger braiding angle accompanies high deformation, but the inverse trend presented by smaller braiding angle (clearly seen in Fig. 2.19c).

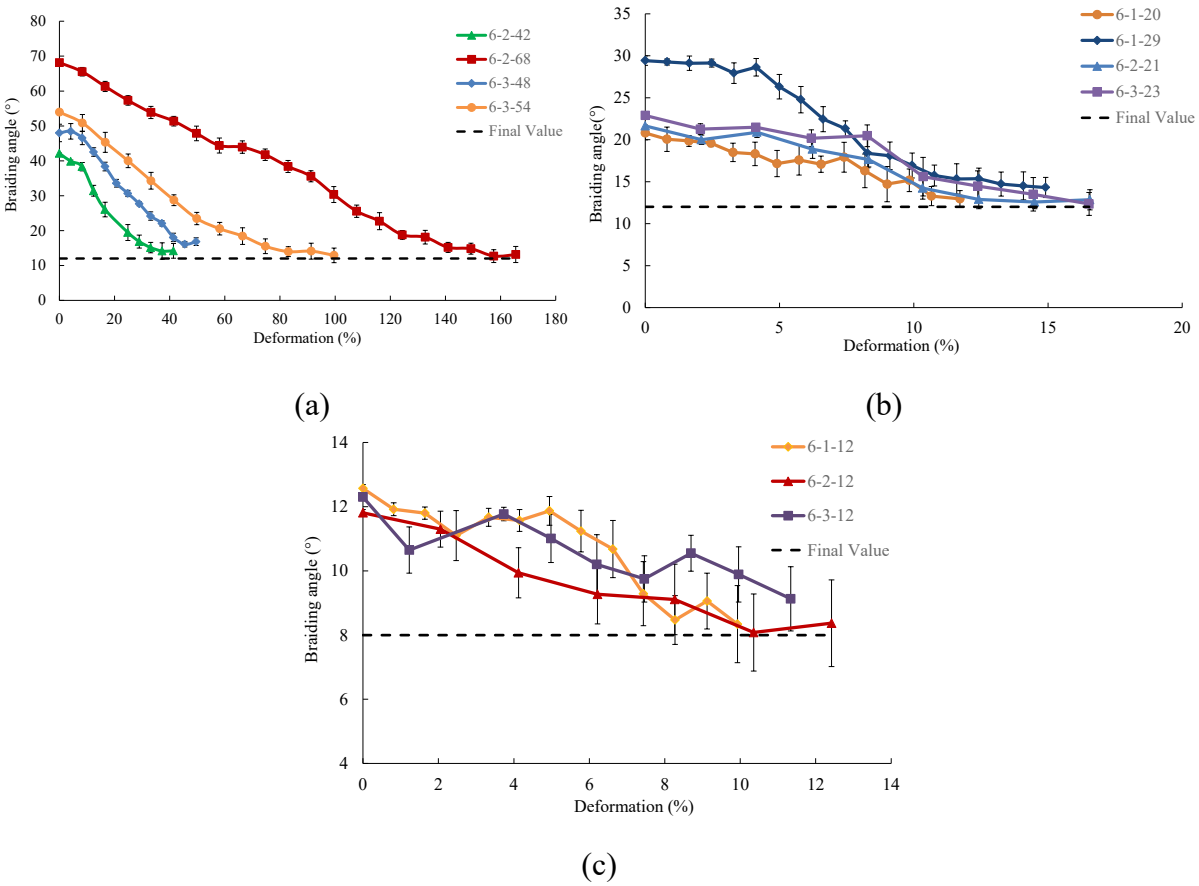

Fig. 2.19. The evolution of braiding angle during tensile test, (a) large, (b) middle and (c) small

The evolution of middle braiding angle can be clearly divided into two parts as shown in Fig. 2.19(b). In first part, the evolution of the braiding angle decreases with smaller slope before reaching the first peak of load since a small portion of load is assigned to bias yarns. A second part, however, the evolution has a relatively great decreasing trend with higher slope until the final value. The first part also should be clearly shown in large braiding angle, but the deformation at first peak is too small to be observed directly compared to the whole high deformation in Fig. 2.19(a). Comparatively, the evolution of small braiding angle is different from it in the larger group since this decreasing trend seems to be linear. It could further confirm that the axial yarns are the primary part to sustain the tensile force while the bias

yarns also bear load at a relatively small extent. Whereas, this small extent would influence the evolution of braiding angle heavily if the triaxial braids are designed with the small braiding angle. Hence, the linearly decreasing trend of braided angle could be seen at the beginning of the test (see Fig. 2.19c).

Thermal characteristics during tensile tests

The evolutions of temperature in samples during tensile tests for different braiding angles with error bars are presented in Fig. 2.20 respectively. It is clearly observed that the temperature increased drastically during the test. This phenomenon is related to the friction between yarns. The results presented by Fig. 2.21 show that the maximal temperature is reached for triaxial fabrics with the larger fibre number of axial yarns when triaxial braided samples have an almost identical braiding angle (6-1-12; 6-2-12; 6-3-12 or 6-1-20; 6-2-21; 6-3-23). It is due to incremental frictions when increasing fibre number of axial yarns. The maximal temperature reached by samples with middle or small braiding angle is higher than it with the large braiding angle as the number of axial yarns is fixed. This is probably because the axial and bias yarns simultaneously bear the load which can directly increase the local friction, and the evolution of temperature in smaller braiding angle has inefficient space and time to dissipate the heat that increases the local temperature. Thus, the temperature has inversely proportional to braiding angle.

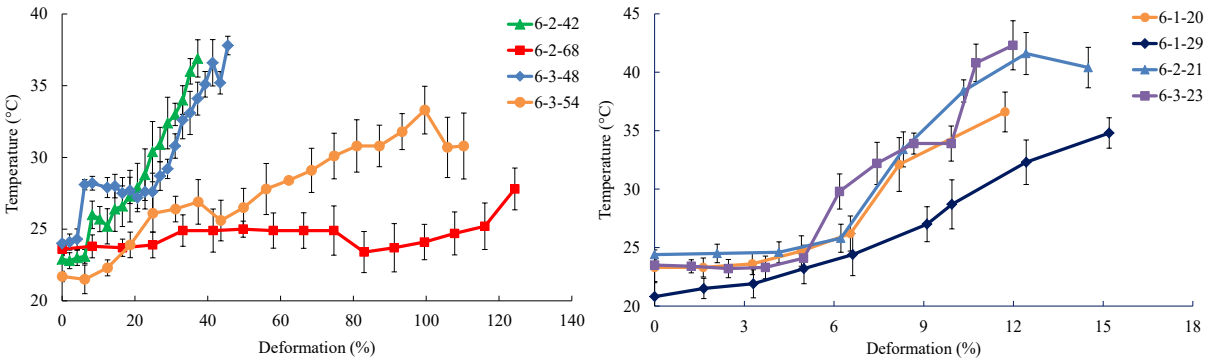

(a) (b)

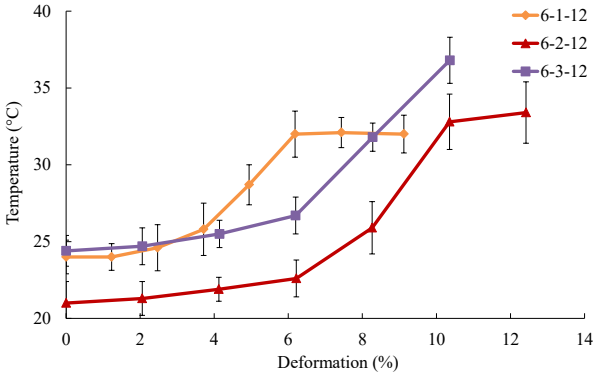

(c)

Fig. 2.20. The temperature evolution with different braiding angle during tests, (a) large, (b) middle and (c) small

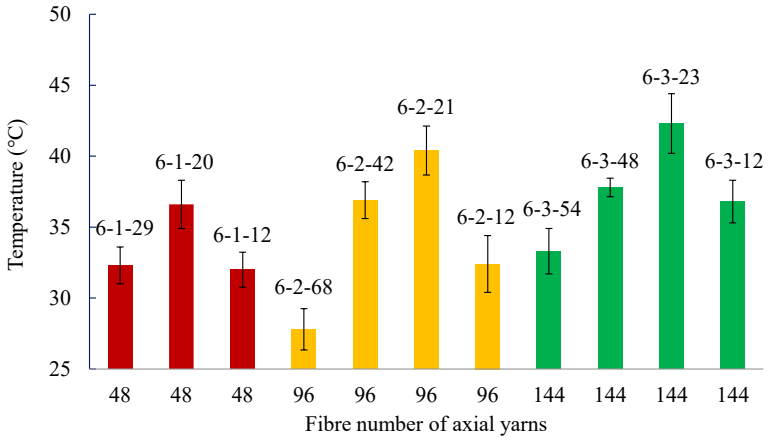

Fig. 2.21. Maximum temperature in function of number of axial yarns

To further analyse the thermal characteristics during the test, the relationship between strains, the evolution of load and temperature for two samples of middle and large groups are shown in Fig. 2.22. As presented previously, the average curves were obtained from 10 tests. For the sample with the middle braided angle, it can be deduced that the increase of the temperature maintains in a relatively small degree during the first peak of load evolution (about 4°). After the first peak, the temperature increases rapidly and almost follows the trend of load evolution to reach the second peak.

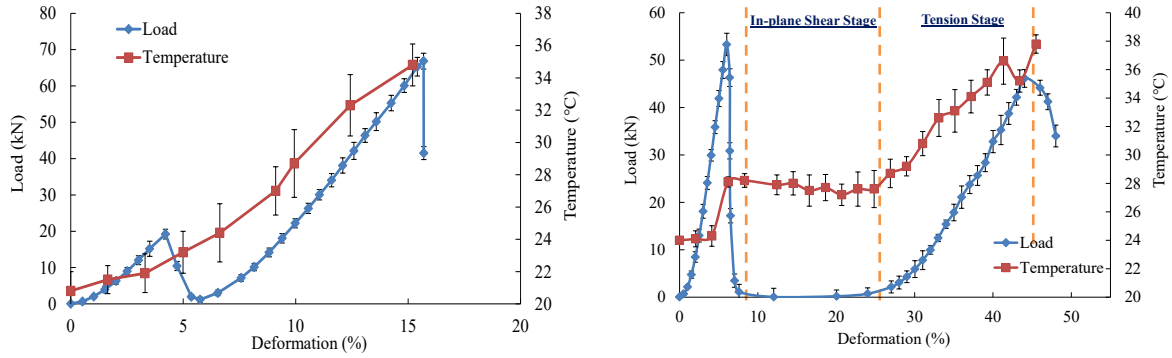

(a) (b)

Fig. 2.22. Temperature and load evolutions during test for (a) sample 6-1-29 and (b) 6-3-48

For the braid 6-3-48(Fig. 2.22b), however, the temperature increases rapidly until reaching the first peak due to the number of axial yarns which is higher in this case. However, the longtime associated with the rotation of the bias yarns causes a decrease in temperature (10-25% deformation). It is possible because the friction caused by yarns rotation is too small to increase the temperature. As soon as bias yarns become contact inducing a significant increase in the load evolution, the temperature follows this increasing trend until the yarns are broken since the friction is a dominant factor to cause heat and meanwhile, enough space to dissipate heat is scarce. Therefore, it is concluded that the fibre number of yarns during the tensile stage has a great effect on increasing temperature because the friction between yarns under load increases as increasing fibre number of yarns. In addition, during the shear stage, the yarns rotation almost does not influence the temperature.

Fig. 2.23 further explains the conclusion above from the point of evolution of braiding angle. It is clearly seen that the evolution of braiding angles and temperature have a definitely inverse trend. For 6-1-29, the evolution of braiding angle decreases slowly as deformation exceeds 10%, and then this trend becomes gentle until the final value is reached. At this stage, the temperature increases more rapidly than it before 10% deformation. Thus, it is suggested that temperature caused by friction rises quickly when bias yarns become contact that the “lock angle” is reached. Comparatively, in the 6-3-48, the evolution of braiding angle decreases greatly among 10%-30% deformation, which is the stage as bias yarns bear the shear deformation. The temperature decreases slightly rather than increases clearly so that friction by shear deformation of bias yarns is not enough to increase the temperature during the test, This is attributed to efficient dissipation that enough time and space during the evolution of braiding angle. Hence, the friction caused by yarns under the tensile stage strongly influences the temperature while the friction caused by bias yarns rotation under

shear behaviour has little effect on temperature, especially for preforms with large braiding angle.

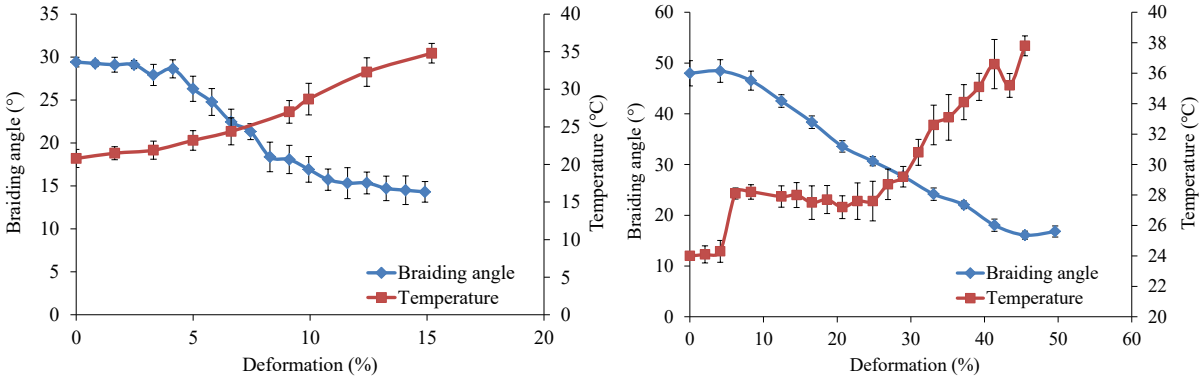

(a) (b)

Fig. 2.23. Evolutions of temperature and braiding angle during tests for (a) sample 6-1-29 and (b) 6-3-48

2.4 Conclusion of Chapter II

As the fundamentally dominated mechanism for deformability behaviours during preforming process for manufacturing composites with complex shapes, the mechanical properties for braided reinforcements are investigated with respect to the in-plane and tensile characteristics influenced by basic braiding parameters. Firstly, the geometric criterion and a general analytical model are developed based on the bias-extension test, and the corresponding availability is verified via comparing experimental results produced by preforms fabricated by natural and synthetic fibres. It is concluded that bias-extension test can be used to figure out the mechanical properties of braided reinforcements based on the proposed geometrical criterion. Secondly, the braiding parameters including braiding angle and number of fibre for axial yarns are discussed in terms of tensile properties, in-plane shearing characteristics and thermal behaviours during tensile tests for triaxial braided preforms. It is suggested that braiding angle could heavily impact the mechanical properties of reinforcements. For instance, increasing braiding angle, deformation ability is improved and temperature produced by friction decreases. Meanwhile, the axial yarns and bias yarns are both subjected to the load until the axial yarns are broken, especially for small braiding angle. Therefore, the braiding angle, the most important difference between braided and woven preforms, can greatly impact the mechanical properties of braided fabrics, determining the deformability behaviours during preforming process. It will be discussed in Chapter III.

III. AN EXPLORATION ON BRAIDED REINFORCEMENTS PREFORMING PROCESS

3.1 Introduction

The preforming process as the essential stage during LCM technique is crucial to the final performance of composites with complex shapes. The deformability behaviours of triaxial braided reinforcements, indeed dominated by mechanical properties discussed on Chapter II, result in undesired drawbacks that greatly influence the quality of resin impregnation stage, for instance, buckling, excessive yarn sliding and wrinkling, which leads to the resin inhomogeneity or poor permeability of resin impregnation through the thickness direction, finally reducing performance of composite parts being in service. Hence, in this part, the deformability behaviours of braided reinforcements during preforming progress were systematically explored, especially for triaxial braided ones. At first, the comprehensive deformability behaviours and possibly introduced drawbacks were discussed. Besides, the mechanical models for yarns during preforming were explored for the purpose of deeply understanding the mechanism behind deformability behaviours. Furthermore, the variation of deformability behaviours dominated by the different braiding angles in terms of magnitude, location on the preforms and profiles were investigated based on the correlation between preform characters and parameters of preforming process. Moreover, the corresponding geometrical model for special deformability behaviours, yarn sliding, was proposed and verified by experimental results.

3.2 Tested materials and experimental set-up

3.2.1 Tested fabrics

The triaxial fabrics were produced by continuous carbon yarns under overbraiding process in GEMTEX laboratory. The braiding angle can be imposed during overbraiding process thanks to selecting the appropriate process parameters. After the braiding process, the braided fabrics were carefully cut and opened to obtain two-dimensional fabric avoiding modification of the braiding angle (Fig. 3.1a). In the fabric scale (macroscopic scale), the axial and transversal directions of fabric were clearly marked. In the single yarn scale (mesoscopic scale), the two directions, longitudinal and radial yarn directions, which are along and perpendicular to the central line of single yarn respectively, are also described in Fig. 3.1(b). These two directions are important to further analyse the sliding behaviour. As shown in Fig. 3.1(c), the triaxial preform was flattened and characterized by axial yarns along the axial direction of fabric interlaced with bias yarns. The characteristics of the tested braided fabric are presented in

Table 3.1. In order to directly present special preforming behaviours of triaxial braids, the woven fabric was put forward as a contrast. Table 3.2 shows the characteristics of the woven fabric.

To master the varied mechanism of deformability behaviours dominated by braiding angle, the braiding angles were selected by $\beta_0/2$, $\beta_1/2$ and $\beta_2/2$ representing the 30°, 55° and 65°, respectively. Selecting braiding angle was based on the fact that the braiding angle can be randomly determined in the range of 5° to 85°.

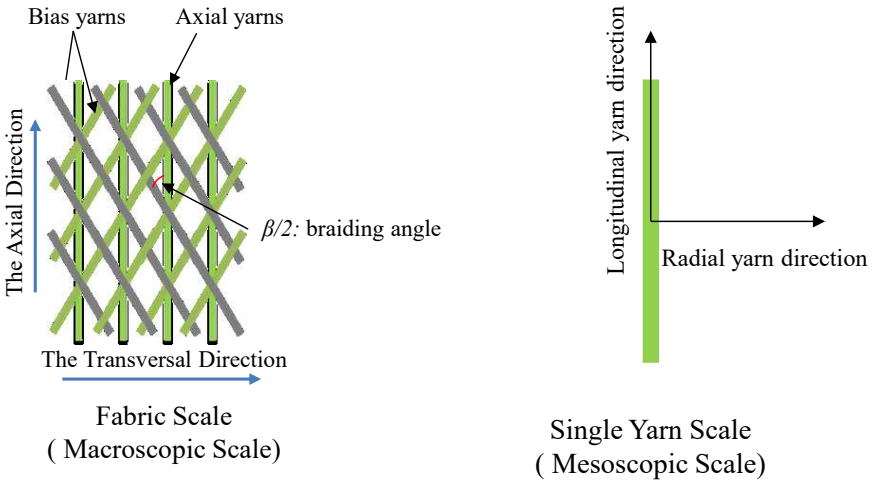

(a) (b)

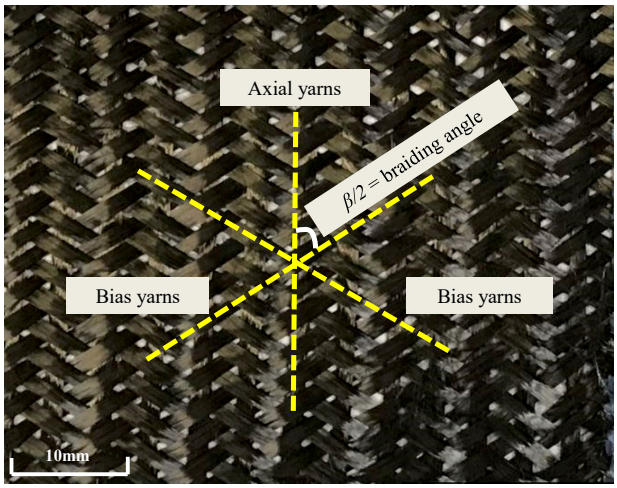

(c)

Fig. 3.1. Tested triaxial braided preforms, (a) the structure, (b) a single yarn profile and (c) a locally specific profile of preform

Table 3.1. The main properties of the tested braided fabric

Parameters	Value
Yarns	792 tex
Area density (g/m2)	510 ± 5
Thickness (mm)	2.37

Braiding angle (°)	30/55/65
Number of yarns per cm	3.9
Surface dimensions (mm2)	280×280
Yarn width (mm)	4.0
Distance between two adjacent axial yarns-L_0 (mm)(centre to centre)	7.5±0.5
Distance between two adjacent bias yarns-L'_0 (mm)(centre to centre)	4.0±0.2

Table 3.2. The main characteristics of the tested woven fabric

Parameters	**Value**
Type of fabric	Twill 2-2
Area density (g/m^2)	600 ± 5
Thickness (mm)	0.62
Number of warps per cm	3.7
Number of wefts per cm	3.7
Surface dimensions (mm^2)	280×280

3.2.2 Preforming machine and experimental set-up

The specific preforming device developed at the GEMTEX laboratory was used as the experimental machine in Fig. 3.2(a). The tested fabric can be put between the upper plate and die since the upper plate is moveable. The upper plate and die are made by Plexiglas and have circular holes with 160 mm diameter in their centre. The corner at the base of the hole in the upper plate is generated to guarantee the preforming successfully. The blank-holder driven by a pneumatic jack permits the pressure on the upper plate during the preforming. The hemispherical punch tool with 150 mm diameter was given a constant movement (45 mm/min) by the lower pneumatic jack equipped with a sensor that could measure the punch force in real-time.

The experiments were divided into two parts, the first part focuses on describing the overall deformability behaviours and corresponding drawbacks. Thus, the varied parameter is only blank-holder pressure that can be selected at 0.05, 0.1, 0.2 and 0.3 MPa, but the braiding angle was fixed at 55°. The second part focuses on the varying braiding angles at fixed 0.1MPa, exploring the law that braiding angle influences the deformability behaviours. Every value was performed by three fabrics in order to verify the repeatability of results

In order to conveniently analyse the preforming behaviours, in particular, the yarns sliding, the axial and bias yarns should be numbered before preforming. The axial yarns from the centre of fabric along the transversal direction were numbered as shown in Fig. 3.2(b). Since the number of axial yarns within the hemisphere shape after preforming was approximately twelve, the number thus in Fig. 3.2(b) was from 0 to 11. Due to symmetrical profiles of hemispherical punch shape and square fabric, the axial yarn that coincides with the central

line of punch shape, was considered as N°0 and the L_0 (in Table 3.1) was defined and measured as the initial distance between axial yarns before preforming. By the same definition method, the bias yarns can also be numbered (see Fig. 3.2b) and L'_0 was also defined and measured before.

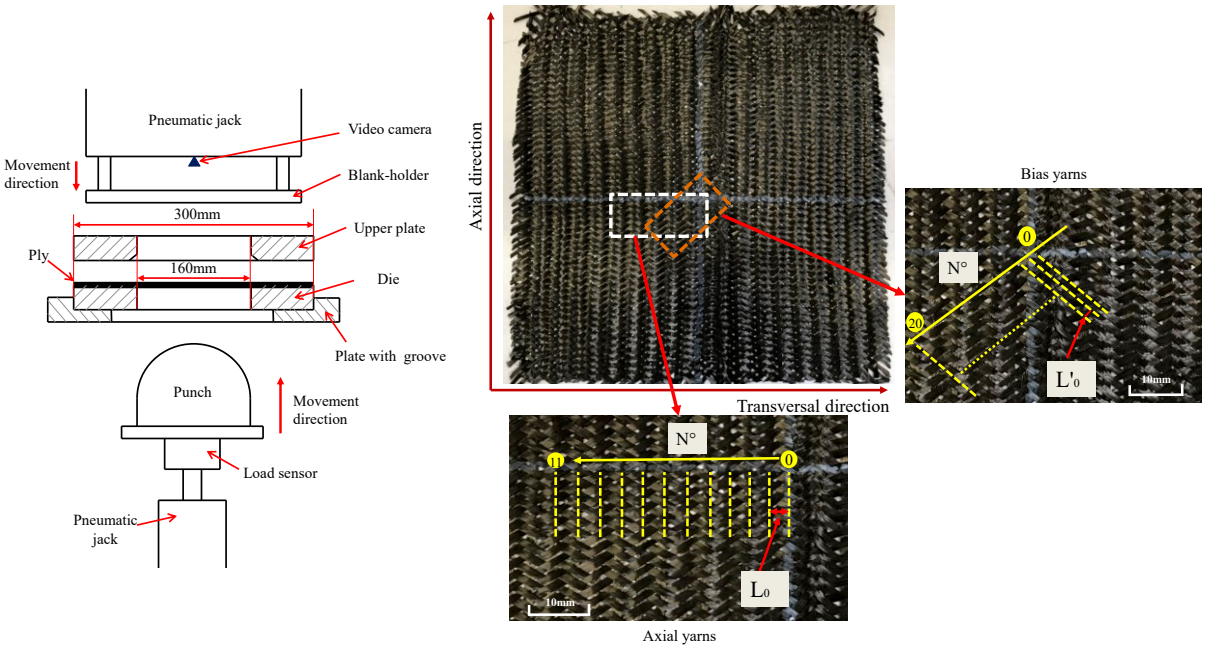

(a) (b)

Fig. 3.2. The details of (a) preforming machine and (b) numbered yarns

After preforming but before blank-holder moving back ("demoulding"), the deformed preform in the preforming device can be fixed using the certain settling agent in order to avoid the elastic spring-back. A video camera installed on the device and linked with a computer is used to monitor preforming process and measure the evolution of yarn sliding. After the consolidation of the settling agent, the blank-holder moved back to the original position and the deformed preform was moved outside from the device for further measurement.

3.3 Deformability behaviours-general results and discussion

The triaxial braided fabric with braiding angle 55° after the preforming with a blank-holder pressure of 0.1MPa can be observed in Fig. 3.3(a). The yarns sliding and in-plane shear zones can be clearly seen as symmetrical profiles. In contrast, preforming of the woven fabric produced by the same carbon yarns with braided fabric is showed in Fig. 3.3(b), which shows a global displacement (material draw-in) clearly in two directions. Moreover, compared to the deformed woven fabric, only two in-plane shear zones can be observed in the transversal

direction in triaxial braided fabric due to the unbalanced structure. Being different from the hemispherical preforming of the woven fabrics, this unbalanced distribution of in-plane shear was also observed in the preforming of the biaxial braided fabrics. The unbalanced structure of tested triaxial fabric exhibits two different characteristics under tension along with axial and transversal directions of fabric, as discussed in Chapter II. The following sections will discuss specific deformability behaviours of triaxial braided fabric, as well as the corresponding defects that could impact the quality of composites parts.

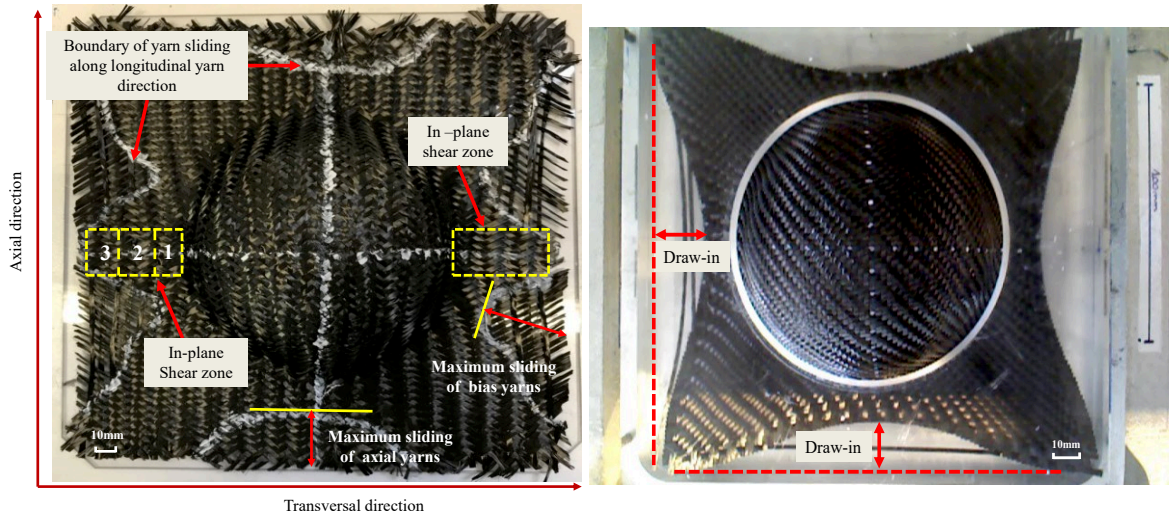

(a) (b)

Fig. 3.3. The fabrics after preforming, (a) triaxial fabric and (b) woven fabric

3.3.1 Yarns sliding

1. The sliding along longitudinal yarn direction

The yarns sliding can be naturally divided along with longitudinal and radial yarn directions at the mesoscopic scale (see Fig. 3.1b). The yarns sliding along with longitudinal yarn direction is induced by the out-plane bending in the punch zone. However, axial and bias yarns show different situations. The analysis of yarn sliding is based on the quasi-inextensibility since the carbon yarns almost have no extension.

<u>The axial yarns sliding</u>

In Fig. 3.3, it is clearly seen that axial yarns sliding along longitudinal yarn direction can be approximately profiled as half ellipse marked by white lines at the axial direction of the fabric. The central axial yarn (N°0 defined in Fig. 3.2b) has maximum sliding because it is imposed on the maximum out-plane bending displacement. Since axial yarns are symmetrical to the transversal direction of the fabric, i.e. the central line of punch tool, the axial yarn sliding along longitudinal yarn direction at the ends is almost identical. Fig. 3.4 shows the maximum

punch force and the maximum axial yarn sliding along longitudinal yarn direction during the preforming with different blank-holder pressures. It can be observed at first that the augments of the blank-holder pressure lead to an increase of the punch force as expected. Remarkably, the maximum sliding nearly does not increase with blank-holder pressures. According to [212], the friction of tow-on-tow and tow-on-tool is too small to restrict the axial yarns slippage even though at maximum pressure. Thus, the sliding is dependent on the yarn length under blank-holder. At the same punch shape, the maximum sliding is almost identical.

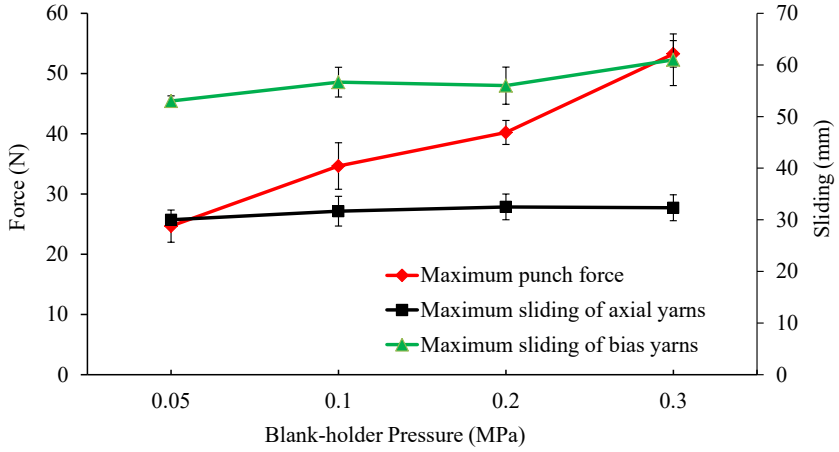

Fig. 3.4. Maximum sliding along longitudinal yarn direction in function of different blank-holder pressures

The bias yarns sliding

Bias yarns along longitudinal yarn direction can be profiled in Fig. 3.5(a). Such sliding presents the difference compared to axial yarn sliding in the same direction. In Fig. 3.5(a), except for bias yarn across the centre of punch shape (N°0 bias yarn in Fig. 3.1), the other bias yarns show the uneven sliding at the ends of yarn. One end with a relatively shorter distance to the base of punch shape could slide with a larger extent due to the unequal friction induced by the ends of yarn. Fig. 3.5(b) clearly shows the behaviour of this bias yarn sliding. Thus, the maximum sliding can be produced by only one end of yarn sliding, another end does not move at all (bias yarns with yellow colour in Fig. 3.5a). Some bias yarns around the base of punch shape almost do not slide due to insufficient out-plane bending that cannot result in sliding. In addition, increasing blank-holder pressure almost has no effect on maximum bias yarns sliding along longitudinal yarn direction as shown in Fig. 3.4.

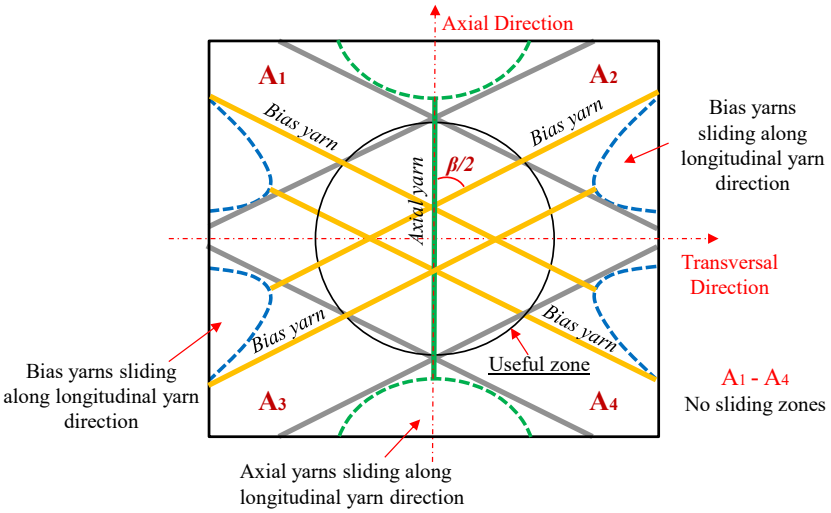

(a)

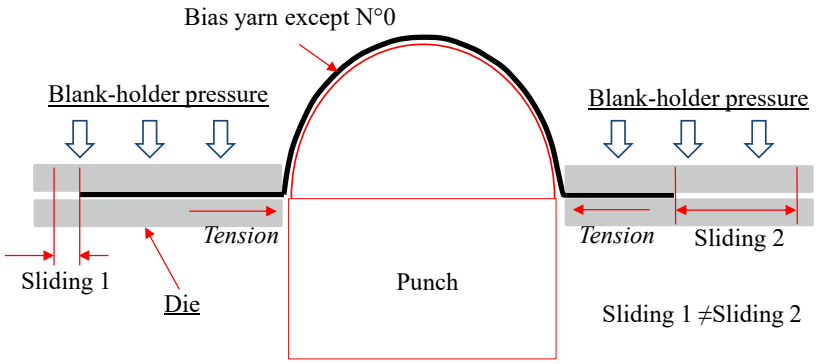

(b)

Fig. 3.5. The yarn sliding along longitudinal yarn direction, (a) the overall profile of sliding performance and (b) the non-identical sliding of bias yarns

2. The sliding along radial yarn direction

The yarns in the useful zone not only sustain tension along longitudinal yarn direction but also bear shear force along radial yarn direction, which originally generates another type of yarn sliding, the sliding along radial yarn direction.

The axial yarns sliding

Axial yarns numbered before preforming as shown in Fig. 3.1 can be counted from top to bottom of hemisphere shape after preforming. As shown in Fig. 3.6, the L_i represents the vertical distance between the N° i-1 and N° i axial yarns along the central line of hemisphere shape (i is the N° of marked axial yarn). This distance, which subtracts the initial distance between two adjacent axial yarns before preforming (L_0), could characterise the sliding of axial yarns along radial yarn direction. To calculate L_i, the vertical distance (d_i) of each sliding axial yarn to N°0 axial yarn could be firstly measured from the top view by an optical

method. And then, the locations of axial yarns in the useful zone can be obtained geometrically on the 2D vertical plane (the plane passing through the central line) projected from the 3D useful zone (Fig. 3.6b). Consequently, the sliding angle θ_i defined in Fig. 3.6(b) can be calculated. Then, the chord length between two adjacent axial yarns equal to L_i can be calculated. Besides, L_i is smaller at the base of the hemisphere as seen in Fig. 3.6(a) because the portion of yarn is gradually restrained by blank-holder when it is close to the base of punch shape. Hence, axial yarns sliding along radial yarn direction is different along shape curve, and the maximum sliding distance is characterised along the central line of shape, which is used to evaluate the sliding along radial yarn direction.

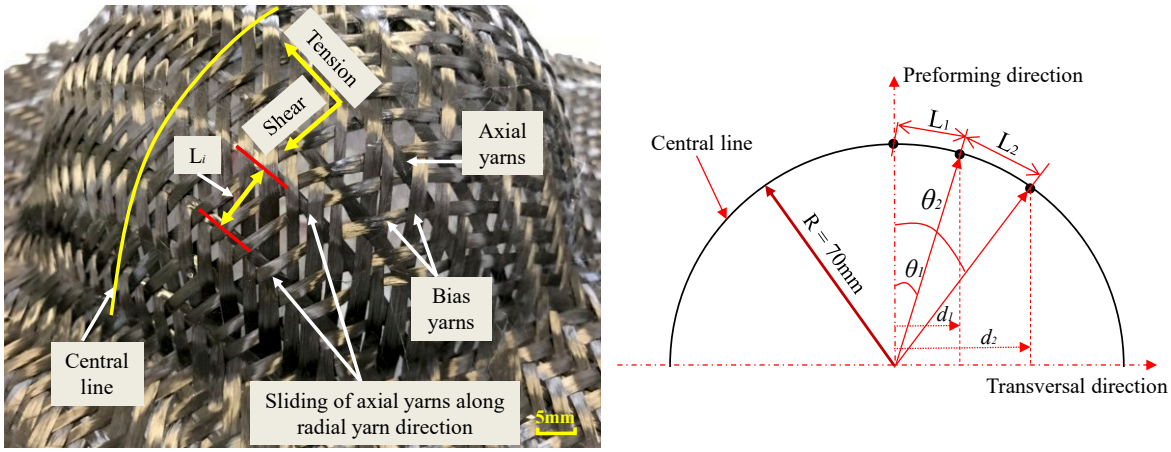

(a) (b)

Fig. 3.6. Sliding of axial yarns along radial yarn direction, (a) the sliding phenomenon in the useful zone and (b) the depiction of sliding

The axial yarns sliding along radial yarn direction with different pressures can be seen in Fig. 3.7. Generally, the variation of axial yarns sliding along radial yarn direction shows a similar trend under different pressures. This trend can be divided into three parts. At first, regarding the four axial yarns around the top of the hemisphere (1st - 4th yarn), their sliding along radial yarn direction increases slightly (the maximum is about 2mm). In contrast, this sliding increases sharply in the second part (5 - 8th yarn located around half hemisphere shape). The maximum sliding can approximately reach 2.5 mm with 0.05 MPa and 8 mm with 0.2 MPa. Besides, the maximum sliding increases a little as pressures above 0.1MPa. After reaching the maximum sliding, the curves decline rapidly at the last three yarns (9-11th yarn), which locates near the base of hemisphere shape. Thus, the sliding of axial yarns along radial yarn direction is associated with the distance between the other yarns to the N°0 yarn within the useful zone. This is because of non-uniform shear effects along the hemispherical surface during the preforming. However, 0.05 MPa shows the smallest component force in radial yarn

direction, this sliding thus presents a low level. As a result, this non-uniform sliding generates the non-homogenous gaps between the axial yarns in the useful zone, resulting in nonhomogeneous density after resin impregnation stage in LCM process.

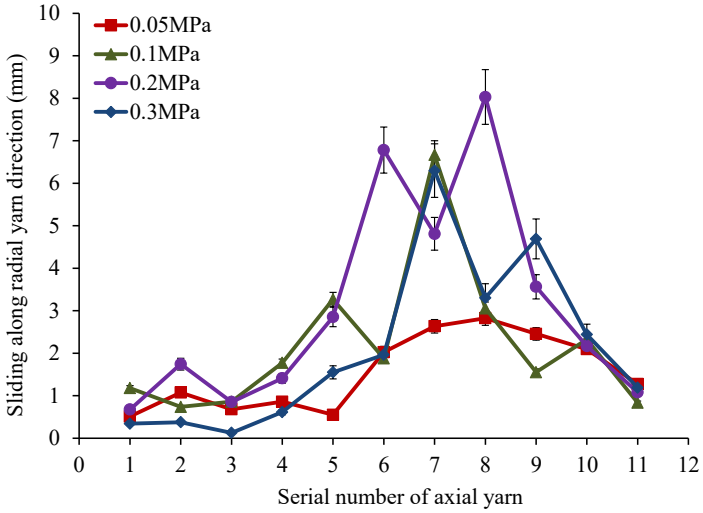

Fig. 3.7. Axial yarns sliding along radial yarn direction with different blank-holder pressures in the useful zone

The bias yarns sliding

The sliding of bias yarns along radial yarn direction also can be observed in the useful zone as shown in Fig. 3.8(a). The way to calculate this sliding is same as axial yarns as the discussion above. The initial distance of bias yarns before preforming is L'_0 shown in Table 3.1. The initial positions of the twenty bias yarns before preforming are shown in Fig. 3.1. Fig. 3.8(b) describes the sliding of bias yarns along radial yarn direction in the useful zone with different pressures. The tendency of the four curves is much similar. It is clearly observed that the sliding has a small increase in the first part (1st-5th yarn), a big increase between 6 -17th yarn and a rapid decrease in the last part. It also can be remarked that the sliding generated by 0.05 MPa is different from other pressures. The sliding increases slowly and the maximum sliding remains quasi-constant during the second part of the curve (increase 0.5-1.0 mm). The maximum sliding increases slightly when the blank-holder pressure is superior to 0.1 MPa. Therefore, it can confirm that the distance between other yarns to N°0 yarn, i.e. the centre of hemisphere shape, is the key factor to influence the sliding along radial yarn direction when pressure over a certain value.

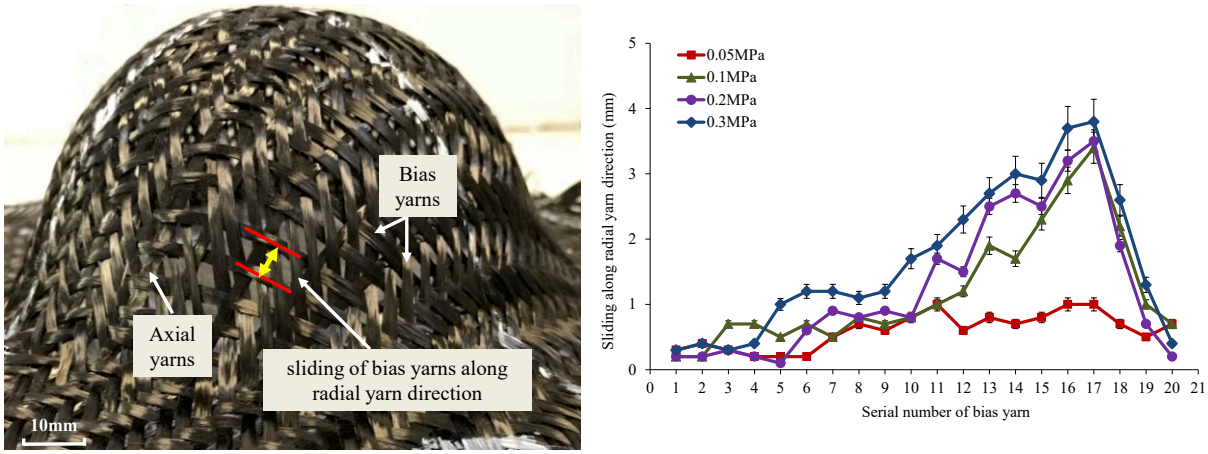

(a) (b)

Fig. 3.8. The bias yarns sliding, (a) sliding and (b) its extend for each bias yarn

3.3.2 In-plane shearing

As mentioned previously (see Fig. 3.3a), two in-plane shear zones can be observed on the deformed preform. The ImageJ software can be used to measure the shearing angle after moving deformed fabrics from preforming device. As expected, the shearing action decreases gradually from the base of the punch shape to fabric boundary. Consequently, the measurements of the in-plane shear angle were performed at different three zones as shown in Fig. 3.3(a). The first one is nearby the base of punch shape, the second one is in the middle of the shearing zone and the last one is closer to fabric boundary. These in-plane shear zones show the negative in-plane shear angles according to the classical definition of the in-plane shear angle γ shown in Eq. 3-1. As demonstrated in Fig. 3.9, the negative in-plane shear angle is generated by the bias yarns turning outward during the deformation of the braided fabric.

The (3-1)

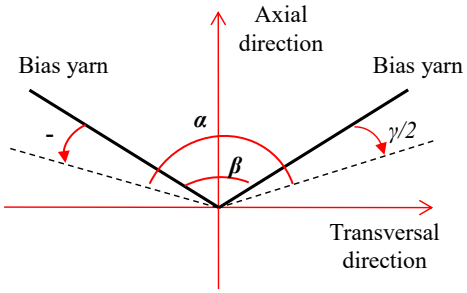

Fig. 3.9. The in-plane shearing towards to the transversal direction

The maximum punch force and the mean in-plane shear angle *vs.* the blank-holder pressure are shown in Fig. 3.10. It is shown that the decrease in shear angle with increasing blank-holder pressure, meaning that the blank-holder pressure that generates the friction almost has

no effect in sliding along the longitudinal direction of yarn, but could effectively influence the in-plane shearing degree of bias yarns under the upper plate. Increasing blank-holder pressure leads to an augment in friction that heavily impacts the in-plane shearing. Hence, the in-plane shearing angle decreases as increasing blank-holder pressure. What results in in-plane shearing angle shows the negative value is associated with braiding angle, which would be detailed in the next section.

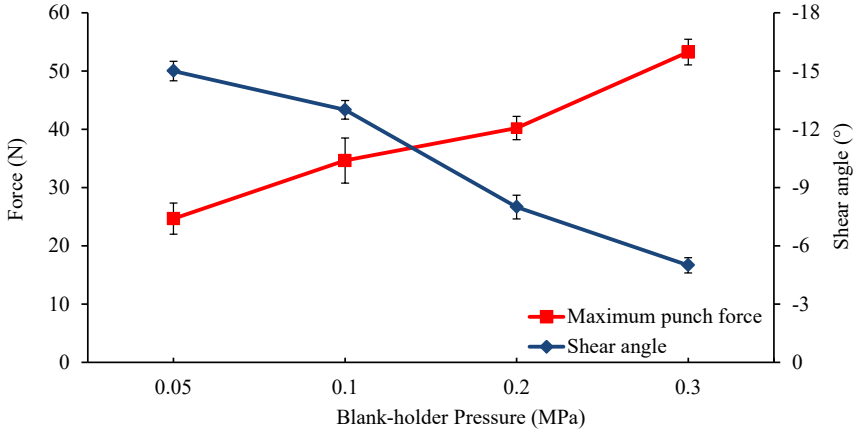

Fig. 3.10 The maximum punch force and the mean in-plane shear angle *vs.* the blank-holder pressure

3.3.3 Preforming drawbacks

Based on the analysis above, it is possible to perform double curvature shapes with triaxial fabrics. However, the preforming drawbacks were also observed and heavily related to basic input parameters. In general, the blank-holder system, which offers a sufficient tension level during the preforming, is important since it could effectively prevent the appearance of the wrinkling defect. By applying a sufficient tension on preform, the compression effect can be annealed. Nevertheless, the special defect, fibre vacancies, could be produced after preforming if the parameters are not properly selected. The other normal drawbacks, which can be observed after preforming woven preforms such as gaps and buckling, are also clearly noticed.

1. Fibre vacancies

As described above, the yarns sliding along longitudinal yarn direction cannot be prevented. Although this phenomenon at the useless zone is not necessary to consider, if this sliding steps into the useful zone, the sliding exceeds the residual distance depicted in Fig. 3.11, the fibre vacancies would be generated locally. Thus, the nonhomogeneous permeability would happen and reduce the mechanical performance of final composite parts. The residual distance is defined as the distance between maximum sliding to the base of the punch shape. The

extent of yarns sliding along longitudinal yarn direction can be determined by the parameters such as the diameter of the punch, the preform dimensions and the braided angle. Hence, the correlation among these parameters should be carefully considered by the composite part designer in order to avoid the excessive yarns sliding along longitudinal yarn direction. The simple geometrical model to predict such defect is expressed in the following.

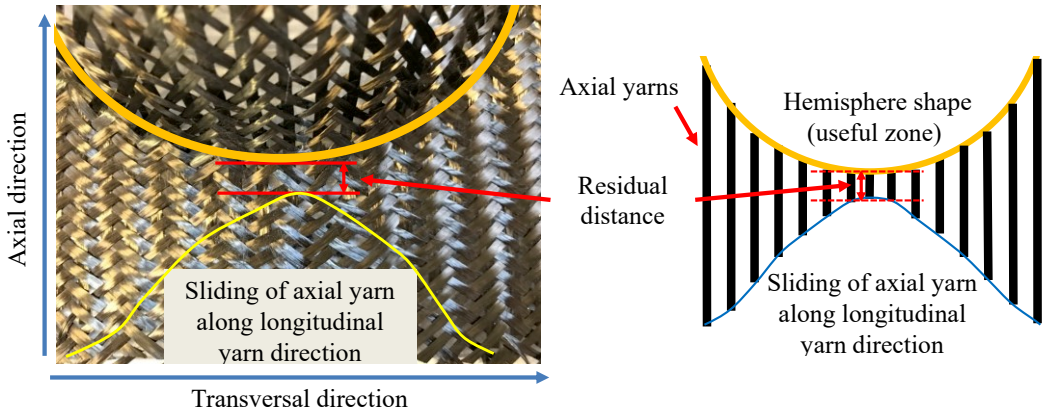

Fig. 3.11. The large extent of yarns sliding along longitudinal yarn direction

2. Gaps and buckling

The yarn sliding along radial yarn direction could lead to irregular gaps (seen in Fig. 3.12), negatively impacting the uniformity of fibre density. It can be inferred from Fig. 3.8(b) that less sliding at 0.05MPa could reduce the magnitude of the gaps. Furthermore, the buckling of bias yarns shown in Fig. 3.12 is also detected. As discussion above, the increasing blank-holder pressure can increase the bias yarns sliding along radial yarn direction towards the base of punch shape, so that the smaller circles, leading to the out-of-plane defect as buckling, are possibly produced. Due to the braiding method for such fabric, the axial yarns have more degrees of freedom along longitudinal yarn direction than radial yarn direction. Consequently, no buckling is observed at axial yarns in the useful zone.

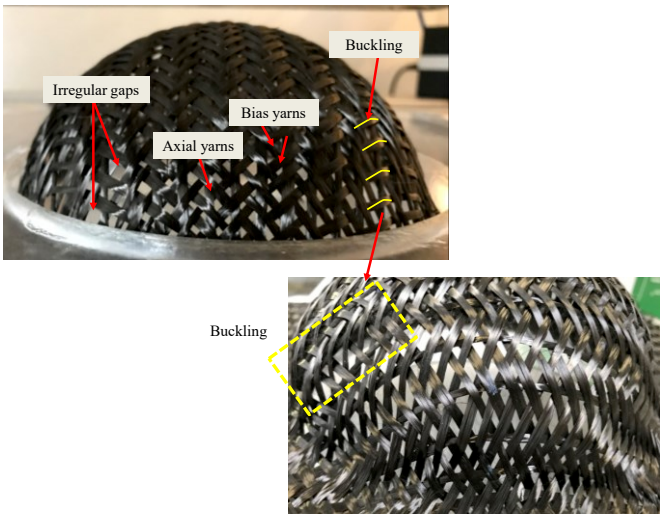

Fig. 3.12. The gaps and buckling in the useful zone

3.3.4 Variation of deformability behaviours influenced by braiding angle

In the second part of experiments, the braiding angles were changed in order to explore the variation of deformability behaviours, and based on experimental results, they exhibit discriminated forms with varied braiding angles. Fig. 3.13 shows the preformed profile of fabric with small braiding angle 30°. It is visible that material draw-in, in-plane shearing and yarn sliding zones are almost symmetrical with transversal directions of the fabric. The corresponding shearing angle γ shows positive value according to the classical definition as described in Section 3.3.2. The yarn sliding zones profiled by white lines are characterized by bias yarns and axial yarns. The sliding of bias yarns is also observed by uneven sliding at the ends of yarn. By contrast, the axial yarns show the identical sliding at the ends. Notably, interlaced bias yarns presenting the in-plane shearing are only around the centre line of preformed shape along the axial direction of fabric outside the punch zone, in which the material draw-in also takes place. However, the other bias yarns only present the uneven yarn sliding.

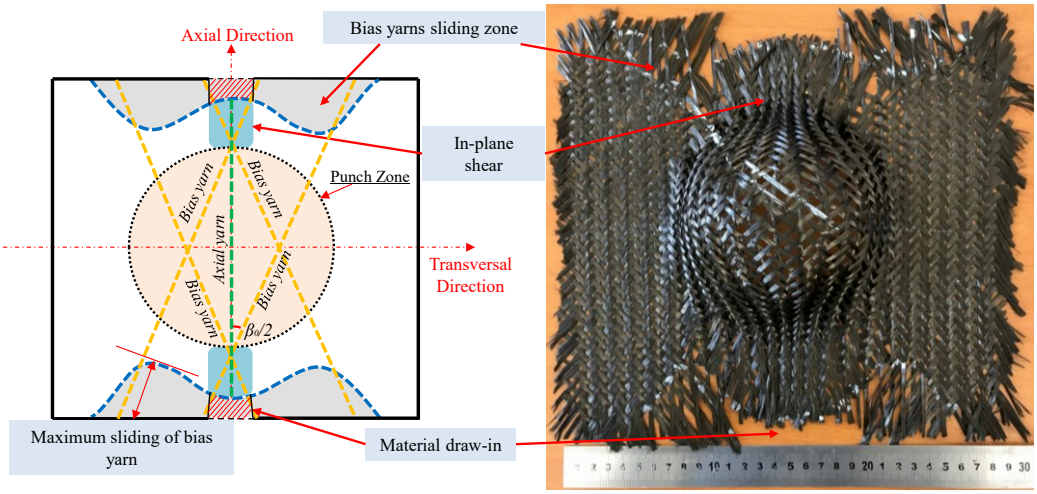

Fig. 3.13. The experimental result by braided angle 30°

Further increasing the braiding angle to 65° as shown in Fig. 3.14, the material draw-in with a small degree appears, and its location is the same as in-plane shearing zones in braiding angle 55°. Besides, the corresponding shearing angle γ also shows the negative value. The identical axial yarns sliding zones symmetrical with the transversal direction of fabric are also detected. The bias yarns sliding zones locate the same position as braiding angle 55°, but the extent of uneven sliding becomes smaller than that in braiding angle 30° and 55°.

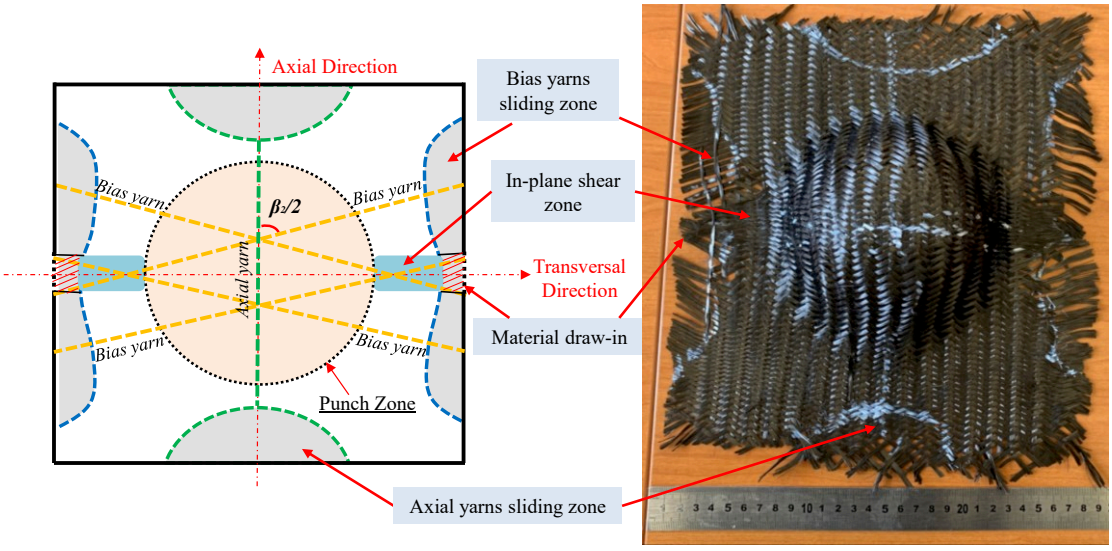

Fig. 3.14. The experimental result by braiding angle 65°

Consequently, according to the experimental results, it is induced that changing the braiding angle can actually influence the appearances of different kinds of behaviours during preforming in fabric mesoscale including the magnitude, location, and orientation. Besides, the material draw-in, which can be defined as whole yarns absence in the local fabric after preforming, can be explained by the co-effect of in-plane shearing and yarns sliding that the former takes place at first, then the latter occurs.

3.4 The mechanical model for yarns and geometrical model for yarns sliding

The deformability behaviours have been detailed qualitatively as discussion above. However, the mechanical character of a yarn that crucially influences such behaviours should be cleared. Hence, the tension model for a yarn would be explored and discussed in order to further understand the deformability behaviours of triaxial braided preforms during preforming.

3.4.1 The mechanical model for yarns

1. N°i axial yarn

The N°i axial yarn, which is symmetrical about transversal direction of fabric (Y-direction), is put forward to express such mechanical model during preforming as shown in Fig. 3.15(a). O is the central point of punch tool and fabric. R is the radius of punch tool, in theory, it is also the radius of punch zone. If the traction force along punch tool surface during preforming is ignored, the vertical distance between O point and N°i axial yarn would be fixed and calculated as iL_0 before and after preforming, L_0 is shown in Tab. 3.1. Furthermore, N°i axial yarn can be projected into half Z-Y plane as shown in Fig. 3.15(b), O' is the corresponding centre point of half circle deformed by N°i axial yarn during preforming. Thus, N°i axial yarn deformed during preforming can be naturally divided into two portions. The first portion continually deforms owing to out-plane bending force so that punch zone is produced, making a displacement in Z direction. The yarn segment AE in Fig. 3.15(b) could character this portion. The point A stands for the vertex of punch tool surface, point M represents the yarn beginning to contact the punch tool surface. The θ_i^A expresses the angle of the yarn/punch contact area from point A to M during preforming process. The portion of yarn QE portrays the contact area of the yarn and corner of upper plate. During the preforming process, indeed, the first portion AE does not contact the entire punch tool surface, as seen the yarn segment MQ without contacting any surface of punch tool. The second portion of yarn is the segment yarn ET which is located between upper plate and die, subjecting the blank-holder pressure. Due to the first portion of yarn AE driven by out-plane bending, the tension is generated along the longitudinal yarn direction. When it overcomes the static friction, which is resulted by upper plate and die and proportional to the length of second portion of yarn ET, the sliding is thereby produced at the ends of yarn as shown in Fig. 3.15(a) and (b), one end slides gradually from the point T to F.

During the preforming, the length of segmental yarn AM increases at the onset of preforming process. Accordingly, θ_i^A increases from zero to the maximum value when the preforming process is over as shown in Fig. 3.15(b). In contrast, the length of segment yarn MQ decreases. It is clearly acquired that θ_i^A is proportional to the displacement in the Z direction, at the end of preforming process, maximum value of θ_i^A is also obtained.

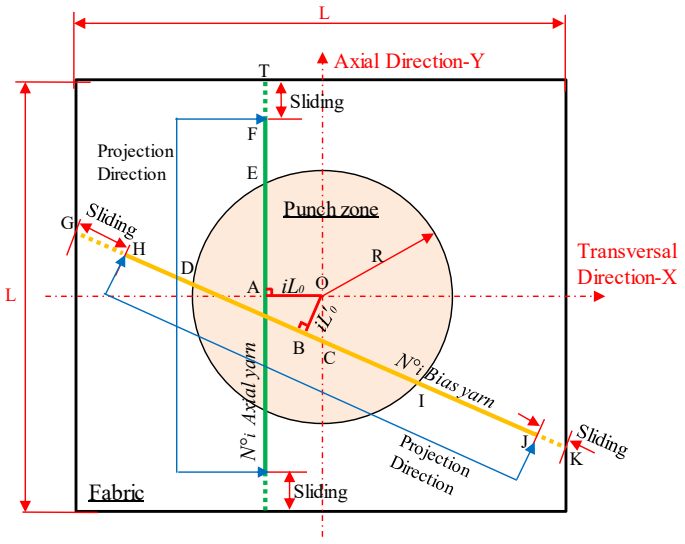

(a)

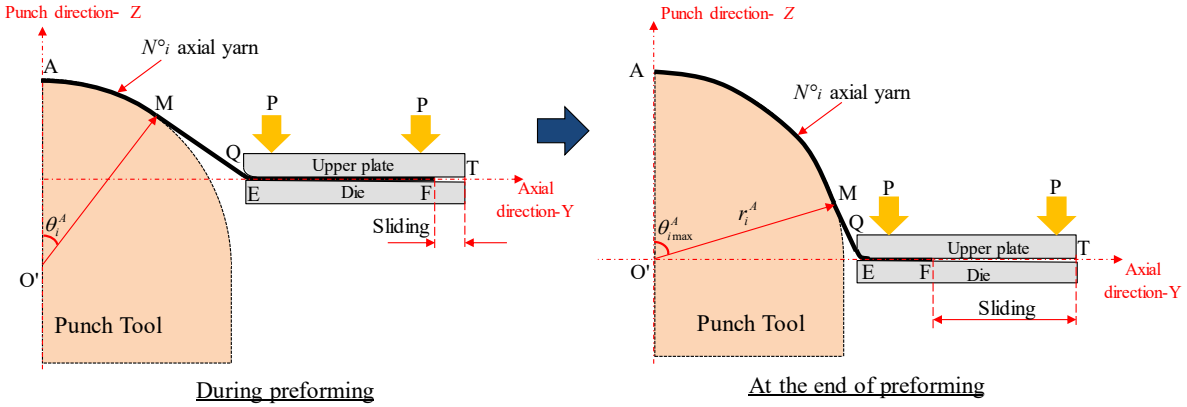

(b)

Fig. 3.15. Sliding occurring during preforming. (a) Geometrical position of N°*i* axial yarn relative to punch tool, (b) N°*i* axial yarn formed by punch tool

Therefore, the mechanical model during preforming can be set up as shown in Fig. 3.16. According to Coulomb Friction Model, the maximum tension is the reaction force of static friction as yarn sliding occurs instantly. The point Q is virtually cut to conveniently analyse the mechanical model of tension. The equilibriums can be expressed during the preforming process:

$$\begin{cases} T_e = f_i^A \\ T_m = T_q = T_e e^{\mu_2 \theta_i^A} \\ T_a = T_m e^{\mu_3 \theta_i^A} \end{cases} \tag{3-2}$$

Where the T_a, T_m, T_q and T_e present the tension at points A, M, Q and E respectively, and f_i^A is friction of N°i axial yarn generated by upper plate and die at one end. μ_2 and μ_3 symbolize the friction coefficient between yarn/upper plate and yarn/punch tool, respectively.

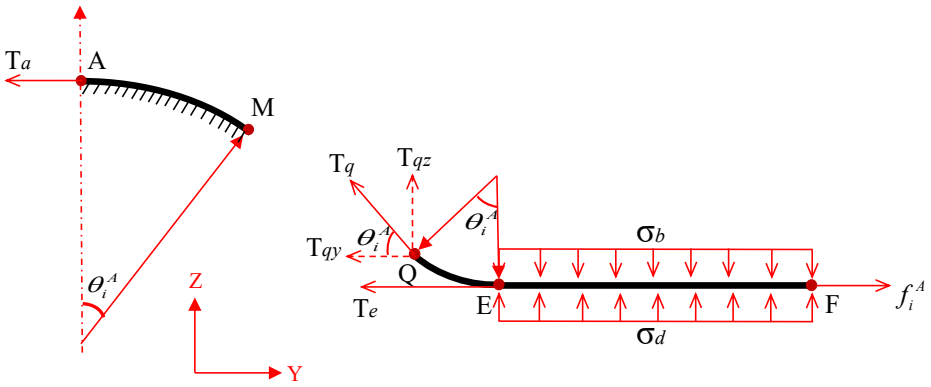

Fig. 3.16 The schematic diagram describes the tension generated during the preforming

According to triaxial fabric structure, the crossovers, the interacting zones made by axial and bias yarns between the upper plate and die as shown in Fig. 3.17(a), mainly sustain the pressure provided by machine in theory. Hence, the friction condition for axial yarn and bias yarn absolutely shows the difference that needs to be investigated respectively. At first, the area of a crossover section A_x in Fig. 3.17(a) can be roughly estimated:

$$A_x = w^2 \sin\beta \tag{3-3}$$

Where w is the width of yarn. Thus, regarding a body diagram for a segment of crossover shown in Fig. 3.17(b), the equilibriums for top bias yarn in shade zone can be expressed respectively as:

$$\begin{cases} \sigma_a A_x + 2\tau_b S - \sigma_b A_x = 0 \\ \sigma_b A_x = \dfrac{P\left(A - \pi R^2\right)}{n} - \dfrac{T_{qz}}{n_i^A} \end{cases} \tag{3-4}$$

σ_a and σ_b present the contact stress on axial yarn and top bias yarn, respectively. τ_b is the shear traction that must act along the dashed line in the bias yarn if the yarn were cut there and equilibrium maintained. Both shear and compressive stresses in the bias yarn might contribute to τ_b. S is the area of shear traction and can be calculated by $wd/3$, d is the fabric thickness. P is the blank-holder pressure; A is the fabric area; n is total number of crossovers under the upper plate, which is constant as fixed punch tool and fabric parameters; n_i^A denotes

the number of crossovers at one end of N°i axial yarn. T_{qz} is component force of T_c in Z direction. The friction generated by one crossover can be explained by:

$$f = 2\mu_1\sigma_a A_X \tag{3-5}$$

Where the μ_1 symbolize the friction coefficient between yarns. Thus, f_i^A can be expressed as follow:

$$f_i^A = \int_0^{n_i^A} f dx = 2n_i^A \mu_1 \sigma_a A_X \tag{3-6}$$

If the tension of N°i axial yarn at one end T_i^A can be represented by T_q, it would be deduced according to Eqs. (1-6):

$$T_i^A = T_q = \frac{2n_i^A \mu_1 e^{\mu_2\theta_i^A}\left(\dfrac{p\left(A-\pi R^2\right)}{n} - \dfrac{2}{3}wd\tau_b\right)}{1+2\mu_1 e^{\mu_2\theta_i^A}\sin\theta_i^A} \tag{3-7}$$

Due to symmetry of axial yarns about the transversal direction of fabric, the tension at two ends is identical owing to the equal length of yarn under upper plate. Hence, the sliding at the ends for any axial yarn shows identical but the sliding degree for different axial yarns is unequal. Besides, due to the identical tension at the ends, the balance is acquired. It means that the first portion of yarn AM does not slide along the surface of punch tool.

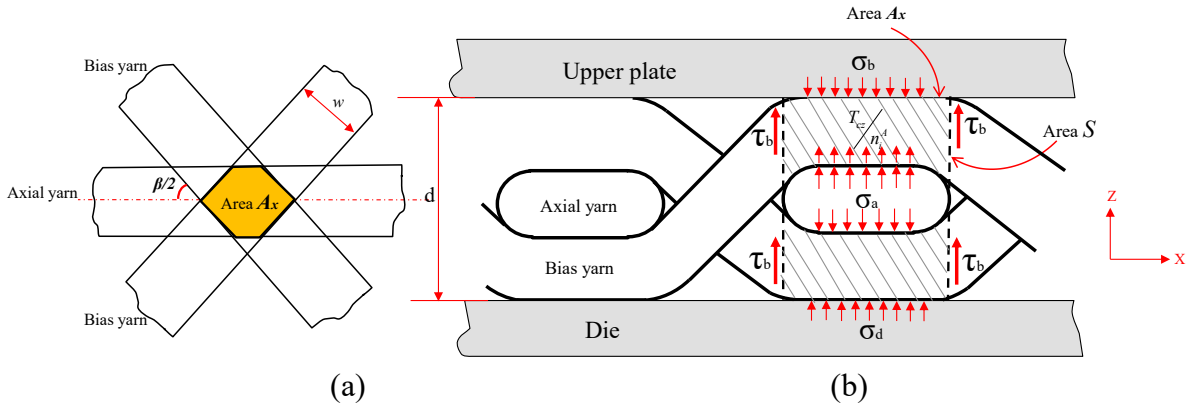

Fig. 3.17. The diagram presents the load transfer through a crossover region between upper plate and die in theory, (a) the area of crossover and (b) free body diagram in a random crossover

2. N°i bias yarn

Exploring the tension of N°i bias yarn (i≠0), T_i^B, is in accordance with T_i^A but it relatively complicated on the account of two aspects, the first one is that the length of the second portion that subjects the pressure between upper and die is not identical with two ends, as shown in Fig. 3.15(a), $l_{GD} \neq l_{IK}$. Thus, the tension at two ends is also not equal, accordingly

generating the difference in sliding. In the same, If the traction force along punch tool surface during preforming is ignored, the vertical distance between O point and N°i bias yarn can be fixed and expressed as iL_0' before and after preforming, L_0' is shown in Tab. 3.1. The point B is the vertex of corresponding half circle deformed by N°i bias yarn as shown in Fig. 3.18. The point C is centre of N°i bias yarn. Indeed, these two points do not coincide resulting in the non-identical sliding at the ends. Moreover, it is deduced that the increasing vertical distance between these two points l_{BC} could aggravate the extent of non-identical sliding at the ends. Therefore, in order to obtain the balance for N°i bias yarn during preforming, the unequal tension at the ends could cause N°i bias yarn to slide on the surface of punch tool. That is different from N°i axial yarn during preforming.

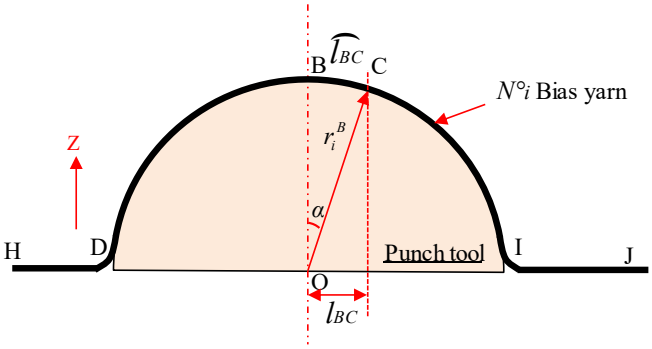

Fig. 3.18. N°i bias yarn after preforming

The second aspect is about the friction. As the braided structure is shown in Fig. 3.17(b), the bias yarn alternately locates at top and bottom in two adjacent crossovers, leading to different friction conditions. Thus, the friction calculation at one end, f_i^B, can be roughly expressed as follows:

$$\begin{cases} f_i^B = \dfrac{n_i^B}{2}\left(f_i^t + f_i^b\right) \\ f_i^t = \mu_2\sigma_b A_x + \mu_1\sigma_a A_x \\ f_i^b = \mu_2\sigma_d A_x + \mu_1\sigma_a A_x \end{cases} \tag{3-8}$$

Where f_i^t and f_i^b stand for the friction forces as N°i bias yarn locates at top and bottom in adjacent crossovers. σ_d is the contact stress on bias yarn at the bottom in shade zone as shown in Fig. 3.17(b). Because the upper plate and die are made by the identical material, the μ_2 is friction coefficient in contact surfaces of yarn/upper plate and yarn/die. n_i^B is the number of crossovers at one end under the upper plate. Being same as Fig. 3.17(b), the equilibriums in Z direction can be denoted as:

$$\begin{cases} \sigma_d A_x + 2\tau_b S - \sigma_a A_x = 0 \\ \sigma_a A_x + 2\tau_b S - \sigma_b A_x = 0 \\ \sigma_b A_x = \dfrac{P\left(A - \pi R^2\right)}{n} - \dfrac{T_{cz}}{n_i^B} \end{cases} \tag{3-9}$$

Referred to deduction of tension for N°i axial yarn, the tension for N°i bias yarn can be expressed as:

$$T_i^B = \frac{n_i^B \left(\mu_1 + \mu_2\right) e^{\mu_2 \theta_i^B} \left(\dfrac{p\left(A - \pi R^2\right)}{n} - \dfrac{2}{3} w d \tau_b \right)}{1 + \left(\mu_1 + \mu_2\right) e^{\mu_2 \theta_i^B} \sin \theta_i^B} \tag{3-10}$$

It is suggested from Eq. (3-7) and (3-10) that tension is heavily associated with the number of crossovers at one end under upper plate and punching displacement. Whether such number or punching displacement, especially for bias yarn, is determined by braiding angle because it geometrically decides the length of portion yarn under upper plate as fixed punch tool. Thus, the deformability behaviours were changed at magnitude and location with a variation of braiding angle as seen in 3.3.4. Furthermore, the sliding, which is directly generated by tension, can be approximately expressed on an approach of geometrical model based on the same assumption as tension models.

3.4.2 The geometrical model for yarns sliding

As the discussion above, the tension generated by the out-plane bending during preforming, when it reaches the static friction generated by die and upper plate, the sliding occurs instantly. Once the sliding occurs, the friction becomes small. Then, the sliding distance is proportional to punching displacement. However, for different axial and bias yarns, the geometrical position relative to punch zone decides the corresponding punching displacement. Furthermore, the extensibility of carbon yarn is little and after preforming, there is no broken carbon being observed. Thus, the carbon yarn could be considered as inextensibility in preforming stage. It is thus reasonable to believe that once out-plane bending starts, the yarns slide instantly according to the performance of experimental results. Therefore, the sliding can be predictably calculated via geometrical analysis before preforming under the condition of neglecting the traction force along the surface of punch tool towards the base of the punch tool during preforming.

1. The axial yarns sliding

The axial yarn is symmetrical with the central line of hemisphere shape along the transversal direction of the preform, resulting in the identical portion yarn length under the upper plate. Thus, the tension at the ends of yarn is equal, and accordingly, the sliding at the ends presents identical value shown in experimental results.

The first portion yarn length of N°i axial yarn projected in X-Y plane $2l_{AE}$, which is seen in Fig. 3.15(a) and named as d_i^A is geometrically equal to the diameter of a perfectly preformed circle by the corresponding N°i axial yarn. It means that the maximum punching displacement is equal to half of d_i^A. The d_i^A can be expressed geometrically as:

$$d_i^A = 2\sqrt{R^2 - (iL_0)^2} \tag{3-11}$$

Based on the inextensibility of carbon yarn before and after preforming, S_i^A that stands for the predicted sliding of N°i axial yarn at one end can be expressed as follows:

$$\text{Before preforming: } 2S_i^A + 2l_{EF} + d_i^A = L \tag{3-12}$$

$$\text{After preforming: } 2l_{EF} + \frac{\pi}{2} d_i^A = L \tag{3-13}$$

$$S_i^A = \sqrt{R^2 - (iL_0)^2}\left(\frac{\pi}{2} - 1\right) \tag{3-14}$$

Where L is the width of the fabric, it is clearly illustrated from Eq.3-14 that axial yarns sliding would be profiled by semicircle that can be approximately proved by the experimental results with braiding angles 55° and 65°. Besides, it is also deduced that the axial yarns sliding is independent of the braided angle. Hence, the maximum axial yarn sliding is almost identical by experimental results with braiding angles 55° and 65° as shown in Fig. 3.19. However, if the material draw-in along axial direction happens, as seen in experimental result with braiding angle 30°, the degree of axial yarns sliding can be restrained by the material draw-in, possibly owing to an augment in friction by in-plane shearing of bias yarns when they have reached the “locking angle”. Hence, the relatively low extent of maximum axial yarn sliding is presented by the performance with braiding angle 30°.

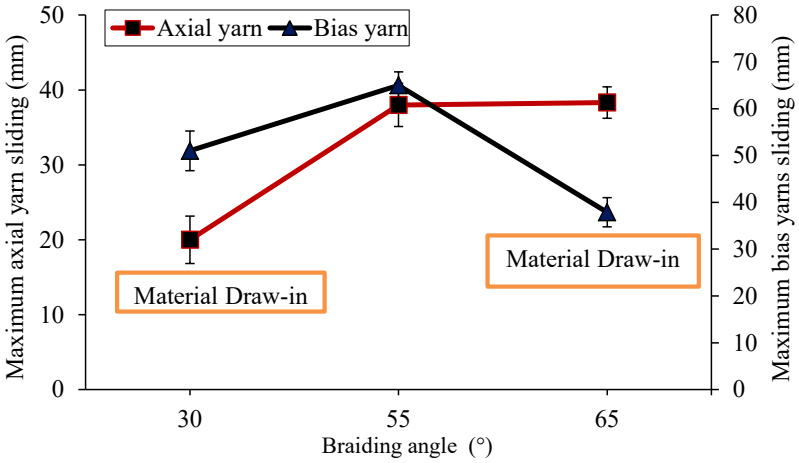

Fig. 3.19. The experimental results concerning maximum yarns sliding with different braiding angles

Evaluation of the geometrical model should resort to the comparison between theoretical and experimental results of sliding for each axial yarn as shown in Fig. 3.20, which experimental results are obtained by braiding angles 55° and 65°. It can be suggested that the geometrical model for axial yarns sliding presents good reliability since theoretical and experimental values show a good agreement. However, if the material draw-in phenomenon would occur in the axial direction of the fabric, this geometrical analysis is no longer adaptable.

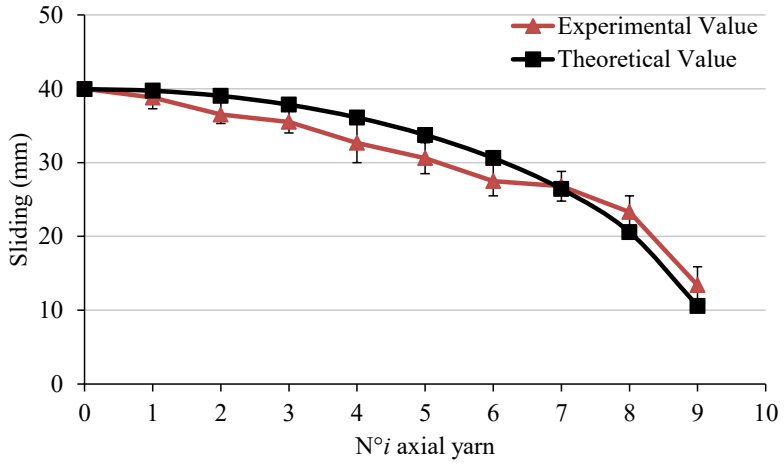

Fig. 3.20. Comparison between theoretical and experimental results with braiding angles 55° and 65°

2. The bias yarns sliding

As the discussion above, the N°i bias yarn ($i \neq 0$) shows the non-identical sliding at two ends. It is defined by the fact that, as shown in Fig. 3.15(a) and Fig. 3.18, point B that is the centre point of N°i segmental yarn within punch zone does not coincide with point C, which is the centre point of whole yarn. Thus, the yarn length under the upper plate at the ends is not identical, the tension at the ends is not equal so that the uneven sliding is observed. It is

suggested that degree of uneven sliding is further enlarged as increasing vertical distance of such two centre points. Even the case that only one end slides, another does not move at all would probably occur if such distance is large enough. It is dominated by the function of enough large difference of tension at the ends. In this case, the maximum value of sliding at one end of bias yarn for different braided angle can be measured as shown in Fig. 3.19.

In this case, the geometrical models for bias yarns are also proposed following the same way of sliding prediction for axial yarns. In this section, the geometrical models for braiding angle over 45° at the ends are expressed in detail. As shown in Fig. 3.15(a), l_{GK} is the whole length of N°i bias yarn before preforming. After preforming, uneven sliding at the ends is accordingly anticipated and can be represented by l_{GH} and l_{JK}, which can be expressed as follows:

$$\text{Before preforming: } l_{GH} + l_{HD} + l_{DC} = \frac{l_{GK}}{2} \tag{3-15}$$

$$\text{After preforming: } l_{HD} + \overset{\frown}{\iota_{DB}} + \overset{\frown}{\iota_{BC}} - \frac{}{2} \tag{3-16}$$

$$S^{B}_{Left} = l_{GH} = \overset{\frown}{\iota_{DC}} - \iota_{DC} \tag{3-17}$$

Where S^{B}_{Left} stands for the sliding at the left end, l_{GH}. S^{B}_{Right} that represents the sliding at the right end, l_{JK}, can be determined as the same way:

$$\text{Before preforming: } l_{CI} + l_{IJ} + l_{JK} = \frac{l_{GK}}{2} \tag{3-18}$$

$$\text{After preforming: } \overset{\frown}{\iota_{CI}} + \iota_{IJ} - \frac{'_{GK}}{2} \tag{3-19}$$

$$S^{B}_{Right} = l_{JK} = \overset{\frown}{\iota_{CI}} \quad \iota_{CI} \tag{3-20}$$

It is directly suggested from the Eq. 3-17 and 3-20 that the sliding at the ends is no longer identical. Based on Fig. 3.18, the maximum punching displacement for N°i bias yarn after preforming is equal to the radius of the ideally punched circle by corresponding yarn, r_i^B, which is half of the length of first portion yarn ideally for N°i bias yarn, d_i^B.

$$r_i^B = \frac{d_i^B}{2} = \sqrt{R^2 - \left(iL_0'\right)^2} \tag{3-21}$$

The distance between two midpoints, l_{BC}, and its corresponding arc length and angle, α, after preforming can be expressed according to Fig. 3.18:

$$\begin{cases} l_{BC} = \dfrac{iL_0'}{\tan\left(\dfrac{\beta}{2}\right)} \\ \alpha = \arcsin\left(\dfrac{l_{BC}}{r_i^B}\right) = \arcsin\left[iL_0' \Big/ \tan\left(\dfrac{\beta}{2}\right)\sqrt{R^2-\left(iL_0'\right)^2} \right] \\ \widehat{\iota_{BC}} - \omega_{r_i} = \arcsin\left[iL_0' \Big/ \left(\tan\left(\dfrac{\beta}{2}\right)\sqrt{R^2-\left(iL_0'\right)^2} \right) \right] \sqrt{R^2-\left(iL_0'\right)^2} \end{cases} \tag{3-22}$$

Therefore, the difference of sliding at the ends, S_d, after preforming can be defined as:

$$\begin{cases} S_d = S_{Left}^B - S_{Right}^B = 2\left(\widehat{\iota_{BC}} \quad \iota_{BC}\right) \\ S_d = 2\left(\arcsin\left[iL_0' \Big/ \left(\tan\left(\dfrac{\beta}{2}\right)\sqrt{R^2-\left(iL_0'\right)^2} \right) \right] \sqrt{R^2-\left(iL_0'\right)^2} - \dfrac{iL_0'}{\tan\left(\dfrac{\beta}{2}\right)} \right) \end{cases} \tag{3-23}$$

From the discussion above, it is clearly deduced that the difference of sliding at the ends is heavily associated with the braiding angle as the fixed diameter of punch shape. The increasing S_d denotes the unbalance of tension at the ends is aggravated, meaning that the case that only one end slides, another does not slide occurs at large degree. Thus, the maximum sliding is positively related to S_d. Fig. 3.21 shows the relation between S_d and braiding angles for each numbered bias yarn. It is clearly seen that S_d for each bias yarn increases from 0° to 45°, decreases from 45° to 90°, and is symmetrical at 45°. Hence, S_d at 55° shows the larger value than S_d at 30° and 65°, accordingly generating the maximum sliding value as shown in Fig. 3.19.

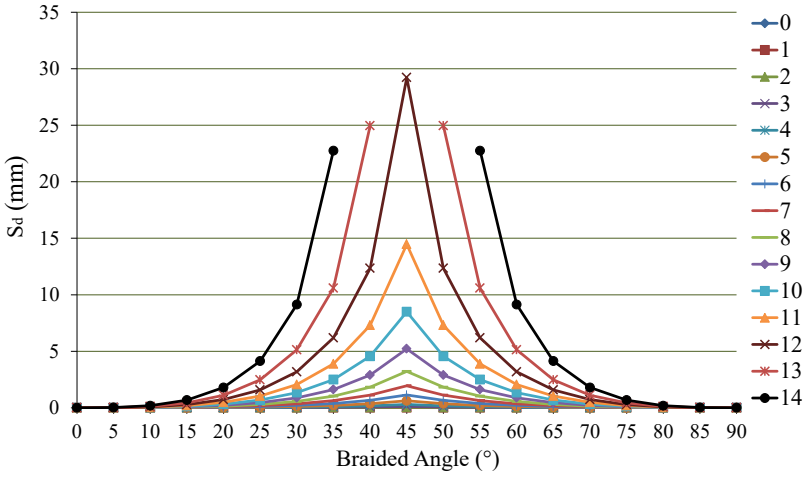

Fig. 3.21. The difference between the ends for each bias yarn, S_d, varied with different braiding angles

Except predicting which braiding angle would show the maximum sliding of bias yarn, the geometrical model for bias yarns sliding can be also compared to experimental results of sliding at one end in order to further verify its accuracy. S_{Right}^{B} can be expressed as follows:

$$S_{Right}^{B}=\frac{\pi\sqrt{R^2-\left(iL_0'\right)^2}}{2}-\arcsin\left[iL_0'\Big/\left(\tan\left(\frac{\beta}{2}\right)\sqrt{R^2-\left(iL_0'\right)^2}\right)\right]\sqrt{R^2-\left(iL_0'\right)^2}-\sqrt{R^2-\left(iL_0'\right)^2}+\frac{iL_0'}{\tan\left(\frac{\beta}{2}\right)} \tag{3-24}$$

Fig. 3.22 shows the comparison between experimental results and the theoretical value of bias yarns sliding at one end. It is believed that the ideology to geometrically model bias yarns sliding is partly adaptable to predict such behaviour, the sliding in first six bias yarns in experimental results shows a relatively good agreement with the theoretical value. This case can be deemed as pure sliding that the degree of unbalanced tension at the ends could not heavily influence the sliding. However, from N°7 bias yarn, the case that only end slides occur, the sliding at another end thus becomes zero. Braiding angle 30° also shows this case but which numbered bias yarn starts doing such case is different from braiding angle 55° and 65°. The geometrical model cannot predict which one yarn starts doing such case because, even though geometrical model could directly present the difference sliding resulted by non-identical tension at the ends, in theory, the function produced by the degree of unbalanced tension at the ends cannot be predictable. The idea of the geometrical model is based on sliding at one end as tension overcomes static friction but disregarding interaction of unbalanced tension at the ends. Therefore, compared to theoretical value and experimental value for axial and bias yarns, it can be concluded that the geometrical model is only adaptable for when yarn length under the upper plate is almost identical at the ends. Once the difference of yarn length at the ends reach the certain threshold value, only one end slides, the sliding could not be precisely predicted by geometrical analysis.

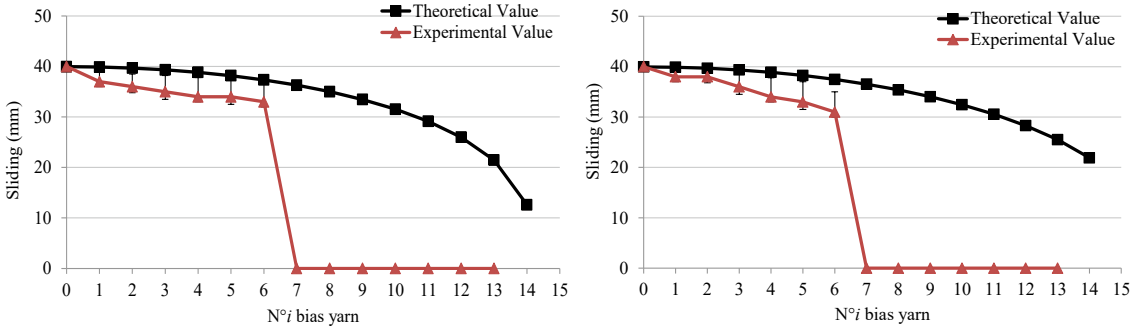

(a) (b)

Fig. 3.22. The comparison between the theoretical and experimental value of sliding for each bias yarn; (a) braiding angle 55°, (b) braiding angle 65°

3.5 The law behind variation of in-plane shearing and material draw-in impacted by braiding angle

As discussion on the tension, it is the reaction force of static friction as yarn sliding occurs instantly. Theoretically, the tension for interlaced bias yarns whose crosspoints are geometrically located at the centre lines of punch zone is identical since the yarn lengths under upper plate on the left and right sides of the centre line are equal as shown in Fig. 3.23. Thus, these interlaced bias yarns are prone to in-plane shear. This is why the in-plane shearing zones only distribute along central lines of fabric at the axial or transversal direction with varied braiding angles as shown in experimental results. The in-plane shearing impels the interlaced bias yarns to rotate towards each other, as classical definition of shearing angle γ, the in-plane shearing zones along the transversal direction of fabric thus show a negative value of the in-plane shearing angle.

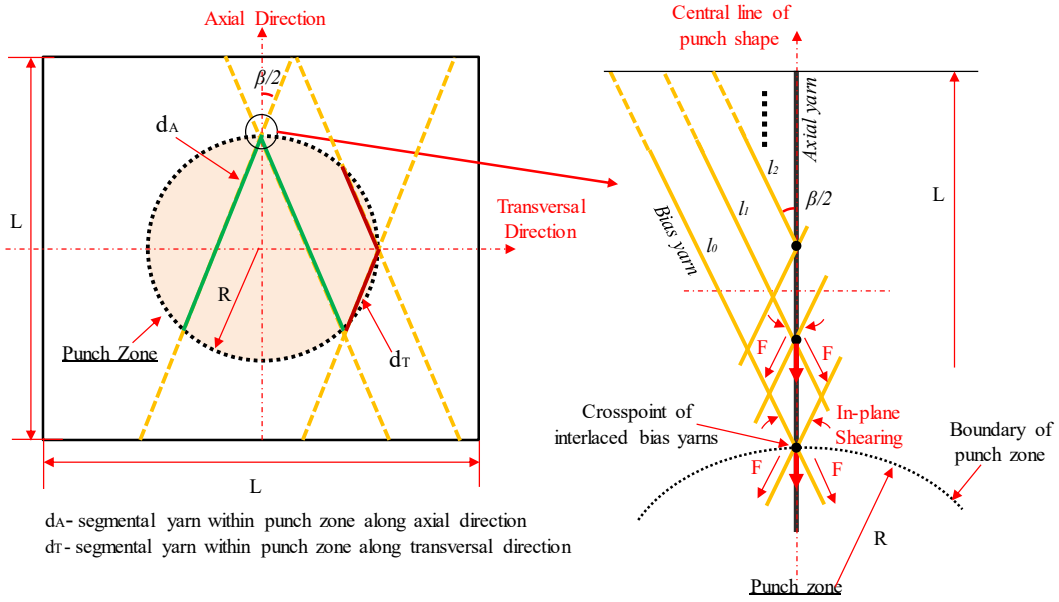

Fig. 3.23. The 2D diagram to describe in-plane shearing during preforming process

Provided that there is crosspoint almost located at the intersection of the boundary of punch zone and central line of punch shape, the maximum length on the left side of this crosspoint can be geometrically defined as l_0 shown in Fig. 3.23. In this case, l_n stands for the yarn length on the left side of each crosspoint that locates at the centre line of punch shape. It is evidently shown that l_n presents the descending tendency, leading to a decreasing tension at continuous crosspoints along the centre line of punch shape from the boundary of punch zone to fabric border. Accordingly, the degree of in-plane shearing for every interlaced bias yarns would also show this tendency. The in-plane shearing angle can be used as the indicator to verify this

prediction as shown in Fig. 3.24, which depicts the in-plane shearing angle variation at braiding angle 55° from the base of the punch zone to preform border where can be divided into three zones after preforming, as shown in Fig. 3.3. The small in-plane shearing angle presents the corresponding small degree of in-plane shearing. It is thus concluded that the degree of in-plane shearing decreases along the central line of punch zone from base of punch zone to the fabric border.

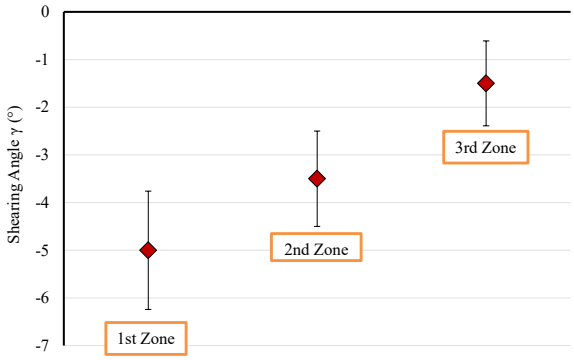

Fig. 3.24. The variation of in-plane shearing angle in the in-plane shearing zone at braided angle 55°

It is also deduced that, from another perspective, l_0 shown in Fig. 3.23 is inversely proportional to the corresponding length of first portion yarn within punch zone projected into X-Y plane along the axial direction, d_A. It means that d_A can indirectly reflect the maximum degree of in-plane shearing along the axial direction. On another direction, the transversal direction of the fabric, d_T can be also defined. d_A and d_T can be calculated geometrically as follows:

$$d_A = 2R\cos\left(\frac{\beta}{2}\right) \tag{3-25}$$

$$d_T = 2R\sin\left(\frac{\beta}{2}\right) \tag{3-26}$$

Indeed, the varied locations of in-plane shearing in different braiding angles shown in experimental results are dominated by this comparison between d_A and d_T. This is because the braiding angle directly impacts the d_A and d_T as fixed hemisphere shape. As shown in Fig. 3.25(a), when the braiding angle is equal to 45°, d_A=d_T, l_0 along with the axial and transversal direction is almost identical so that the in-plane shearing zones or material draw-in could distribute symmetrically along with axial and transversal directions. It can account for the characteristic of the distribution of in-plane shearing in woven fabric preforming in section 3.3. When the braiding angle descends from 45° gradually as shown in Fig. 3.25(b), d_A>d_T, l_0

along axial and transversal directions become uneven, the degree of in-plane shearing along axial yarn direction turns to be large since the friction becomes smaller so that the in-plane shearing is more likely to occur. In contrast, the in-plane shearing along transversal direction becomes obscure gradually since the friction increases so that the in-plane shearing is no longer easy to happen. As braiding angle descends further, material draw-in along axial direction would be detected because when in-plane shearing approach the "locking angle", the stage of in-plane shearing would finish and then the sliding at the end will happen. Meanwhile, the in-plane shearing along transversal direction almost disappears because the friction is too large to generate in-plane shearing, as shown in Fig. 3.13. As increasing the braiding angle from 45° as shown in Fig. 3.25(c) and (d), conversely, the appearance of in-plane shearing and material draw-in along transversal direction shows the similar trend compared to decreasing braiding angle from 45°, and can be verified by the experimental results in braiding angle 55° and 65°, as shown in Fig. 3.14. The in-plane shearing angle γ can be deemed as a character to verify this variation as shown in Fig. 3.26. The in-plane shearing angle γ with negative value shows that the in-plane shearing, or even material draw-in, exhibits in the transversal direction of the fabric. It is clearly deduced from Fig. 3.26 that the difference between d_A and d_T is able to predict which direction shows more obvious in-plane shearing or even material draw-in phenomenon. The material draw-in would possibly occur as enlarging the difference between d_A and d_T.

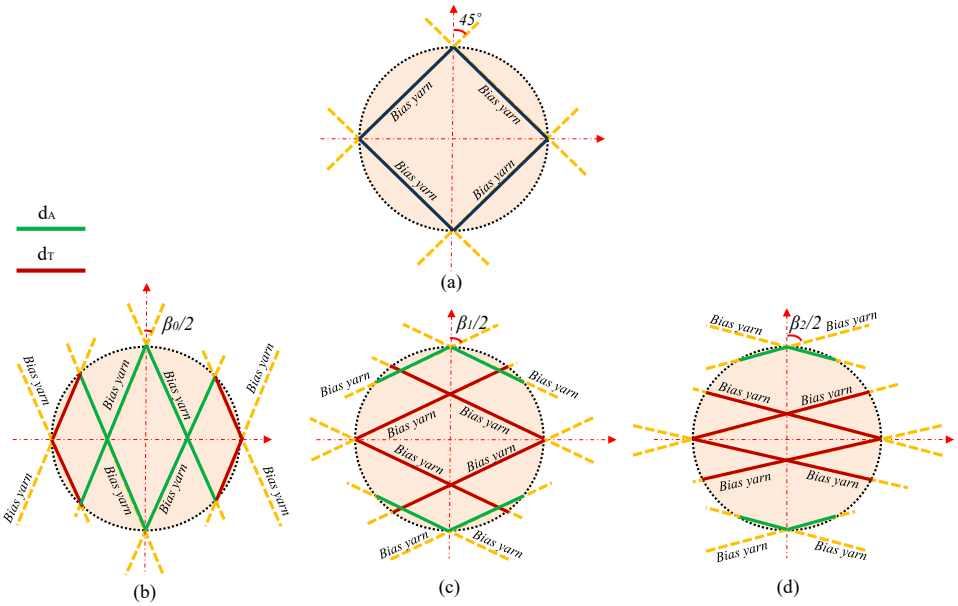

Fig. 3.25. The change of segmental yarn length in punch shape with different braided angles, (a) $\beta/2$=45°, (b) $\beta_0/2$=30°, (c) $\beta_1/2$=55°and (d) $\beta_2/2$=65°

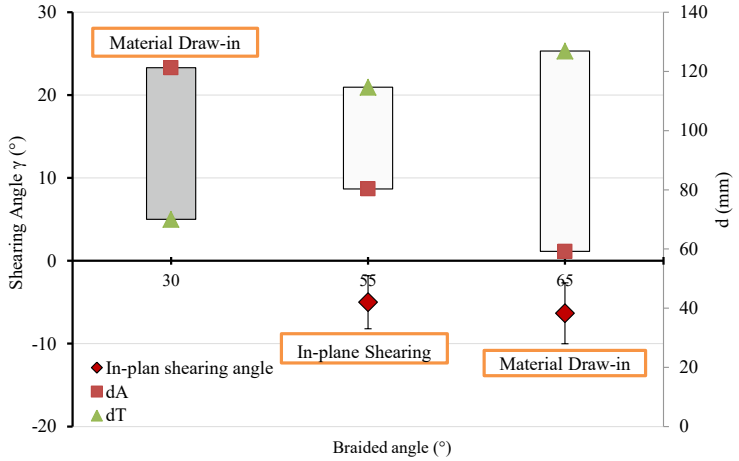

Fig. 3.26. The variation of in-plane shearing angle with different braiding angles

Indeed, due to the fact that when the preform is being performed, the segmental yarn on the surface of hemisphere shape tends to slide towards the base of punch shape, especially for yarns near the base of hemisphere shape, leading to its corresponding segmental yarn in punch zone no more sustaining out-plane bending. Hence, the in-plane shearing along axial yarn direction cannot be seen in experimental results with braiding angle 55° and 65°, even if in theory, the segmental yarn length still exists. Therefore, the braiding angle that produces the in-plane shearing, in theory, is less than it in reality.

3.6 Conclusion of Chapter III

The triaxial braids as promising reinforcements for advanced composite manufacturing are originally investigated with respect to deformability behaviours such as in-plane shearing and yarns sliding, based on various braiding angles through experimental and mechanical analysis. Firstly, the in-plane shearing is only taken place at the intersecting bias yarns under upper plate whose cross-points must be located at centre lines of punch zone, and its degree decreases from base of punch tool to fabric border. Secondly, the variation of in-plane shearing behaviours or even material draw-in is essentially dependent on the difference between the maximum length of portion yarn within punch zone projected in X-Y plane along the axial and transversal direction of the fabric, d_A and d_T, which are decided by the braiding angle as fixed punch tool. Through theoretical analysis and verification, it can be concluded that when $d_A > d_T$, the in-plane shearing phenomenon relatively shows more obvious along the axial direction. Conversely, the in-plane shearing is more visible along the transversal direction of the fabric.

The yarn sliding is divided into axial yarn sliding and bias yarn sliding. Varied braiding angle greatly impacts the characterization of yarns sliding presented in experimental results. Based on the inextensibility of carbon yarn during preforming, the geometrical models are proposed to further precisely describe yarns sliding. Axial yarns sliding, presenting identical sliding at the ends, shows a good agreement between the model and experimental results of sliding for each axial yarn. However, the bias yarn sliding is relatively complicated because of uneven sliding at the ends. The geometrical analysis not only can be used to predict the degree of maximum bias yarn sliding among braiding angles but also partly describe the sliding within pure sliding stage. Furthermore, the mechanical model for yarn is also explored in order to further understand the deformability behaviours.

Therefore, the conclusion can be drawn that the braiding angle greatly impacts the variation of deformability behaviours, which can be geometrically predicted at the perspectives of degree and tendency before preforming. The accuracy of the geometrical model for each yarn sliding is reliable for axial yarns whose sliding during preforming is independent of braiding angle.

IV. THE INVESTIGATION ON MACHINING FIBRE REINFORCED COMPOSITES BY ABRASIVE WATERJET TECHNIQUE

4.1 Introduction

Indeed, the composites manufacturing only could do the near-shape parts that need to be subsequently machined in order to satisfy the requirements in the assembly process, especially for composites with complex shapes that capably replace mental or ceramic parts in aerospace or automobile industries for the purpose of further reducing the weight. Thus, in most cases, the machining process is unavoidable. Abrasive waterjet (AWJ), an emerging processing technique, can promisingly provide the potential advantages in composites machining compared to traditional and other non-traditional processing techniques as discussed in Chapter I. Therefore, this chapter began to explore the material removal mechanism (MRM) of composites machining by AWJ, which is the root cause to generate the defects during machining and basis of improving efficiency via innovations in processing. Besides, the relation between processing parameters and the defects during processing was subsequently attempted to figure out. Based on the exploration in MRM, secondly, the innovations inspired by metal or ceramic AWJ cutting, the multi-pass cutting, was originally introduced into composites machining. Besides, an update in multi-pass cutting process was also proposed and compared with that without update in order to further improve efficiency. Through the investigation in this chapter, it is hopeful to offer instructive suggestions to practitioners in composites manufacturing.

4.2 Materials and experimental set-up

The experiments were conducted by a 5-axis NC waterjet cutter system equipped with an intensifier high output pump from 180 to 420MPa. A nozzle of 0.85mm in diameter and 72.4mm length within an orifice in 0.3mm diameter. The 80# garnets were used as the abrasive particles which are universal and economic in cutting applications. Particularly, a novel abrasive flowrate system was used in this AWJ cutting machine consisting of the belt pulley, focusing on precisely controlling abrasive flowrate under changing the speed of pulley. The specimens ($120\times150\times5mm^3$) were reinforced with carbon fibre (T300) using the epoxy polymer resin matrix in 20 plies. The specimen formed by thermoforming was cross-ply with carbon fibre at 0°，45°/-45°and 90° and the volume content of 60%. Some properties are given in Table 4.1. The cutting length was 45mm and kerf taper is measured at 10mm cross-section of the direction of traverse speed, the cross-section of kerf wall in middle cutting length (10mm-40mm) was taken as the part to measure the surface quality. Noticeably, as

seen in Fig. 1.13(b), when cutting with an inclining nozzle the displacement of energetic particles out from nozzle to surface of specimen becomes larger compared as nozzle vertical to the workpiece surface. Besides, owing to AWJ energy dissipation during the machining, the kerf widths at entrance and exit are different as shown in Fig. 1.13(c).

Table 4.1. Mechanical properties of specimens

Properties	Value
Tensile Modulus (GPa)	138
Transversal Compression	128
Shear Modulus (GPa)	4.51
Poisons Ratio	0.27

The experiments were divided into two parts to investigate cutting performance evaluated by kerf quality and machining efficiency. The first part was to explore material removal behaviours and its relationship between delamination defect. The material removal behaviours were explored by single-pass and multi-pass ways. The second part was subsequently conducted on multi-pass cutting with changed parameters among different passes to improve quality and efficiency as expected. Selection of parameters, especially for traverse speed, in this test was depended on predetermined minimum standoff distance, water pressure and maximum traverse speed (separation speed=800mm/min) allowed for a through-cutting by a single pass. Thus, the minimum traverse speeds selected in this test was more 300mm/min than separation speed and then increased to 2100 or 2300 at an increment of 200mm/min. The pressures were selected at 180MPa and 230MPa, and the standoff distance and abrasive flowrate were always constant.

The kerf taper and surface quality in SCZ characterized by R_a were measurements to distinctly compare the multi-pass cutting with constant and changed parameters among different passes. The control group was conducted by single-pass cutting at half of the separation speed. The experiments content can be seen in Table 2. The kerf taper was easily described by the following formula:

$$\text{Kerf Taper} = \text{Entrance Width} / \text{Exit Width} \tag{4-1}$$

Table 4.2. Experimental details

Projects	Abrasive Flowrate (r/min)	Standoff Distance (mm)	Pressure (MPa)	Impact Angles (°)	Traverse Speed (mm/min)
Multi-pass cutting with constant parameters	100	1.5	180 & 230	0 & 8	1100-2300 (at an increment of 200)
Multi-pass cutting with changed parameters			180 & 230	0	1300,1500,1700
Control Group: Single-pass cutting			180	0	400

The kerf width in all experiments was measured by the VHX-600E super-high magnification lens zoom 3D microscope. Microscopic observations were made under the Scanning Electron Microscope (SEM) to investigate the material removal mechanism and features of the machined surface. Mensuration of surface quality was taken by Taylor-Hobson stylus profilometer. The average measure R_a was produced by three different locations in SCZ. All experiments were conducted two times and the results were an average of these measurements.

4.3 The material removal mechanism of fibre reinforced composites by AWJ machining

In general, the non-through cutting produces the pocket at the bottom of the kerf due to unordered jet upward deflection [189]. As shown in Fig. 4.1(a), the kerf shape at non-through cutting is not always pocket but cutting front deflection occasionally. This is probably related to the material properties such as anisotropy and different erosion rates among fibres and matrix. Hence, the kerf produced at first-pass cutting occasionally presented different shapes that could influence the performance at second pass such as the irregular pits randomly occurring at kerf wall, as shown in Fig. 4.1(b). In addition, the delamination does not occur at the first-pass cutting because of enough bonding strength between layers and residual stiffness to resist jet impact. Hence, the multi-pass cutting could be applied to such FRPs machining. But surface quality at lower zone could not be evaluated accurately because of random pits as seen in Fig. 4.1(c).

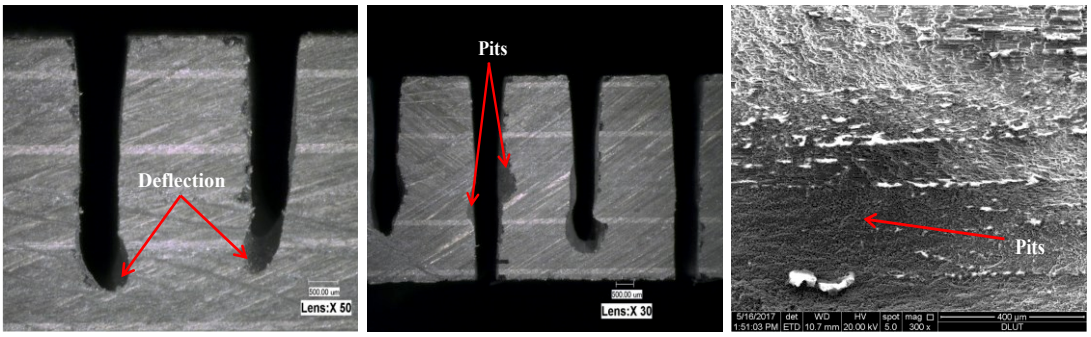

(a) (b) (c)

Fig. 4.1. Kerf characteristics in multi-pass cutting, (a) kerf shape at first-pass cutting (non-through cutting), (b) kerf shape at multi-pass cutting and pits and (c) enlarged microphoto of pits at bottom of kerf wall

The material removal behaviours in AWJ machining multidirectional fibre reinforced composites were investigated by SEM and representative micrographs of typical kerf surfaces are shown in Fig. 4.2. The initial damage zone (IDZ) appears irregularly with pits caused by abrasive particles with maximum energy out of the nozzle, producing non-uniform damage zone as exhibited in Fig. 4.2(a) [213]. At various depth of cut, the machined surface appears relatively smoother at smooth cutting zone (SCZ) because of the impacting at a shallow angle (as shown in Fig.1). The grooves with less extent can be observed randomly and their orientations are parallel to the jet direction from Fig. 4.2(b). This is probably attributed to vibration due to nozzle traverse system or unsteadiness of process parameters [214]. In the rough cutting zone (RCZ), the grooves are more noticeable and described as striations or waviness belonged to the AWJ property that impacting at a large angle. The striations amplitude increases as an augment in depth ignored apparently different orientations of laminates. In addition, the fibre pullout randomly occurs in fibre bundles leaving large cavities in the machined surface, which is distinctly shown in the interface of junction between two different orientations of laminates in RCZ. It is probably caused by relatively weaker bonding stress at the interface so that debonded interface between fibre and matrix is prone to exist. Furthermore, the fibre pullout in RCZ is more obvious than in SCZ since brittle fracture is the primary removal mechanism of fibres rather than microcutting (shear). The Fig. 4.3 clearly shows the difference at end of fibres in 45°and 90°orientations in RCZ and SCZ, it is suggested that the microcutting is prevailingly dominant removal mechanism of fibres in SCZ. When cutting further down in the lower region, the abrasive particles with insufficient energy could not effectively cut or trim but ceaselessly impact fibres. Thus, the fibres at RCZ are mostly removed by brittle fracture, resulting in the fibre pullout seriously. Contrastively, the matrix is obviously removed by plastic deformation as shown in Fig. 4.2(b) and (c), and

the mechanism belongs to microcutting or plough at relatively small and large impact angle in varying depth of cut.

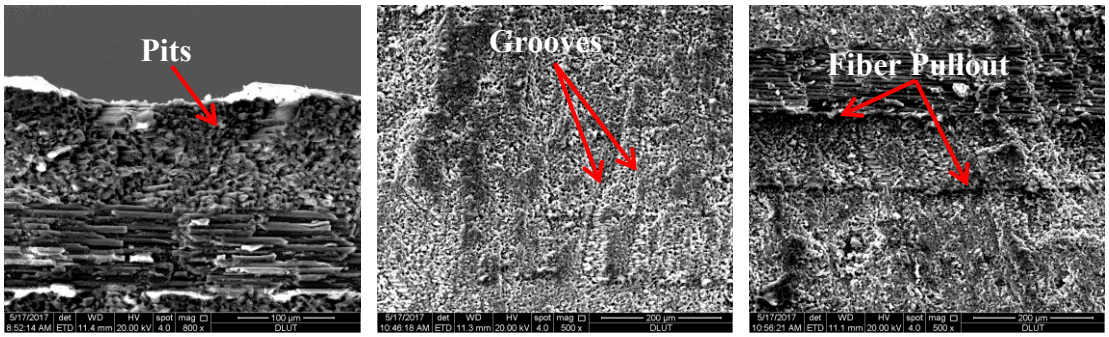

(a) (b) (c)

Fig. 4.2. The three zones generated by AWJ cutting, (a) IDZ, (b) SCZ and (c) RCZ

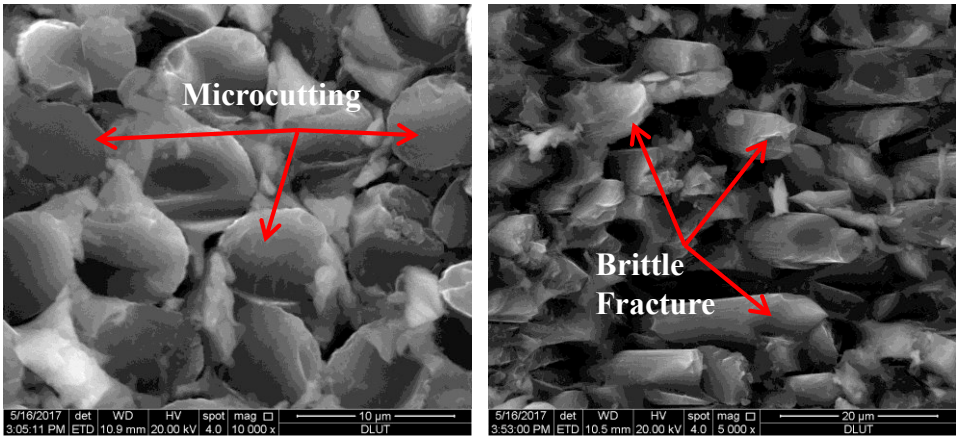

(a) (b)

Fig. 4.3. End of fibres in SCZ and RCZ, (a) 90° and (b) 45°

When cutting depth increases to exit zone, the abrasive particles further reduce the energy so that fibres are heavily subjected to microbending for lack of adequate supporting at the bottom of the workpiece. Thus, the fibres deform elastically under the jet pressure and then displacement increases. The large extent of debonding between fibres and matrix can be observed at the last laminate of the exit zone as shown in Fig. 4.4(a). This debonding could produce matrix cracks that are able to propagate and finally generate the inter-laminar delamination. In contrast, the total abrasive particles at AWJ cutting front increases as reducing the traverse speed greatly so that cutting energy in per unit area enhances [215], leading to the microcutting is still dominant removal mechanism of fibres and matrix at lower zone of the kerf. Thus, the delamination does not appear, as seen in Fig. 4.4(b).

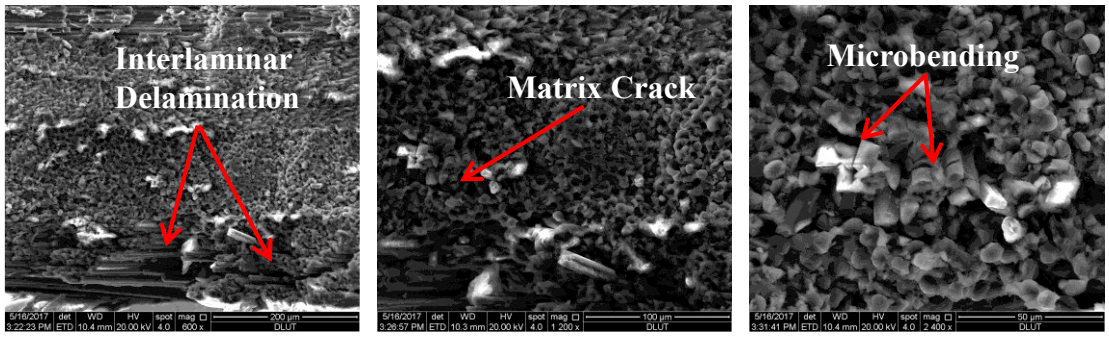

(a)

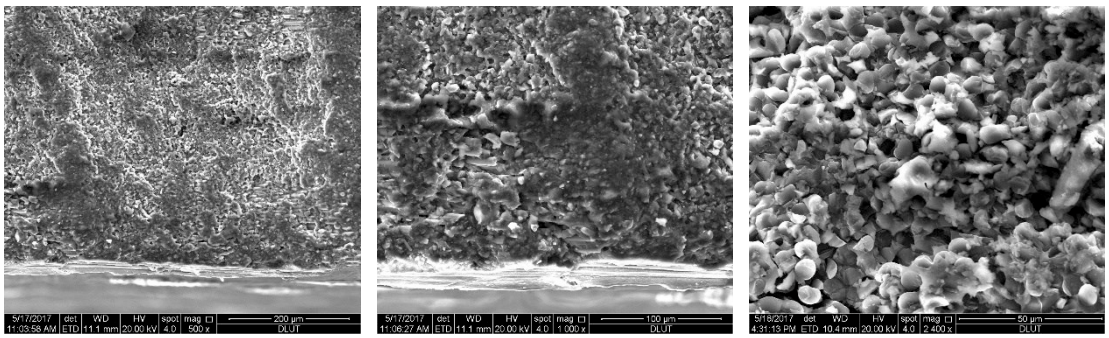

(b)

Fig. 4.4. Comparing the distinct zones machined with different traverse speeds, (a) a multi-pass cutting at 2300mm/min traverse speed, (b) a single-pass cutting at 400mm/min traverse speed

Consequently, it is concluded that the material removal mode primarily appears to be the microcutting, plough and brittle fracture of fibres and matrix. Meanwhile, the delamination at exit zone is depended on removal mechanism at that phase, i.e. when matrix and fibres are removed by microcutting, the delamination does not appear. While the fibres are removed by brittle fracture, the inter-laminar delamination is produced. Hence, the processing parameters such as pressure and traverse speed heavily influence the delamination since they significantly affect the energy of particles at cutting front. And if the FRPs have enough residual stiffness after non-through cutting pass, the delamination also would not happen. This residual stiffness is heavily associated with bonding strength between layers. Hence, the delamination is also highly dependent on the properties of FRPs being processed.

4.4 The evaluation of kerf quality produced by multi-pass cutting process

The discussion in Section 4.3 proves that the multi-pass cutting process, which has been verified the valuation in the improvement of cutting quality and efficiency, can be introduced

into composites machining, yet carefully considering the appropriate processing parameters selected, which is the main objective in this section. Besides, the applied multi-pass cutting process keeps the constant processing parameters among the cutting passes which could introduce a harmful effect in cutting performance due to an augment in standoff distance indeed during the different passes. The remedies consist of increasing pressure or decreasing traverse speed, indicating that the changing parameters among the cutting passes could improve the negative effect by constant parameters during cutting passes.

4.4.1 Kerf taper

Fig. 4.5(a) shows the kerf taper in multi-pass cutting with constant parameters. It is typically found that increasing pressure could effectively decrease kerf taper, the maximum decrease is approximately 50%. The traverse speed influencing kerf taper at two pressures is almost identity that increasing traverse speed could expectedly increase the kerf taper. Besides, the inclined nozzle at relatively low traverse speed 1100mm/min can distinctly reduce kerf taper by almost 38%. As increasing the traverse speed, the difference in kerf taper between vertical and inclined angle is small. Indeed, the inclined nozzle, however, does not affect the kerf taper greatly as expected. This is because standoff distance at second-pass becomes large that influences the cutting power more heavily than inclined nozzle. By contrast with single-pass cutting, the multi-pass cutting with constant parameters only shows a slightly advantage over single-pass cutting at relatively low traverse speed (1100-1300mm/min) with higher pressure (230MPa). Over these values, the multi-pass cutting with constant parameters produces higher kerf taper without any advantages.

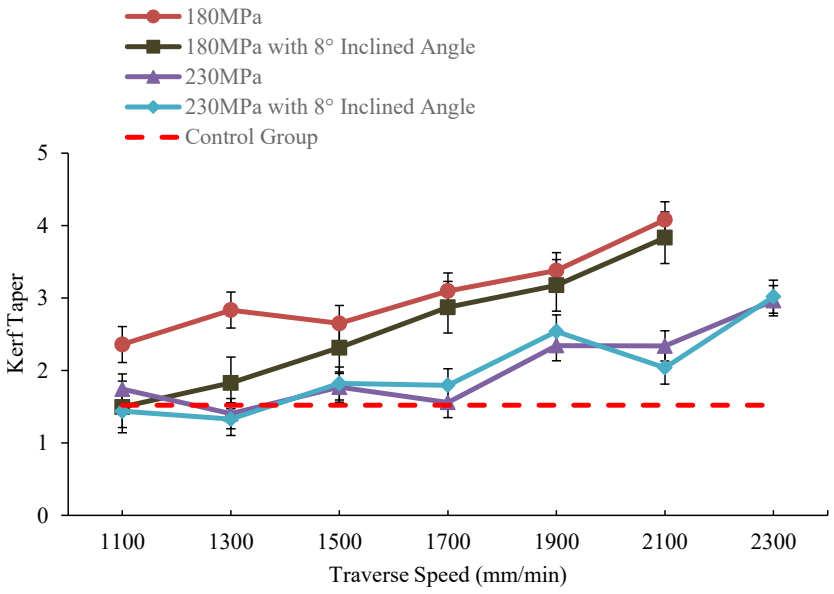

(a)

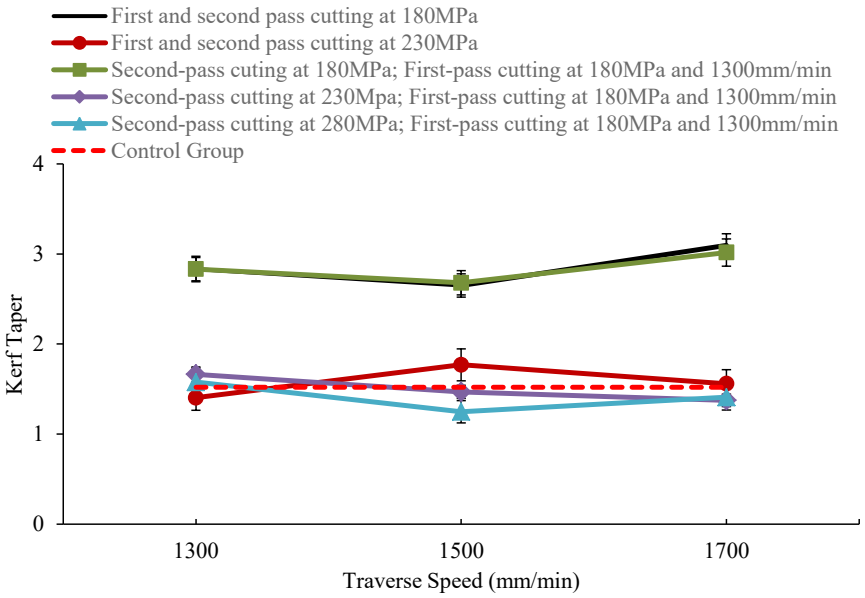

(b)

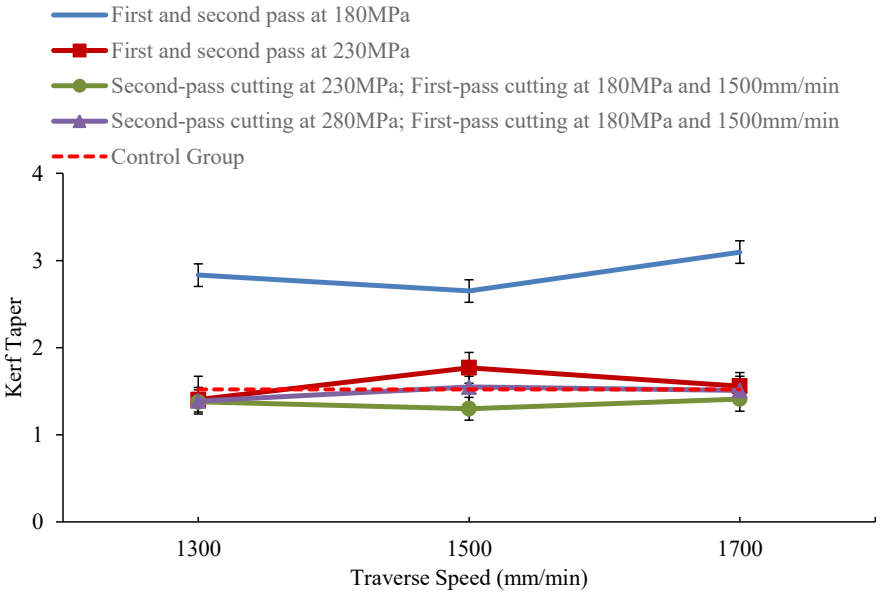

(c)

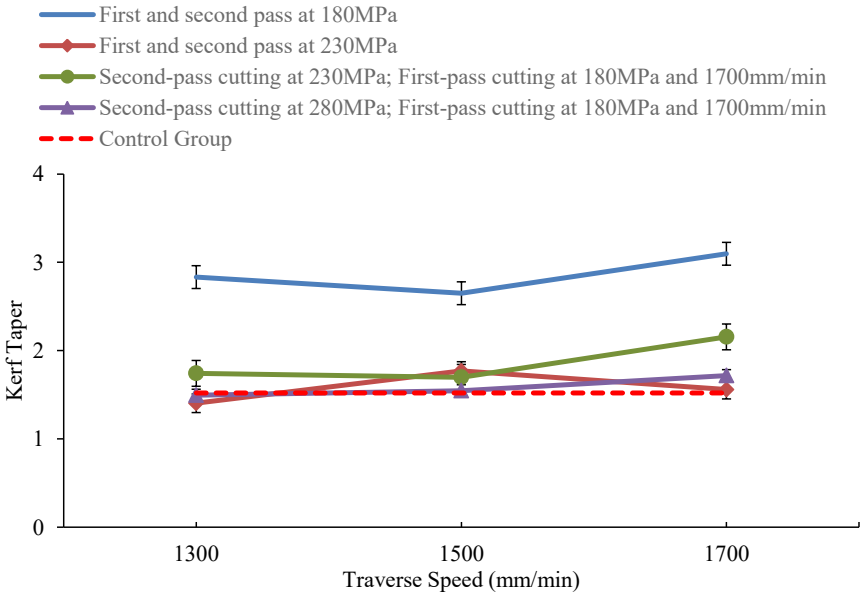

(d)

Fig. 4.5. Comparing kerf taper produced by multi-pass cutting with constant and changed parameters including pressure and traverse speed

Compared to multi-pass cutting with changed parameters as shown in Fig. 4.5(b), however, the kerf taper decreases remarkably, especially for first-pass cutting at 180MPa, highly increasing pressure at second-pass cutting could compensate the disadvantages caused by larger standoff distance at second-pass cutting following first-pass cutting. For instance, the kerf taper decreased almost 53% in multi-pass cutting with changed parameters including first-pass cutting at 180MPa and 1300mm/min, second-pass cutting at 280MPa and 1700mm/min compared with multi-pass cutting with constant parameters that first-pass and second-pass cutting at 180MPa and 1300mm/min. Thus, kerf taper can be improved by increasing pressure at second-pass cutting even though at relatively high traverse speed. Meanwhile, the kerf taper generated by multi-pass cutting with changed parameters (first-pass cutting at 180MPa and 1300mm/min, second-pass cutting at 230MPa) is almost equal to it produced by single-pass cutting (Control group). Thus, it means that appropriate parameters selected at second-pass cutting could achieve the cutting quality obtained by single-pass cutting relatively.

However, Fig. 4.5(b) also shows that only increasing the traverse speed at second-pass cutting with constant pressure does not appear the advantage over second-pass cutting without changed parameters. The value of kerf taper performed by first-pass cutting at 180MPa and 1300mm/min, second-pass cutting at 180MPa with different traverse speeds is nearly identical with it produced by both cutting passes at constant parameters (180MPa). Hence, it can be

induced that the cutting efficiency can be improved slightly as expected without sacrifice of cutting performance. Moreover, Fig. 4.5(b) and (c) also clearly express that first-pass cutting at 180MPa and 1300mm/min and 1500mm/min, second-pass cutting at 230MPa with varying traverse speeds could produce the nearly identical kerf taper as multi-pass cutting with constant parameters at 230MPa. It thus infers that under the almost same output performance, the energy can be saved to a small extent by decreasing pressure from 230MPa to 180MPa at first-pass cutting.

Moreover, when increasing traverse speed at first-pass cutting from 1500mm/min to 1700mm/min at 230MPa, the second-pass cutting with changed parameters is not superior to it with constant parameters (230MPa and 1700mm/min) in this situation as shown in Fig. 4.5(d). The kerf taper generated by multi-pass cutting with constant parameters (230MPa and 1700mm/min) decreases almost 28% compared with first-pass cutting at 180MPa and 1700mm/min, second-pass cutting at 230MPa and 1700mm/min. The increasing pressure only at relatively high traverse speed is no longer effective. It is probably explained by the residual material thickness left by first-pass cutting with relatively high traverse speed exceeds a certain critical value that is enough to influence the kerf taper distinctly, resulting in a reduction of effectiveness with increasing pressure. Therefore, it can be concluded that multi-pass cutting with changed parameters should arrange the relatively low traverse speed at first-pass cutting and high traverse speed at second-pass cutting.

Fig. 4.6 presents the cutting time during multi-pass cutting that the efficiency can be compared between processes at constant and changed parameters. In addition, the kerf tapers produced by multi-pass cutting with changed parameters and control group are also put forward to conveniently express the efficiency extent. At first, it is clearly seen that the multi-pass cutting can improve cutting efficiency compared with control group-single pass cutting under the condition that the kerf tapers generated by multi-pass and single-pass cutting are almost identical. For example, the cutting time used by multi-pass cutting at 180MPa with 1300mm/min and 1500mm/min decreases almost 38% compared with the control group without sacrifice of kerf taper quality. Indeed, even though the multi-pass cutting time excludes the return stroke time in present experiments, the multi-pass cutting also shows the superiority in cutting efficiency if the cutting length is enough long since the return stroke time is relatively much shorter than cutting time in reality. However, although further increasing traverse speed in multi-pass cutting (1700mm/min) can improve efficiency more effectively, the kerf taper produced by multi-pass cutting becomes larger than the control

group, especially for first and second pass both at 1700mm/min. Among multi-pass cutting with constant and changed parameters, the multi-pass cutting with changed parameters could further decrease the cutting time. The efficiency can be further improved by almost 13% as the condition that kerf taper produced varies in a small extent.

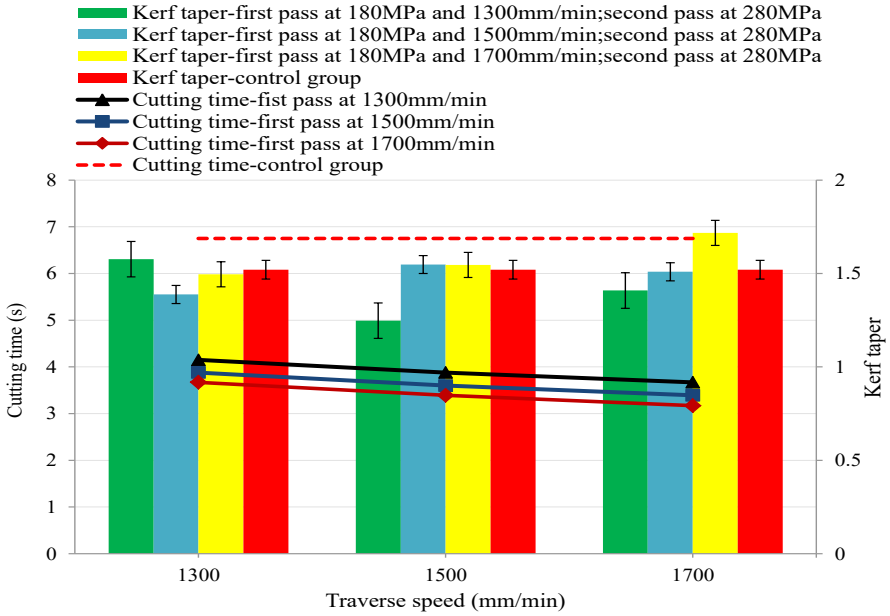

Fig. 4.6. Cutting time and kerf taper in multi-pass cutting process

4.4.2 Surface quality

As the discussion in Section 4.3, the irregular pits can be detected in IDZ and RCZ, the SCZ surface shows the relatively smooth property without much fibre pull-out and pits. Thus, the SCZ surface is measured by R_a to directly evaluate and compare the multi-pass cutting with constant and changed parameters. Fig. 4.7 shows the R_a is influenced by multi-pass cutting with constant and changed parameters. It is typically discovered in Fig. 4.7(a) that increasing the traverse speed and pressure could undesirably increase and expectedly decrease the R_a, which is similar to the mental cutting performance [216]. However, the difference among these parameters appeared distinctly only if traverse speed exceeds the 1500mm/min. Further increasing traverse speed over 1500mm/min, the fewer particles and overlapping could reduce the surface quality greatly [187]. It is also probably deduced that the relatively high pressure with the inclined nozzle is probably more sensitive to high traverse speed that deteriorates the surface quality at the multi-pass cutting process. Furthermore, it is interesting to find that the R_a in multi-pass cutting is almost equal (180MPa) and less (230MPa) than it in single-pass cutting when traverse speed in multi-pass cutting is less than 1500mm/min. Especially for 230MPa with 1500mm/min, the R_a reduces almost 21% compared to the control group. Thus,

the multi-pass cutting process could not only improve the surface quality but also enhance the efficiency to some extent if the parameters are approximately selected.

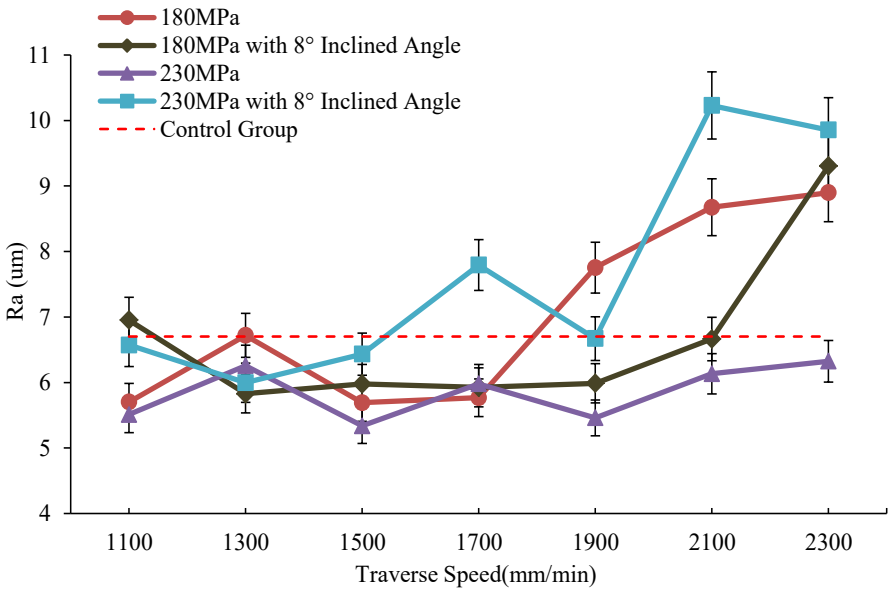

(a)

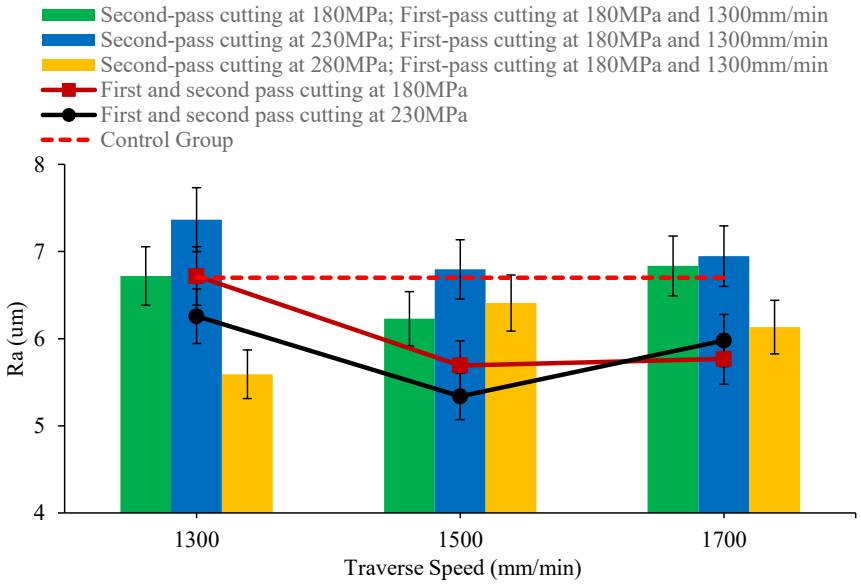

(b)

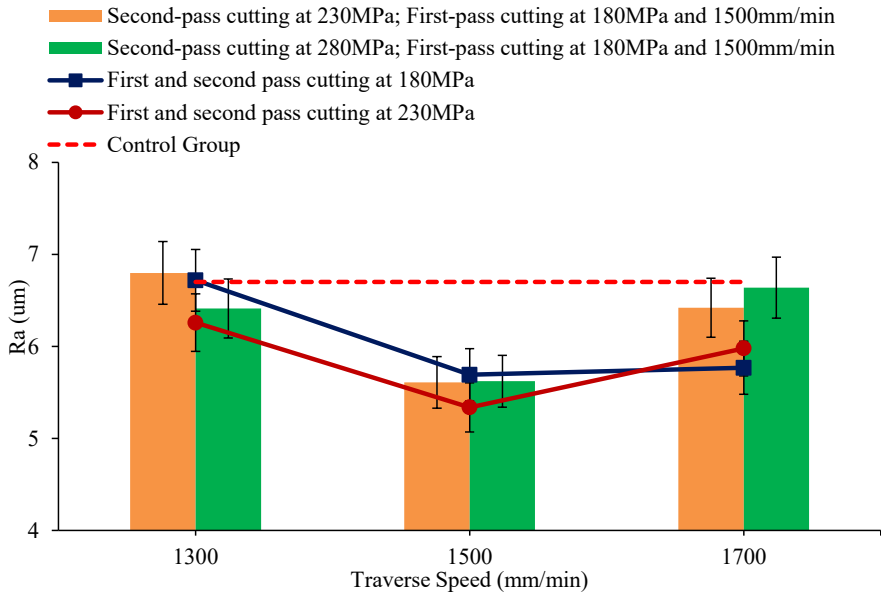

(c)

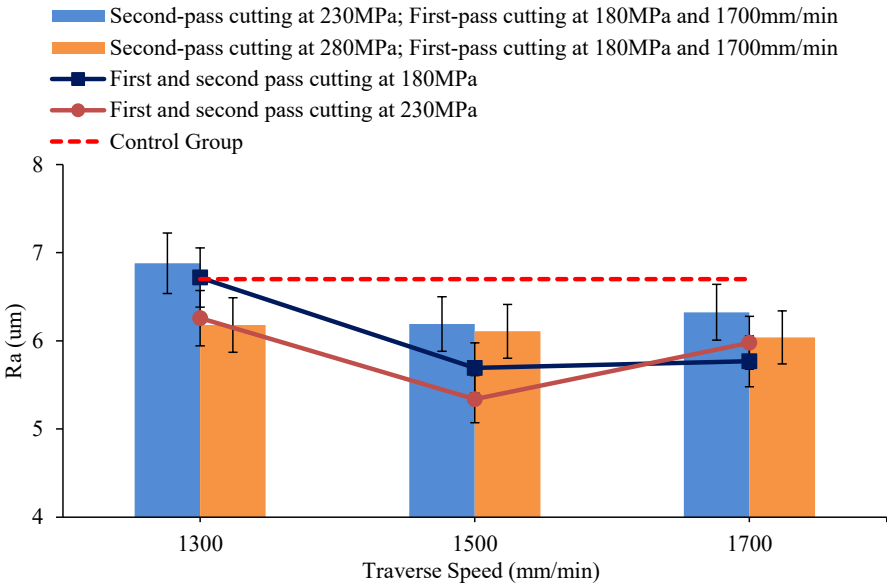

(d)

Fig. 4.7. Comparing R_a produced by multi-pass cutting constant and changed parameters

Considering the multi-pass cutting with changed parameters, however, the R_a measured in multi-pass cutting with changed parameters is generally higher than it measured with constant parameters except greatly increasing pressure to 280MPa in second-pass cutting with 1300mm/min when the first-pass cutting at 180MPa and same traverse speed, which could decrease R_a almost 18%. Comparatively, For instance, the R_a produced by second–pass cutting at 230MPa and 1500mm/min, first-pass cutting at 180MPa and 1300mm/min is 21% higher than that with constant parameters of multi-pass cutting (230MPa and 1500mm/min). Hence, it is inferred that the multi-pass cutting with changed parameters does not improve the surface

quality except for increasing pressure greatly at second-pass cutting with the same traverse speed. This is attributed to the different traverse speeds between first-pass and second-pass cutting that could probably produce the new grooves at the base of first-cutting pass. On the other hand, the effective width of removal material in jet increases as increasing pressure, which could make the previous grooves resulted by first-pass cutting deeper. Thus, the interaction of these two sides could deteriorate the surface quality. However, the greatly increased pressure in second-pass cutting at the same traverse speed as first-pass cutting could probably rebuild rather than deteriorate the surface because enough effective width and potential fragmentation by high pressure reduce the size of abrasive particles that could effectively enhance the surface quality with sacrifice of cutting depth [217]. Thus, the surface quality could be improved as discussed in multi-pass cutting with highly changed pressure at relatively low traverse speed 1300mm/min. Therefore, the multi-pass cutting with changed parameters generally does not show the advantage over with constant parameters.

4.5 Conclusion of Chapter IV

A study of kerf quality on CFRPs cutting by AWJ multi-pass process is originally presented on this Chapter. The material removal behaviours are firstly investigated by SEM and make a relation with delamination. Micro-machining including microcutting, plough and brittle fracture of fibres and matrix is material removal mechanism. It is found that the delamination at the exit zone is dependent on removal mechanism which is dominant, i.e. when matrix and fibres are removed by microcutting, the delamination does not appear. While the fibres are removed by the brittle fracture and absence of sufficient supporting, the inter-laminar delamination is produced at exit zone. The other zones and un-through cutting do not appear delamination because of enough bonding strength between layers and residual stiffness provided by un-cut layers. This investigation lays a foundation for originally applying the multi-pass cutting on FRPs.

Secondly, the multi-pass cutting on FRPs is discussed and makes a comparison between constant and changed parameters. The kerf taper reduced obviously by multi-pass cutting with changed parameters, especially for increasing pressure at second-pass cutting when first-pass cutting at relatively low pressure (180MPa), the greatest reduction is about 53% without sacrifice of efficiency. It is also suggested from experimental analysis that the multi-pass cutting with changed parameters not only decreased the kerf taper but also improved efficiency, appropriate transverse speed selected at different passes could improve efficiency

almost 13% within roughly identical kerf taper. Meanwhile, in order to further reduce the kerf taper, multi-pass cutting with changed parameters should arrange the relatively low traverse speed at first-pass cutting and high traverse speed at second-pass cutting. Lastly, the R_a, which is a representation of surface quality in SCZ, is also studied in multi-pass cutting process. The surface quality generated by changed parameters is generally worse than it by constant parameters unless greatly increasing pressure at second-pass cutting with relatively low and same traverse speed (1300mm/min) as first-pass cutting. Therefore, it is concluded that the multi-pass cutting could be used to further improve FRPs cutting quality, in which material properties including debonding strength and stiffness are enough to avoid delamination. Besides, the efficiency also can be improved as appropriate traverse speed selected at different passes.

V. GENERAL CONCLUSION

5.1 Conclusion

The braided fabrics as promising reinforcements for composites with complex shapes are investigated in this thesis in terms of mechanical properties and deformability behaviours during the preforming process, which is first stage of manufacturing process for composites with complex shapes. The in-plane shearing property, which is the most important character in mechanical properties, is analysed on the basis of kinematic analysis based on the proposed geometrical condition of fabrics. By comparing theoretical value and experimental results, it can be concluded that, firstly, the bias extension can also determine the in-plane shearing property of triaxial braided fabrics. Secondly, the kinematical model is able to predict and describe the in-plane shearing property of braided fabrics due to a good agreement between theoretical value and experimental results. Fabrics parameters such as braiding angle and number fibre of axial yarns are discussed with respect to mechanical and thermo-mechanical characteristics based on experimental analysis. It is clearly observed that braiding angle is a crucial factor to determine the character in mechanical properties including deformation and friction. An increasing braiding angle improves the deformation while increases the friction during bias extension tests.

The deformability behaviours during preforming process are discussed in the second part of the thesis. The in-plane shearing and yarns sliding are the primary deformability behaviours that are firstly investigated via varying preforming blank-holder pressure and braiding angle. The mechanical models for yarns are proposed to realize the mechanism of deformability behaviours. The yarns sliding can be classified along radial and longitudinal yarn direction, the former can be heavily impacted by blank-holder pressure but the latter is not. If the yarns sliding along longitudinal yarn direction steps into punch zone, one defect that can be defined as fibre vacancies will be observed. Hence, the sliding along longitudinal yarn direction whatever for axial and bias yarns is analysed on basis of geometrical model, and experimental results show these models could roughly predict yarns sliding along longitudinal yarn direction. In-plane shearing behaviour is also detected during preforming process, which shows the difference in terms of magnitude and location that are influenced by varied braiding angle. The model based on the braiding angle, punch tool diameter and fabric size could predict the variation of in-plane shearing behaviour. Through theoretical and experimental analysis, it is clearly included that the braiding angle plays a crucial effect on deformability behaviours during preforming process. The law behind can be described via geometrical

analysis in some degree, which could help or inspire someone who engages in or is interested in composites manufacturing.

The machining properties of composites including material removal mechanism and innovation are also discussed by abrasive waterjet technique, which is a promising non-conditional machining technique. Micro-machining including microcutting, plough and brittle fracture of fibres and matrix is material removal mechanism. Besides, the multi-pass cutting with changed parameters is originally applied to composites machining. It is experimentally analysed that the multi-pass cutting with changed parameters could compensate the deficiency in multi-pass cutting with constant parameters and further improve cutting quality and efficiency.

5.2 Perspectives

As expanding application of triaxial braided reinforcements in aerospace and automobile manufacturing, the model to analyse mechanical properties need to be set up. It is important to add the mechanical properties of axial yarns to kinematic model of bias-axial braided fabrics presented in this thesis, and verify its accuracy in order to provide the suggestions for worker in composites manufacturing. On the other hand, the yarns tension, which is generated by out-plane bending during preforming process, should be also analysed quantitatively because it is definitely a root reason causing variation of deformability behaviours. This analysis should be related to braiding angle, punch tool and fabric parameters that have been certified the effect on the variation of deformability behaviours in this thesis. The perspectives detailed as follows:

- Experimental results on the in-plane shear behaviours of braided preforms should be followed and verified by implementation in finite element simulation models
- Preforming tests with other punch shapes such as square and triangle
- Optimizing the braids structure relative to deformability behaviours, for examples, biaxial/triaxial, braiding angle and yarns number
- Coupling in-plane shear and tensile behaviours for triaxial preforms, according to the tension model of axial yarns
- Investigate on the process routing for composites machining by abrasive waterjet technique based on the material removal mechanism
- Exploring the composite milling by abrasive waterjet technique

Reference

[1] Fazeli M, Florez JP, Simão RA. Improvement in adhesion of cellulose fibers to the thermoplastic starch matrix by plasma treatment modification. Compos Part B Eng 2019;163:207–16. doi:10.1016/J.COMPOSITESB.2018.11.048.

[2] Haim Abramovich. Introduction to composite materials. Woodhead Publishing; 2017. doi:10.1016/B978-0-08-100410-4.00001-6.

[3] Chung DDL. Introduction to Carbon Composites. Carbon Compos., Butterworth-Heinemann; 2016, p. 88–160. doi:10.1016/b978-0-12-804459-9.00002-6.

[4] Sheikh-Ahmad JY. Machining of polymer composites. 2009. doi:10.1007/978-0-387-68619-6.

[5] Fernandes EM, Correlo VM, Chagas JAM, Mano JF, Reis RL. Properties of new cork–polymer composites: Advantages and drawbacks as compared with commercially available fibreboard materials. Compos Struct 2011;93:3120–9. doi:10.1016/J.COMPSTRUCT.2011.06.020.

[6] Dandekar CR, Shin YC. Modeling of machining of composite materials: A review. Int J Mach Tools Manuf 2012;57:102–21. doi:10.1016/j.ijmachtools.2012.01.006.

[7] Saheb DN, Jog JP. Natural fiber polymer composites: A review. Adv Polym Technol 1999;18:351–63. doi:10.1002/(SICI)1098-2329(199924)18:4<351::AID-ADV6>3.0.CO;2-X.

[8] Faruk O, Bledzki AK, Fink H-P, Sain M. Biocomposites reinforced with natural fibers: 2000–2010. Prog Polym Sci 2012;37:1552–96. doi:10.1016/J.PROGPOLYMSCI.2012.04.003.

[9] Fazeli M, Keley M, Biazar E. Preparation and characterization of starch-based composite films reinforced by cellulose nanofibers. Int J Biol Macromol 2018;116:272–80. doi:10.1016/J.IJBIOMAC.2018.04.186.

[10] Liu Z, Erhan SZ, Akin DE, Barton FE. “Green” composites from renewable resources: Preparation of epoxidized soybean oil and flax fiber composites. J Agric Food Chem 2006;54:2134–7. doi:10.1021/jf0526745.

[11] Zini E, Scandola M. Green composites: An overview. Polym Compos 2011;32:1905–15. doi:10.1002/pc.21224.

[12] Soutis C. Fibre reinforced composites in aircraft construction. Prog Aerosp Sci 2005;41:143–51. doi:10.1016/J.PAEROSCI.2005.02.004.

[13] Hayat MD, Singh H, He Z, Cao P. Titanium Metal Matrix Composites: An Overview. Compos Part A Appl Sci Manuf 2019. doi:10.1016/J.COMPOSITESA.2019.04.005.

[14] Chung DDL, Chung DDL. Ceramic-Matrix Composites. Carbon Compos 2017:467–531. doi:10.1016/B978-0-12-804459-9.00008-7.

[15] Applications I. Carbon Fiber Composites. Butterworth-Heinemann; 2011. doi:10.1016/0010-4361(78)90646-8.

[16] Altin Karataş M, Gökkaya H. A review on machinability of carbon fiber reinforced polymer (CFRP) and glass fiber reinforced polymer (GFRP) composite materials. Def Technol 2018;14:318–26. doi:10.1016/J.DT.2018.02.001.

[17] Mitchell BS. An introduction to materials engineering and science for chemical and materials engineers. John Wiley; 2004.

[18] M’Saoubi R, Axinte D, Soo SL, Nobel C, Attia H, Kappmeyer G, et al. High performance cutting of advanced aerospace alloys and composite materials. CIRP Ann - Manuf Technol 2015;64:557–80. doi:10.1016/j.cirp.2015.05.002.

[19] Hashish M. Trimming of Cfrp Aircraft Components. WJTA Am Waterjet Conf 2013.

[20] Bakis CE, Bank LC, Brown VL, Cosenza E, Davalos JF, Lesko JJ, et al. Fiber-Reinforced Polymer Composites for Construction—State-of-the-Art Review. J Compos Constr 2002;6:73–87. doi:10.1061/(ASCE)1090-0268(2002)6:2(73).
[21] Mallick P. Fiber-Reinforced Composites. vol. 20072757. CRC Press; 2007. doi:10.1201/9781420005981.
[22] Ku H, Wang H, Pattarachaiyakoop N, Trada M. A review on the tensile properties of natural fiber reinforced polymer composites. Compos Part B Eng 2011;42:856–73. doi:10.1016/J.COMPOSITESB.2011.01.010.
[23] Slayter Games. Method and apparatus for making glass wool, 1933.
[24] Sathishkumar T, Satheeshkumar S, Naveen J. Glass fiber-reinforced polymer composites – a review. J Reinf Plast Compos 2014;33:1258–75. doi:10.1177/0731684414530790.
[25] Joshi S., Drzal L., Mohanty A., Arora S. Are natural fiber composites environmentally superior to glass fiber reinforced composites? Compos Part A Appl Sci Manuf 2004;35:371–6. doi:10.1016/J.COMPOSITESA.2003.09.016.
[26] Totry E, Molina-Aldareguía JM, González C, LLorca J. Effect of fiber, matrix and interface properties on the in-plane shear deformation of carbon-fiber reinforced composites. Compos Sci Technol 2010;70:970–80. doi:10.1016/J.COMPSCITECH.2010.02.014.
[27] Cheng Z, Zhang L, Jiang C, Dai Y, Meng C, Luo L, et al. Aramid fiber with excellent interfacial properties suitable for resin composite in a wide polarity range. Chem Eng J 2018;347:483–92. doi:10.1016/J.CEJ.2018.04.149.
[28] Cherif C, editor. Textile Materials for Lightweight Constructions. Berlin, Heidelberg: Springer Berlin Heidelberg; 2016. doi:10.1007/978-3-662-46341-3.
[29] Lukaszewicz DH-JA, Ward C, Potter KD. The engineering aspects of automated prepreg layup: History, present and future. Compos Part B Eng 2012;43:997–1009. doi:10.1016/J.COMPOSITESB.2011.12.003.
[30] Mazumdar S. Composites Manufacturing. CRC Press; 2001. doi:10.1201/9781420041989.
[31] Strong AB. Fundamentals of composites manufacturing : materials, methods and applications. Society of Manufacturing Engineers; 2008.
[32] Gurunathan T, Mohanty S, Nayak SK. A review of the recent developments in biocomposites based on natural fibres and their application perspectives. Compos Part A Appl Sci Manuf 2015;77:1–25. doi:10.1016/J.COMPOSITESA.2015.06.007.
[33] Jani SP, Kumar AS, Khan MA, Kumar MU. Machinablity of Hybrid Natural Fiber Composite with and without Filler as Reinforcement. Mater Manuf Process 2016;31:1393–9. doi:10.1080/10426914.2015.1117633.
[34] Bajpai PK, Singh I. Drilling behavior of sisal fiber-reinforced polypropylene composite laminates. J Reinf Plast Compos 2013;32:1569–76. doi:10.1177/0731684413492866.
[35] Shah DU. Natural fibre composites: Comprehensive Ashby-type materials selection charts. Mater Des 2014;62:21–31. doi:10.1016/J.MATDES.2014.05.002.
[36] Baghaei B, Skrifvars M, Berglin L. Manufacture and characterisation of thermoplastic composites made from PLA/hemp co-wrapped hybrid yarn prepregs. Compos Part A Appl Sci Manuf 2013;50:93–101. doi:10.1016/j.compositesa.2013.03.012.
[37] Taj S, Khan S. Natural fiber-reinforced polymer composites. Proceddings Pakistan Acad Sci 2007;38:129–44.
[38] Bilisik K. Three-dimensional braiding for composites: A review. Text Res J 2013;83:1414–36. doi:10.1177/0040517512450766.
[39] Jones RM. Mechanics of Composite Materials. CRC Press; 2018. doi:10.1201/9781498711067.

[40] Xiaogang Chen X, Taylor LW, Tsai L-J. An overview on fabrication of three-dimensional woven textile preforms for composites. Text Res J 2011;81:932–44. doi:10.1177/0040517510392471.
[41] Guénon VA, Chou TW, Gillespie JW. Toughness properties of a three-dimensional carbon-epoxy composite. J Mater Sci 1989;24:4168–75. doi:10.1007/BF01168991.
[42] Cox BN, Dadkhah MS, Morris WL, Flintoff JG. Failure mechanisms of 3D woven composites in tension, compression, and bending. Acta Metall Mater 1994;42:3967–84. doi:10.1016/0956-7151(94)90174-0.
[43] Poe CC, Dexter HB, Raju IS. Review of the NASA Textile Composites Research. J Aircr 1999;36:876–84. doi:10.2514/2.2521.
[44] Boris D, Xavier L, Damien S. The tensile behaviour of biaxial and triaxial braided fabrics. J Ind Text 2018;47:2184–204. doi:10.1177/1528083716654469.
[45] Kamiya R, Cheeseman BA, Popper P, Chou T-W. Some recent advances in the fabrication and design of three-dimensional textile preforms: a review. Compos Sci Technol 2000;60:33–47. doi:10.1016/S0266-3538(99)00093-7.
[46] Kyosev Y, Gleßner P. Extended horn gears in 3D maypole braiding. J Text Fibrous Mater 2018;1:251522111878674. doi:10.1177/2515221118786741.
[47] Kyosev Y. Braiding technology for textiles. Elsevier/ Woodhead Pub; 2015.
[48] Lengersdorf M, Gries T. Three-dimensional (3D)-maypole braiding. Adv Braid Technol 2016:89–105. doi:10.1016/B978-0-08-100407-4.00003-X.
[49] Birkefeld K, Röder M, Von Reden T, Bulat M, Drechsler K. Characterization of biaxial and triaxial braids: Fiber architecture and mechanical properties. Appl Compos Mater 2012;19:259–73. doi:10.1007/s10443-011-9190-2.
[50] Mouritz AP, Bannister MK, Falzon PJ, Leong KH. Review of applications for advanced three-dimensional fibre textile composites. Compos Part A Appl Sci Manuf 1999;30:1445–61. doi:10.1016/S1359-835X(99)00034-2.
[51] Potluri P, Rawal A, Rivaldi M, Porat I. Geometrical modelling and control of a triaxial braiding machine for producing 3D preforms. Compos Part A Appl Sci Manuf 2003;34:481–92. doi:10.1016/S1359-835X(03)00061-7.
[52] Potluri P, Manan A, Francke M, Day RJ. Flexural and torsional behaviour of biaxial and triaxial braided composite structures. Compos Struct 2006;75:377–86. doi:10.1016/j.compstruct.2006.04.046.
[53] Ayranci C, Carey J. 2D braided composites: A review for stiffness critical applications. Compos Struct 2008;85:43–58. doi:10.1016/j.compstruct.2007.10.004.
[54] Ayranci C, Carey JP. Predicting the longitudinal elastic modulus of braided tubular composites using a curved unit-cell geometry. Compos Part B Eng 2010;41:229–35. doi:10.1016/j.compositesb.2009.10.006.
[55] Branscomb D, Beale D, Broughton R. New Directions in Braiding. J Eng Fibres Fabr 2013;8:11–24.
[56] Potluri P, Manan A. Mechanics of non-orthogonally interlaced textile composites. Compos Part A Appl Sci Manuf 2007;38:1216–26. doi:10.1016/j.compositesa.2006.04.008.
[57] Ruiz E, Trochu F. Flow modeling in composite reinforcements. Compos Reinf Optim Perform 2011:588–615. doi:10.1533/9780857093714.4.588.
[58] Zhang Q, Beale D, Adanur S, Broughton RM, Walker RP. Structural analysis of a two-dimensional braided fabric. J Text Inst 1997;88:41–52. doi:10.1080/00405009708658528.
[59] Kessels JFA, Akkerman R. Prediction of the yarn trajectories on complex braided preforms. Compos Part A Appl Sci Manuf 2002;33:1073–81. doi:10.1016/S1359-835X(02)00075-1.

[60] Van Ravenhorst JH, Akkerman R. Circular braiding take-up speed generation using inverse kinematics. Compos Part A Appl Sci Manuf 2014;64:147–58. doi:10.1016/j.compositesa.2014.04.020.

[61] Chen L, Tao XM, Choy CL. Mechanical analysis of 3-D braided composites by the finite multiphase element method. Compos Sci Technol 1999;59:2383–91. doi:10.1016/S0266-3538(99)00087-1.

[62] Lyons J, Pastore CM. Effect of braid structure on yarn cross-sectional shape. Fibers Polym 2004;5:182–6. doi:10.1007/BF02902997.

[63] Li D Sen, Li JL, Chen L, Lu ZX, Fang DN. Finite element analysis of mechanical properties of 3D four-directional rectangular braided composites part 1: Microgeometry and 3D finite element model. Appl Compos Mater 2010;17:373–87. doi:10.1007/s10443-010-9126-2.

[64] Kyosev Y, Cordes A. Geometrical modelling of tubular and flat braids within the jamming limits-verification and limitations. Recent Dev. Braid. Narrow Weav., Cham: Springer International Publishing; 2016, p. 23–31. doi:10.1007/978-3-319-29932-7_3.

[65] Kyosev Y. 21 – Geometrical modeling and computational mechanics tools for braided structures. Adv Braid Technol 2016:501–19. doi:10.1016/B978-0-08-100407-4.00021-1.

[66] Kyosev Y. Generalized geometric modeling of tubular and flat braided structures with arbitrary floating length and multiple filaments. Text Res J 2016;86:1270–9. doi:10.1177/0040517515609261.

[67] Tong L, Mouritz AP, Bannister MK. 3D fibre reinforced polymer composites. Elsevier; 2002.

[68] Byun JH, Chou TW. Modelling and characterization of textile structural composites: A review. J Strain Anal Eng Des 1989;24:253–62. doi:10.1243/03093247V244253.

[69] Roberts GD, Goldberg RK, Biniendak WK, Arnold WA, Littell JD, Kohlman LW. Characterization of triaxial braided composite material properties for impact simulation 2009.

[70] Littell JD, Binienda WK, Arnold WA, Roberts GD, Goldberg RK. Effect of microscopic damage events on static and ballistic impact strength of triaxial braid composites. Compos Part A Appl Sci Manuf 2009;40:1846–62. doi:10.1016/j.compositesa.2009.08.001.

[71] Han H, Taheri F, Pegg N. Crushing behaviors and energy absorption efficiency of hybrid pultruded and ??45?? braided tubes. Mech Adv Mater Struct 2011;18:287–300. doi:10.1080/15376494.2010.506103.

[72] Gan X, Yan J, gu B, Sun B. Impact tensile behavior and frequency response of 3D braided composites. Text Res J 2012;82:280–7. doi:10.1177/0040517511427970.

[73] Pan Z, Gu B, Sun B. Experimental investigation of high-strain rate properties of 3-D braided composite material in cryogenic field. Compos Part B Eng 2015;77:379–90. doi:10.1016/j.compositesb.2015.03.002.

[74] Laberge-Lebel L, Hoa S Van. Manufacturing of braided thermoplastic composites with carbon/nylon commingled fibers. J Compos Mater 2007;41:1101–21. doi:10.1177/0021998306067273.

[75] Ivanov DS, Baudry F, Van Den Broucke B, Lomov S V., Xie H, Verpoest I. Failure analysis of triaxial braided composite. Spec Issue 12th Eur Conf Compos Mater ECCM 2006 2008;69:1372–80. doi:10.1016/j.compscitech.2008.09.013.

[76] Liu Z, Liu L, Yu J. Unit yarn-reduction technique and flexural properties of tapered composites based on four-step row and column braiding. Compos Part A Appl Sci Manuf 2011;42:1883–91. doi:10.1016/j.compositesa.2011.08.010.

[77] Li S, Liu L, Yan J, Yu J. An approach for testing and predicting longitudinal tensile

modulus of 3D braided composites. J Reinf Plast Compos 2014;33:775–84. doi:10.1177/0731684414522332.

[78] Falzon PJ, Herszberg I. Mechanical performance of 2-D braided carbon/epoxy composites. Compos Sci Technol 1998;58:253–65. doi:10.1016/S0266-3538(97)00133-4.

[79] Kuo WS, Ko TH, Chen HI. Elastic moduli and damage mechanisms in 3D braided composites incorporating pultruded rods. Compos Part A Appl Sci Manuf 1998;29:681–92. doi:10.1016/S1359-835X(97)00110-3.

[80] Tang ZX, Postle R. Mechanics of three-dimensional braided structures for composite materials - part I: Fabric structure and fibre volume fraction. Compos Struct 2000;49:451–9. doi:10.1016/S0263-8223(00)00082-9.

[81] Castejón L, Miravete A, Cuartero J. Analytical formulation of (0°, ±α°) braided composites and its application in crashworthiness simulations. Mech Compos Mater Struct 2001;8:219–29. doi:10.1080/107594101750370497.

[82] Aggarwal A, Ramakrishna S, Ganesh VK. Predicting the strength of diamond braided composites. J Compos Mater 2002;36:625–43. doi:10.1177/0021998302036005487.

[83] Quek SC, Waas AM, Shahwan KW, Agaram V. Analysis of 2D triaxial flat braided textile composites. Int J Mech Sci 2003;45:1077–96. doi:10.1016/j.ijmecsci.2003.09.003.

[84] Goyal D. Analysis of Stress Concentrations in 2 2 Braided Composites. J Compos Mater 2005;40:533–46. doi:10.1177/0021998305055268.

[85] Pickett AK, Fouinneteau MRC. Material characterisation and calibration of a meso-mechanical damage model for braid reinforced composites. Compos Part A Appl Sci Manuf 2006;37:368–77. doi:10.1016/j.compositesa.2005.03.034.

[86] Fouinneteau MRC, Pickett AK. Shear mechanism modelling of heavy tow braided composites using a meso-mechanical damage model. Compos Part A Appl Sci Manuf 2007;38:2294–306. doi:10.1016/j.compositesa.2006.12.006.

[87] Pickett AK, Sirtautas J, Erber A. Braiding simulation and prediction of mechanical properties. Appl Compos Mater 2009;16:345–64. doi:10.1007/s10443-009-9102-x.

[88] Schmidt F, Rheinfurth M, Horst P, Busse G. Effects of local fibre waviness on damage mechanisms and fatigue behaviour of biaxially loaded tube specimens. Compos Sci Technol 2012;72:1075–82. doi:10.1016/j.compscitech.2011.09.012.

[89] Fang G, Liang J. A review of numerical modeling of three-dimensional braided textile composites. J Compos Mater 2011;45:2415–36. doi:10.1177/0021998311401093.

[90] Li D Sen, Fang DN, Jiang N, Xuefeng Y. Finite element modeling of mechanical properties of 3D five-directional rectangular braided composites. Compos Part B Eng 2011;42:1373–85. doi:10.1016/j.compositesb.2011.05.042.

[91] Qu P, Guan X, Jia Y, Lou S, Nie J. Effective elastic properties and stress distribution of 2D biaxial nonorthogonally braided composites. J Compos Mater 2012;46:997–1008. doi:10.1177/0021998311413684.

[92] Hwan CL, Tsai KH, Chen WL, Sun SJ. Predicting the elastic moduli of three-dimensional (four-step) braided tubes using a spatial spring model. J Compos Mater 2013;47:991–1000. doi:10.1177/0021998312444148.

[93] Schultz JA, Garnich MR. Meso-scale and multicontinuum modeling of a triaxial braided textile composite. J Compos Mater 2013;47:303–14. doi:10.1177/0021998312440128.

[94] Ji X, Khatri AM, Chia ES, Cha RK, Yeo BT, Joshi SC, et al. Multi-scale simulation and finite-element-assisted computation of elastic properties of braided textile reinforced composites. J Compos Mater 2014;48:931–49. doi:10.1177/0021998313480198.

[95] Kier ZT, Salvi A, Theis G, Waas AM, Shahwan K. Estimating mechanical properties of 2D triaxially braided textile composites based on microstructure properties. Compos Part B Eng 2015;68:288–99. doi:10.1016/j.compositesb.2014.08.039.

[96] Catera PG, Gagliardi F, Mundo D, De Napoli L, Matveeva A, Farkas L. Multi-scale modeling of triaxial braided composites for FE-based modal analysis of hybrid metal-composite gears. Compos Struct 2017;182:116–23. doi:10.1016/j.compstruct.2017.09.017.

[97] Wehrkamp-Richter T, De Carvalho N V., Pinho ST. Predicting the non-linear mechanical response of triaxial braided composites. Compos Part A Appl Sci Manuf 2018;114:117–35. doi:10.1016/J.COMPOSITESA.2018.08.011.

[98] Swanek DSS, Carey J. Braided composite materials for the production of lightweight, high rigidity golf shafts. Sport Eng 2007;10:195–208. doi:10.1007/BF02933571.

[99] Rawal A, Kumar R, Saraswat H. Tensile mechanics of braided sutures. Text Res J 2012;82:1703–10. doi:10.1177/0040517512445340.

[100] Monnot P, Lévesque J, Laberge Lebel L. Automated braiding of a complex aircraft fuselage frame using a non-circular braiding model. Compos Part A Appl Sci Manuf 2017;102:48–63. doi:10.1016/j.compositesa.2017.07.011.

[101] McKenna HA, Hearle JWS, O'Hear N. Handbook of fibre rope technology. Woodhead; 2004. doi:10.1533/9781855739932.

[102] Davies P, Reaud Y, Dussud L, Woerther P. Mechanical behaviour of HMPE and aramid fibre ropes for deep sea handling operations. Ocean Eng 2011;38:2208–14. doi:10.1016/j.oceaneng.2011.10.010.

[103] Shalin RE. Polymer Matrix Composites. Springer Netherlands; 1995.

[104] Rudd CD, Long AC, Kendall KN, Mangin CGE. Liquid moulding technologies : resin transfer moulding, structural reaction injection moulding, and related processing techniques. SAE International; 1997. doi:10.1649/1065.1.

[105] Campbell FC (Flake C. Manufacturing processes for advanced composites. Elsevier; 2004.

[106] Kruckenberg T, Paton R. Resin transfer molding for aerospace structures. Springer; 1998.

[107] Williams C, Summerscales J, Grove S. Resin Infusion under Flexible Tooling (RIFT): a review. Compos Part A Appl Sci Manuf 1996;27:517–24. doi:10.1016/1359-835X(96)00008-5.

[108] Zin MH, Razzi MF, Othman S, Liew K, Abdan K, Mazlan N. A review on the fabrication method of bio-sourced hybrid composites for aerospace and automotive applications. IOP Conf Ser Mater Sci Eng 2016;152:12041. doi:10.1088/1757-899X/152/1/012041.

[109] ZHANG Q, GAO Q, CAI J. Experimental and simulation research on thermal stamping of carbon fiber composite sheet. Trans Nonferrous Met Soc China 2014;24:217–23. doi:10.1016/S1003-6326(14)63050-8.

[110] Syerko E, Comas-Cardona S, Binetruy C. Models for shear properties/behavior of dry fibrous materials at various scales: a review. Int J Mater Form 2015;8:1–23. doi:10.1007/s12289-013-1138-7.

[111] Endruweit A, Long AC. A model for the in-plane permeability of triaxially braided reinforcements. Compos Part A Appl Sci Manuf 2011;42:165–72. doi:10.1016/j.compositesa.2010.11.003.

[112] Lindberg J, Behre B, Dahlberg B. Part III: Shearing and Buckling of Various Commercial Fabrics. Text Res J 1961;31:99–122. doi:10.1177/004051756103100203.

[113] Skordos AA, Monroy Aceves C, Sutcliffe MPF. A simplified rate dependent model of forming and wrinkling of pre-impregnated woven composites. Compos Part A Appl

Sci Manuf 2007;38:1318–30. doi:10.1016/j.compositesa.2006.11.005.

[114] Cao J, Akkerman R, Boisse P, Chen J, Cheng HS, de Graaf EF, et al. Characterization of mechanical behavior of woven fabrics: Experimental methods and benchmark results. Compos Part A Appl Sci Manuf 2008;39:1037–53. doi:10.1016/j.compositesa.2008.02.016.

[115] Spivak SM, Treloar LRG. The Behavior of Fabrics in Shear. Text Res J 1968;38:963–71. doi:10.1177/004051756803800911.

[116] Kawabata S, Niwa M, Kawai H. 3—THE FINITE-DEFORMATION THEORY OF PLAIN-WEAVE FABRICS PART I: THE BIAXIAL-DEFORMATION THEORY. J Text Inst 1973;64:21–46. doi:10.1080/00405007308630416.

[117] Grosberg P, Park BJ. The Mechanical Properties of Woven Fabrics. Text Res J 1966;36:420–31. doi:10.1177/004051756603600505.

[118] Wang J, Page JR, Paton R. Experimental investigation of the draping properties of reinforcement fabrics. Compos Sci Technol 1998;58:229–37. doi:10.1016/S0266-3538(97)00115-2.

[119] Lomov SV, Boisse P, Deluycker E, Morestin F, Vanclooster K, Vandepitte D, et al. Full-field strain measurements in textile deformability studies. Compos Part A Appl Sci Manuf 2008;39:1232–44. doi:10.1016/J.COMPOSITESA.2007.09.014.

[120] Rozant O, Bourban P-E, Månson J-A. Drapability of dry textile fabrics for stampable thermoplastic preforms. Compos Part A Appl Sci Manuf 2000;31:1167–77. doi:10.1016/S1359-835X(00)00100-7.

[121] Potluri P, Perez Ciurezu DA, Ramgulam RB. Measurement of meso-scale shear deformations for modelling textile composites. Compos Part A Appl Sci Manuf 2006;37:303–14. doi:10.1016/J.COMPOSITESA.2005.03.032.

[122] Hivet G, Duong A V. A contribution to the analysis of the intrinsic shear behavior of fabrics. J Compos Mater 2011;45:695–716. doi:10.1177/0021998310382315.

[123] Mohammed U, Lekakou C, Dong L, Bader MG. Shear deformation and micromechanics of woven fabrics. Compos Part A Appl Sci Manuf 2000;31:299–308. doi:10.1016/S1359-835X(99)00081-0.

[124] Nguyen M, Herszberg I, Paton R. The shear properties of woven carbon fabric. Compos Struct 1999;47:767–79. doi:10.1016/S0263-8223(00)00051-9.

[125] Boisse P, Hamila N, Guzman-Maldonado E, Madeo A, Hivet G, dell'Isola F. The bias-extension test for the analysis of in-plane shear properties of textile composite reinforcements and prepregs: a review. Int J Mater Form 2017;10:473–92. doi:10.1007/s12289-016-1294-7.

[126] Peng XQ, Cao J, Chen J, Xue P, Lussier DS, Liu L. Experimental and numerical analysis on normalization of picture frame tests for composite materials. Compos Sci Technol 2004;64:11–21. doi:10.1016/S0266-3538(03)00202-1.

[127] Pazmino J, Carvelli V, Lomov S V., Van Mieghem B, Lava P. 3D digital image correlation measurements during shaping of a non-crimp 3D orthogonal woven E-glass reinforcement. Int J Mater Form 2014;7:439–46. doi:10.1007/s12289-013-1139-6.

[128] Zouari B, Daniel J-L, Boisse P. A woven reinforcement forming simulation method. Influence of the shear stiffness. Comput Struct 2006;84:351–63. doi:10.1016/J.COMPSTRUC.2005.09.031.

[129] Harrison P, Clifford MJ, Long AC. Shear characterisation of viscous woven textile composites: A comparison between picture frame and bias extension experiments. Compos Sci Technol 2004;64:1453–65. doi:10.1016/j.compscitech.2003.10.015.

[130] Härtel F, Harrison P. Evaluation of normalisation methods for uniaxial bias extension tests on engineering fabrics. Compos Part A Appl Sci Manuf 2014;67:61–9. doi:10.1016/J.COMPOSITESA.2014.08.011.

[131] Harrison P, Wiggers J, Long AC. Normalization of Shear Test Data for Rate-independent Compressible Fabrics. J Compos Mater 2008;42:2315–44. doi:10.1177/0021998308095367.
[132] Hamila N, Boisse P, Sabourin F, Brunet M. A semi-discrete shell finite element for textile composite reinforcement forming simulation. Int J Numer Methods Eng 2009;79:1443–66. doi:10.1002/nme.2625.
[133] Hamila N, Boisse P. Simulations of textile composite reinforcement draping using a new semi-discrete three node finite element. Compos Part B Eng 2008;39:999–1010. doi:10.1016/j.compositesb.2007.11.008.
[134] Guzman-Maldonado E, Hamila N, Naouar N, Moulin G, Boisse P. Simulation of thermoplastic prepreg thermoforming based on a visco-hyperelastic model and a thermal homogenization. Mater Des 2016;93:431–42. doi:10.1016/j.matdes.2015.12.166.
[135] Lebrun G, Bureau MN, Denault J. Evaluation of bias-extension and picture-frame test methods for the measurement of intraply shear properties of PP/glass commingled fabrics. Compos Struct 2003;61:341–52. doi:10.1016/S0263-8223(03)00057-6.
[136] Wang P, Hamila N, Boisse P. Thermoforming simulation of multilayer composites with continuous fibres and thermoplastic matrix. Compos Part B Eng 2013;52:127–36. doi:10.1016/J.COMPOSITESB.2013.03.045.
[137] Haanappel SP, ten Thije RHW, Sachs U, Rietman B, Akkerman R. Formability analyses of uni-directional and textile reinforced thermoplastics. Compos Part A Appl Sci Manuf 2014;56:80–92. doi:10.1016/J.COMPOSITESA.2013.09.009.
[138] Guzman-Maldonado E, Hamila N, Boisse P, Bikard J. Thermomechanical analysis, modelling and simulation of the forming of pre-impregnated thermoplastics composites. Compos Part A Appl Sci Manuf 2015;78:211–22. doi:10.1016/j.compositesa.2015.08.017.
[139] Harte A-M, Fleck NA. On the mechanics of braided composites in tension. Eur J Mech - A/Solids 2000;19:259–75. doi:10.1016/S0997-7538(99)00164-3.
[140] Hristov K, Armstrong-Carroll E, Dunn M, Pastore C, Gowayed Y. Mechanical Behavior of Circular Hybrid Braids Under Tensile Loads. Text Res J 2004;74:20–6. doi:10.1177/004051750407400104.
[141] Dabiryan H, Johari MS. Analysis of the tensile behavior of tubular braids using energy method, part I: theoretical analysis. J Text Inst 2016;107:553–61. doi:10.1080/00405000.2015.1046309.
[142] Subramani P, Rana S, Oliveira D V., Fangueiro R, Xavier J. Development of novel auxetic structures based on braided composites. Mater Des 2014;61:286–95. doi:10.1016/j.matdes.2014.04.067.
[143] Rebelo R, Vila N, Fangueiro R, Carvalho S, Rana S. Influence of design parameters on the mechanical behavior and porosity of braided fibrous stents. Mater Des 2015;86:237–47. doi:10.1016/j.matdes.2015.07.051.
[144] Del Rosso S, Iannucci L, Curtis PT. Experimental investigation of the mechanical properties of dry microbraids and microbraid reinforced polymer composites. Compos Struct 2015;125:509–19. doi:10.1016/j.compstruct.2015.02.036.
[145] Rawal A, Potluri P, Steele C. Geometrical modeling of the yarn paths in three-dimensional braided structures. J Ind Text 2005;35:115–35. doi:10.1177/1528083705057574.
[146] Rawal A, Saraswat H, Kumar R. Tensile response of tubular braids with an elastic core. Compos Part A Appl Sci Manuf 2013;47:150–5. doi:10.1016/j.compositesa.2012.12.006.
[147] Rawal A, Saraswat H, Sibal A. Tensile response of braided structures: A review. Text

Res J 2015;85:2083–96. doi:10.1177/0040517515576331.

[148] Labanieh AR, Garnier C, Ouagne P, Dalverny O, Soulat D. Intra-ply yarn sliding defect in hemisphere preforming of a woven preform. Compos Part A Appl Sci Manuf 2018;107:432–46. doi:10.1016/j.compositesa.2018.01.018.

[149] Bloom LD, Wang J, Potter KD. Damage progression and defect sensitivity: An experimental study of representative wrinkles in tension. Compos Part B Eng 2013;45:449–58. doi:10.1016/j.compositesb.2012.05.021.

[150] Ouagne P, Soulat D, Hivet G, Allaoui S, Duriatti D. Analysis of defects during the preforming of a woven flax reinforcement. Adv Compos Lett 2011;20:105–8.

[151] Sharma SB, Sutcliffe MPF, Chang SH. Characterisation of material properties for draping of dry woven composite material. Compos Part A Appl Sci Manuf 2003;34:1167–75. doi:10.1016/j.compositesa.2003.09.001.

[152] Ouagne P, Soulat D, Moothoo J, Capelle E, Gueret S. Complex shape forming of a flax woven fabric; Analysis of the tow buckling and misalignment defect. Compos Part A Appl Sci Manuf 2013;51:1–10. doi:10.1016/j.compositesa.2013.03.017.

[153] Arbter R, Beraud JM, Binetruy C, Bizet L, Bréard J, Comas-Cardona S, et al. Experimental determination of the permeability of textiles: A benchmark exercise. Compos Part A Appl Sci Manuf 2011;42:1157–68. doi:10.1016/j.compositesa.2011.04.021.

[154] Ouagne P, Bréard J. Continuous transverse permeability of fibrous media. Compos Part A Appl Sci Manuf 2010;41:22–8. doi:10.1016/j.compositesa.2009.07.008.

[155] Sjölander J, Hallander P, Åkermo M. Forming induced wrinkling of composite laminates: A numerical study on wrinkling mechanisms. Compos Part A Appl Sci Manuf 2016;81:41–51. doi:10.1016/j.compositesa.2015.10.012.

[156] Wang P, Legrand X, Soulat D. Investigation about the manufacturing technique of the composite corner fitting part. Autex Res J 2014;14:111–20. doi:10.2478/aut-2014-0007.

[157] Gereke T, Döbrich O, Hübner M, Cherif C. Experimental and computational composite textile reinforcement forming: A review. Compos Part A Appl Sci Manuf 2013;46:1–10. doi:10.1016/j.compositesa.2012.10.004.

[158] Khan MA, Mabrouki T, Vidal-Sallé E, Boisse P. Numerical and experimental analyses of woven composite reinforcement forming using a hypoelastic behaviour. Application to the double dome benchmark. J Mater Process Technol 2010;210:378–88. doi:10.1016/j.jmatprotec.2009.09.027.

[159] Ouagne P, Soulat D, Tephany C, Gillibert J. Measurement of the Appearance and Growth of Tow Buckling Defect in the Frame of Complex Shape Manufacturing Process by Using Fringe Projection Technique. Strain 2016;52:559–69. doi:10.1111/str.12206.

[160] Capelle E, Ouagne P, Soulat D, Duriatti D. Complex shape forming of flax woven fabrics: Design of specific blank-holder shapes to prevent defects. Compos Part B Eng 2014;62:29–36. doi:10.1016/j.compositesb.2014.02.007.

[161] Allaoui S, Cellard C, Hivet G. Effect of inter-ply sliding on the quality of multilayer interlock dry fabric preforms. Compos Part A Appl Sci Manuf 2015;68:336–45. doi:10.1016/j.compositesa.2014.10.017.

[162] Nosrat Nezami F, Gereke T, Cherif C. Active forming manipulation of composite reinforcements for the suppression of forming defects. Compos Part A Appl Sci Manuf 2017;99:94–101. doi:10.1016/j.compositesa.2017.04.011.

[163] Gatouillat S, Bareggi A, Vidal-Sallé E, Boisse P. Meso modelling for composite preform shaping - Simulation of the loss of cohesion of the woven fibre network. Compos Part A Appl Sci Manuf 2013;54:135–44. doi:10.1016/j.compositesa.2013.07.010.

[164] Hallander P, Akermo M, Mattei C, Petersson M, Nyman T. An experimental study of mechanisms behind wrinkle development during forming of composite laminates. Compos Part A Appl Sci Manuf 2013;50:54–64. doi:10.1016/j.compositesa.2013.03.013.

[165] Li XK, Bai SL. Sheet forming of the multi-layered biaxial weft knitted fabric reinforcement. Part I: On hemispherical surfaces. Compos Part A Appl Sci Manuf 2009;40:766–77. doi:10.1016/j.compositesa.2009.03.007.

[166] Jauffrès D, Sherwood JA, Morris CD, Chen J. Discrete mesoscopic modeling for the simulation of woven-fabric reinforcement forming. Int J Mater Form 2010;3:1205–16. doi:10.1007/s12289-009-0646-y.

[167] Peng X, Ding F. Validation of a non-orthogonal constitutive model for woven composite fabrics via hemispherical stamping simulation. Compos Part A Appl Sci Manuf 2011;42:400–7. doi:10.1016/j.compositesa.2010.12.014.

[168] Peng X, Rehman ZU. Textile composite double dome stamping simulation using a non-orthogonal constitutive model. Compos Sci Technol 2011;71:1075–81. doi:10.1016/j.compscitech.2011.03.010.

[169] Peng X, Guo Z, Du T, Yu WR. A simple anisotropic hyperelastic constitutive model for textile fabrics with application to forming simulation. Compos Part B Eng 2013;52:275–81. doi:10.1016/j.compositesb.2013.04.014.

[170] Zhu B, Yu T, Zhang H, Engineering XT-CPB, 2011 U. Experimental investigation of formability of commingled woven composite preform in stamping operation. Compos Part B Eng 2011;42:289–95.

[171] Boisse P, Hamila N, Vidal-Sallé E, Dumont F. Simulation of wrinkling during textile composite reinforcement forming. Influence of tensile, in-plane shear and bending stiffnesses. Compos Sci Technol 2011;71:683–92. doi:10.1016/j.compscitech.2011.01.011.

[172] Allaoui S, Boisse P, Chatel S, Hamila N, Hivet G, Soulat D, et al. Experimental and numerical analyses of textile reinforcement forming of a tetrahedral shape. Compos Part A Appl Sci Manuf 2011;42:612–22. doi:10.1016/j.compositesa.2011.02.001.

[173] Allaoui S, Hivet G, Soulat D, Wendling A, Ouagne P, Chatel S. Experimental preforming of highly double curved shapes with a case corner using an interlock reinforcement. Int J Mater Form 2014;7:155–65. doi:10.1007/s12289-012-1116-5.

[174] Wang P, Legrand X, Boisse P, Hamila N, Soulat D. Experimental and numerical analyses of manufacturing process of a composite square box part: Comparison between textile reinforcement forming and surface 3D weaving. Compos Part B Eng 2015;78:26–34. doi:10.1016/j.compositesb.2015.03.072.

[175] Jacquot PB, Wang P, Soulat D, Legrand X. Analysis of the preforming behaviour of the braided and woven flax/polyamide fabrics. J Ind Text 2016;46:698–718. doi:10.1177/1528083715591592.

[176] Gao Y, Li J. Effects of braiding angle on modal experimental analysis of three-dimensional and five-directional braided composites. Compos Part B Eng 2012;43:2423–8. doi:10.1016/J.COMPOSITESB.2011.11.025.

[177] Okano M, Sugimoto K, Saito H, Nakai A, Hamada H. Effect of the braiding angle on the energy absorption properties of a hybrid braided FRP tube. Proc Inst Mech Eng Part L J Mater Des Appl 2005;219:59–66. doi:10.1243/146442005X10256.

[178] Tate JS, Kelkar AD, Whitcomb JD. Effect of braid angle on fatigue performance of biaxial braided composites. Int J Fatigue 2006;28:1239–47. doi:10.1016/J.IJFATIGUE.2006.02.009.

[179] Hashish M. A Modeling Study of Metal Cutting with Abrasive Water Jets. Trans ASME J Eng Mater Technol 1984;106:88–100.

[180] Finnie I. The Mechanism of Erosion of Ductile Metals. Proc. third U.S. Natl. Congr. Appl. Mech. held Brown Univ. Provid. Rhode Island, June 11-14, 1958, 1958, p. 527–32.
[181] Bitter JGA. A study of erosional phenomena, Part II. Wear 1963;6:169–90. doi:10.1016/0043-1648(63)90003-6.
[182] Bitter JGA. A study of erosion phenomena. Part II. Wear 1963;6:169–90. doi:10.1016/0043-1648(63)90073-5.
[183] Arola D, Ramulu M. A study of Kerf characteristics in abrasive waterjet machining of graphite/ epoxy composite. J Eng Mater Technol-Trans ASME 1996;118:256–65. doi:10.1115/1.2804897.
[184] Wang J. Machinability study of polymer matrix composites using abrasive waterjet cutting technology. J Mater Process Technol 1999;94:30–5. doi:10.1016/S0924-0136(98)00443-9.
[185] Hashish M. Characteristics of Surfaces Machined With Abrasive-Waterjets. J Eng Mater Technol 1991;113:354–62. doi:10.1115/1.2903418.
[186] Liu H, Wang J, Kelson N, Brown RJ. A study of abrasive waterjet characteristics by CFD simulation. J Mater Process Technol 2004;153–154:488–93. doi:10.1016/j.jmatprotec.2004.04.037.
[187] Wang J. Abrasive Waterjet Machining of Engineering Materials. 2003.
[188] Doreswamy D, Shivamurthy B, Anjaiah D, Sharma NY. An Investigation of Abrasive Water Jet Machining on Graphite/Glass/Epoxy Composite. Int J Manuf Eng 2015;2015:1–11. doi:10.1155/2015/627218.
[189] Wang J. Abrasive waterjet machining of polymer matrix composites - cutting performance, erosive process and predictive models. Int J Adv Manuf Technol 1999;15:757–68. doi:10.1007/s001700050129.
[190] Azmir MA, Ahsan AK. Investigation on glass/epoxy composite surfaces machined by abrasive water jet machining. J Mater Process Technol 2008;198:122–8. doi:10.1016/j.jmatprotec.2007.07.014.
[191] Ramulu M, Arola D. The influence of abrasive waterjet cutting conditions on the surface quality of graphite/epoxy laminates. Int J Mach Tools Manuf 1994;34:295–313. doi:10.1016/0890-6955(94)90001-9.
[192] Jackson MJ, Davim JP. Machining with abrasives. 2011. doi:10.1007/978-1-4419-7302-3.
[193] Shanmugam DK, Wang J, Liu H. Minimisation of kerf tapers in abrasive waterjet machining of alumina ceramics using a compensation technique. Int J Mach Tools Manuf 2008;48:1527–34. doi:10.1016/j.ijmachtools.2008.07.001.
[194] Lemma E, Chen L, Siores E, Wang J. Study of cutting fiber-reinforced composites by using abrasive water-jet with cutting head oscillation. Compos Struct 2002;57:297–303. doi:10.1016/S0263-8223(02)00097-1.
[195] Lemma E, Chen L, Siores E, Wang J. Optimising the AWJ cutting process of ductile materials using nozzle oscillation technique. Int J Mach Tools Manuf 2002;42:781–9. doi:10.1016/S0890-6955(02)00017-2.
[196] Chen FL, Siores E, Patel K. Improving the cut surface qualities using different controlled nozzle oscillation techniques. Int J Mach Tools Manuf 2002;42:717–22. doi:10.1016/S0890-6955(01)00161-4.
[197] Wang J, Kuriyagawa T, Huang CZ. An experimental study to enhance the cutting performance in abrasive waterjet machining. Mach Sci Technol 2003;7:191–207. doi:10.1081/MST-120022777.
[198] Wang J, Guo DM. The cutting performance in multipass abrasive waterjet machining of industrial ceramics. J Mater Process Technol 2003;133:371–7. doi:10.1016/S0924-

0136(02)01125-1.

[199] Cantwell WJ, Morton J. The impact resistance of composite materials - a review. Composites 1991;22:347–62. doi:10.1016/0010-4361(91)90549-V.

[200] Potter K. Bias extension measurements on cross-plied unidirectional prepreg. Compos - Part A Appl Sci Manuf 2002;33:63–73. doi:10.1016/S1359-835X(01)00057-4.

[201] hu JL, Zhang yi T. The KES Shear Test for Fabrics. Text Res J 1997;67:654–64. doi:10.1177/004051759706700904.

[202] Cao J, Akkerman R, Boisse P, Chen J, Cheng H., De Graaf E., et al. Characterization of mechanical behavior of woven fabrics-Experimental methods and benchamrk results. Compos Part A Appl Sci Manuf 2008;39:1037–53.

[203] Launay J, Hivet G, Duong A, And PB. Experimental analysis of the influence of tensions on in plane shear behaviour of woven composite reinforcements. Compos Sci Technol 2008;68:506–15. doi:10.1063/1.2729650.

[204] Härtel F, And PH-CPAAS, 2014 U. Evaluation of normalisation methods for uniaxial bias extension tests on engineering fabrics. Compos Part A Appl Sci Manuf 2014;67:61–9. doi:10.1016/j.compositesa.2014.08.011.

[205] Nosrat-Nezami F, Gereke T, Eberdt C, Cherif C. Characterisation of the shear-tension coupling of carbon-fibre fabric under controlled membrane tensions for precise simulative predictions of industrial preforming processes. Compos Part A Appl Sci Manuf 2014;67:131–9. doi:10.1016/j.compositesa.2014.08.030.

[206] Lomov S V., Verpoest I. Model of shear of woven fabric and parametric description of shear resistance of glass woven reinforcements. Compos Sci Technol 2006;66:919–33. doi:10.1016/j.compscitech.2005.08.010.

[207] Harrison P, Abdiwi F, Guo Z, Potluri P, Yu WR. Characterising the shear-tension coupling and wrinkling behaviour of woven engineering fabrics. Compos Part A Appl Sci Manuf 2012;43:903–14. doi:10.1016/j.compositesa.2012.01.024.

[208] Harrison P. Normalisation of biaxial bias extension test results considering shear tension coupling. Compos Part A Appl Sci Manuf 2012;43:1546–54. doi:10.1016/j.compositesa.2012.04.014.

[209] Duchamp B, Legrand X, Soulat D. The tensile behaviour of biaxial and triaxial braided fabrics. J Ind Text 2016:1–21. doi:10.1177/1528083716654469.

[210] Zhou Y, Chen X, Wells G. Influence of yarn gripping on the ballistic performance of woven fabrics from ultra-high molecular weight polyethylene fibre. Compos Part B Eng 2014;62:198–204. doi:10.1016/J.COMPOSITESB.2014.02.022.

[211] Duchamp B, Kyosev Y, Legrand X, Soulat D. Experimental and numerical investigation of triaxial braid reinforcements. Narrow Smart Text., Cham: Springer International Publishing; 2017, p. 123–40. doi:10.1007/978-3-319-69050-6_11.

[212] Mulvihill DM, Smerdova O, Sutcliffe MPF. Friction of carbon fibre tows. Compos Part A Appl Sci Manuf 2017;93:185–98. doi:10.1016/J.COMPOSITESA.2016.08.034.

[213] Wang J, Guo DM. A predictive depth of penetration model for abrasive waterjet cutting of polymer matrix composites. J Mater Process Technol 2002;121:390–4. doi:10.1016/S0924-0136(01)01246-8.

[214] Monno M, Ravasio C. The effect of cutting head vibrations on the surfaces generated by waterjet cutting. Int J Mach Tools Manuf 2005;45:355–63. doi:10.1016/j.ijmachtools.2004.07.010.

[215] Li W, Zhu H, Wang J, Huang C. Radial-mode abrasive waterjet turning of short carbon–fiber-reinforced plastics. Mach Sci Technol 2016;20:231–48. doi:10.1080/10910344.2016.1165836.

[216] Hascalik A, Çaydaş U, Gürün H. Effect of traverse speed on abrasive waterjet machining of Ti-6Al-4V alloy. Mater Des 2007;28:1953–7.

doi:10.1016/j.matdes.2006.04.020.

[217] Wang J. Predictive depth of jet penetration models for abrasive waterjet cutting of alumina ceramics. Int J Mech Sci 2007;49:306–16. doi:10.1016/j.ijmecsci.2006.09.005.

Abstract

The mechanical characteristics and deformability behaviours of reinforcements are essential knowledge to optimize manufacturing process composites with complex shapes. Meanwhile, the machining properties of composites also greatly determine the in-service performance of composite parts. This thesis is not only dedicated on the three aspects in manufacturing and machining processes to explore what characters the special features in the mechanical properties and deformability behaviours of braided fabrics, which are promising and excellent textile reinforcements for composites with complex shapes. But also to study machining processes using the abrasive water jet technique in order to further improve machining efficiency without sacrificing quality. The mechanical characteristics of braided fabrics, especially for in-plane shearing phenomenon, were originally investigated and modelled based on bias-extension test. In addition, triaxial braids were also the subject of an experimental study to determine the mechanical characteristics with regard to braiding parameters, such as braiding angle and number of yarns. The deformability behaviour of triaxial braids during the preforming step was analysed and correlated with the associated defects according to the different process conditions, such as the pressures applied. In addition, the evolution of the deformability behaviour as a function of the braiding angle was geometrically modelled and verified by experimental results. The upgraded multi-pass cutting of abrasive waterjet was firstly introduced into composites machining process based on the exploration of the corresponding material removal mechanism. It was experimentally concluded that such technique could effectively enhance the machining quality and efficiency.

Résumé

Les caractéristiques mécaniques et le comportement à la déformabilité des renforts sont des connaissances essentielles pour optimiser les procédés de fabrication des composites notamment de formes complexes. Par ailleurs, les propriétés d'usinage des composites déterminent également grandement la performance en service des pièces composites. Cette thèse est consacrée aux trois aspects des procédés de fabrication et d'usinage afin d'explorer les caractéristiques particulières des propriétés mécaniques et des comportements de déformabilité des tissus tressés, qui sont des renforts textiles prometteurs et excellents pour les composites aux formes complexes. Mais également étudier les procédés d'usinage en utilisant la technique du jet d'eau abrasif afin d'améliorer encore l'efficacité de l'usinage sans sacrifier la qualité. Les caractéristiques mécaniques des renforts tressés, en particulier pour les composantes de cisaillement dans le plan, ont d'abord été étudiées et modélisées à partir d'essais de bias-test. Par ailleurs, les tresses triaxiales ont également fait l'objet d'une étude expérimentale de détermination des caractéristiques mécaniques relativement aux paramètres de tressage, tels que l'angle de tressage et le nombre de fils. Le comportement à la déformabilité des tresses triaxiales lors de l'étape de préformage a été analysé et corrélés avec les défauts associés en fonction des différentes conditions du procédé, telles que les pressions appliquées. De plus, l'évolution du comportement à la déformabilité en fonction de l'angle de tressage a été modélisée géométriquement et vérifiée par des résultats expérimentaux. La découpe améliorée multi-passe du jet d'eau abrasif a été introduite dans le processus d'usinage des composites grâce à l'exploration du mécanisme d'enlèvement de matière associée. Il a été conclu expérimentalement qu'une telle technique pouvait améliorer efficacement la qualité et l'efficacité de l'usinage.